

Modeling and Simulation of the Forming of Aluminum Sheet Alloys

Jeong Whan Yoon and Frédéric Barlat, Alloy Technology and Materials Research Division, Alcoa Technical Center

WITH ADVANCES in computer hardware and software, it is possible to model material processing, product manufacturing, product performance in service, and failure. Although the fine-tuning of product manufacturing and performance is empirical, modeling can be an efficient tool to guide and optimize design, to evaluate material attributes, and to predict lifetime and failure. Moreover, modeling can be used as a research tool for a more fundamental understanding of physical phenomena that can result in the development of improved or new products.

This article is concerned with the numerical simulation of the forming of aluminum alloy sheet metals. In order to design a process for a specific material, it is necessary to account for the attributes of the material in the simulations. Although the numerical methods are generic and can be applied to any material, constitutive models, that is, the mathematical descriptions of material behavior, are material-specific. Therefore, macroscopic and microscopic aspects of the plastic behavior of aluminum alloys are reviewed first. The following are then discussed to cover theoretical and implementation aspects of sheet metal forming simulation:

- Constitutive equations suitable for the description of aluminum alloy sheets
- Testing procedures and analysis methods used to measure the relevant data needed to identify the material coefficients
- Tensile and compressive instabilities in sheet forming. For tensile instability, both strain- and stress-based forming-limit curves are discussed.
- Springback analysis
- Finite Element (FE) formulation
- Stress-integration procedures for both continuum and crystal-plasticity mechanics
- Finite element design

Finally, various examples of the simulation of aluminum sheet forming are presented. These examples include earing in cup drawing, wrinkling, automotive stamping, hemming, hydroforming, and clam-shell-resistant design via

FE analysis and the Taguchi (Ref 1) optimization method.

Material Modeling

Plasticity of Aluminum Alloys

Macroscopic Observations. Aspects of the plastic deformation and ductility of aluminum alloys at low and moderate strain rates and subjected to monotonic loading or to a few load cycles are briefly discussed here. The stress-strain behavior at low strain is almost always reversible and linear. The elastic range, however, is bounded by the yield limit, the stress above which permanent or inelastic deformations occur. In the plastic range, the flow stress, described by a stress-strain curve, increases with the amount of accumulated plastic strain and becomes the new yield stress if the material is unloaded.

In general, it is considered that plastic deformation occurs without any volume change and that hydrostatic pressure has no influence on yielding. Experiments conducted at high confinement pressure showed that, although very small, a pressure effect is quantifiable (Ref 2, 3). However, practically, this effect can be neglected for aluminum alloys at low confinement pressure. A feature common in aluminum alloys is the Bauschinger effect. This occurs when a material is deformed up to a given strain, unloaded, and loaded in the reverse direction—typically, tension followed by compression. The yield stress after strain reversal is lower than the flow stress before unloading from the first deformation step.

The flow stress of an alloy depends on the testing temperature. Moreover, at low absolute temperature compared to the melting point, time usually has a very small influence on the flow stress and plasticity in general. However, at higher temperatures, strain-rate effects are important. In fact, it has been observed that strain rate and temperature have virtually identical effects on plasticity. Raising the temperature

under which an experiment is carried out is similar to decreasing the strain rate. Temperature has another influence on plasticity. When subjected to a constant stress smaller than the yield limit, a material can deform by creep. A similar phenomenon, called relaxation, corresponds to a decrease in the applied stress when the strain is held constant.

Microscopic Aspects. Commercial aluminum alloys used in forming operations are polycrystalline. They are composed of numerous grains, each with a given lattice orientation with respect to macroscopic axes. At low temperature compared to the melting point, metals and alloys deform by dislocation glide or slip on given crystallographic planes and directions, which produces microscopic shear deformations (Ref 4). Therefore, the distribution of grain orientations—the crystallographic texture—plays an important role in plasticity. Because of the geometrical nature of slip deformation, strain incompatibilities arise between grains and produce micro-residual stresses, which macroscopically lead to a Bauschinger effect. Slip results in a gradual lattice rotation as deformation proceeds. After slip, dislocations accumulate at microstructural obstacles and increase the slip resistance for further deformation, leading to strain hardening with its characteristic stress-strain curve.

At higher temperature, more slip systems can be available to accommodate the deformation (Ref 5), but grain-boundary sliding becomes more predominant. For instance, superplastic forming occurs mainly by grain-boundary sliding (Ref 6). In this case, the grain size and shape are important parameters. Atomic diffusion is also another mechanism that affects plastic deformation at high temperature and contributes to creep as well as the accommodation of stress concentrations that arise due to grain-boundary sliding.

Commercial aluminum alloys contain second-phase particles. These phases are present in materials by design in order to control either the microstructure, such as the grain size, or mechanical properties, such as strength (Ref 7, 8).

However, some amounts of second phases are undesired. In any case, the presence of these nonhomogeneities alters the material behavior because of their differences in elastic properties with the matrix, such as in composite materials, or because of their interactions with dislocations. In both cases, these effects produce incompatibility stresses that lead to a Bauschinger effect.

The mechanisms of failure intrinsic to materials are flow localization and fracture. Localization tends to occur in the form of shear bands, either microbands, which tend to be crystallographic, or macrobands, which are not (Ref 9). Macroscopic necking in thin sheet occurs under either three-dimensional conditions (e.g., diffuse necking) or plane-strain conditions (e.g., localized, through-thickness necking). Ductile fracture is generally the result of a mechanism of void nucleation, growth, and coalescence (Ref 10). The associated microporosity leads to volume changes, although the matrix is plastically incompressible, and hydrostatic pressure affects the material behavior. At low temperature compared to the melting point, second phases are principally the sites of damage. The stress concentration around these phases leads to void nucleation, and growth occurs by plasticity. Coalescence is the result of plastic flow micro-localization of the ligaments between voids. At higher temperature, where creep becomes dominant, cavities nucleate at grain boundaries by various mechanisms, including grain sliding and vacancy coalescence. Generally, materials subjected to creep and superplastic forming exhibit higher porosity levels than those formed at lower temperature.

Constitutive Behavior

General Approach. Constitutive laws in materials generally consist of a state equation and evolution equations. The state equation describes the relationship between the strain rate ($\dot{\epsilon}$), stress (σ), temperature (T), and state variables (x^k), which represent the microstructural state of the material (Ref 11). The porosity of a material and a measure of the accumulated plastic deformation, such as the effective strain or the dislocation density, are a few examples of the variables x^k . The state equation can be expressed mathematically, for instance, in a scalar form for uniaxial deformation, as:

$$\dot{\epsilon} = \dot{\epsilon}(\sigma, T, x^k) \quad (\text{Eq 1})$$

The evolution equations describe the development of the microstructure through the change of the state variables and can take the form:

$$\dot{x}^k = \dot{x}^k(\sigma, T, x^k) \quad (\text{Eq 2})$$

Because slip plays a major role in plasticity, it is important to look at this mechanism in terms of both its kinetic effect on strain hardening and its geometrical effect on anisotropy. The Kocks and Mecking approach (Ref 12)

has laid the foundations for many subsequent studies by connecting the dislocation density to the flow stress. With this type of approach, it is possible to model the influence of parameters describing the microstructure, such as grain size, second phases, and solutes. Other approaches to strain hardening include dislocation dynamics and atomistic computation. However, these methods are very computationally intensive at this time and not appropriate for forming simulations.

The description of crystal plasticity has been very successful over the last few decades. This approach is based on the geometrical aspect of plastic deformation, slip and twinning in crystals, and on averaging procedures over a large number of grains. The crystallographic texture is the main input to these models, but other parameters, such as the grain shape, can also be included. It is a multiaxial approach and involves tensors instead of scalar variables. One of the outputs of a polycrystal model is the concept of the yield surface, which generalizes the concept of uniaxial yield stress for a multiaxial stress state. Polycrystal models can be used in multi-scale simulations of forming, but they are usually expensive in time, and the relevant question is to know if their benefit is worth the cost. Polycrystal modeling aspects have been treated in a large number of publications and books, such as in Ref 4, 13, and 14.

The state variables do not need to be connected to a specific microstructural feature. In this case, Eq 1 and 2 define a macroscopic model with state (or internal) variables. In fact, for forming applications, macroscopic models appear to be more appropriate. Because of the scale difference between the microstructure and a stamped part, the amount of microscopic material information necessary to store in a forming simulation would be excessively large. It is not possible to track all of the relevant microstructural features in detail. Therefore, lumping them all in a few macroscopic variables seems to be more appropriate and efficient.

Constitutive Modeling for Aluminum Alloys. At the continuum scale, for a multiaxial stress space, plastic deformation is well described with a yield surface, a flow rule, and a hardening law. The yield surface in stress space separates states producing elastic and elastoplastic deformation. It is a generalization of the tensile yielding behavior to multiaxial stress states. Plastic anisotropy is the result of the distortion of the yield surface shape due to the material microstructural state. Reference 15 discusses different phenomena attached to the yield surface shape at a macroscopic scale.

Certain properties of the continuum yield functions can be obtained from microstructural considerations. Bishop and Hill (Ref 16) showed that for a single crystal obeying the Schmid law (i.e., dislocation glide occurs when the resolved shear stress on a slip system reaches a critical value), the resulting yield surface is convex, and

the associated strain increment is normal to it. Furthermore, they extended this result to a polycrystal by averaging the behavior of a representative number of grains in an elementary volume without making any assumption about the interaction modes between grains or the uniformity of the deformation gradient. These results provide a good support for the use of the associated flow rule, which stipulates that the strain rate (increment) is normal to the yield surface.

Regardless of the shape of the yield surface, strain hardening can be isotropic or anisotropic. The former corresponds to an expansion of the yield surface without distortion. Any other form of hardening is anisotropic and leads to different properties in different directions after deformation, even if the material is initially isotropic. Whether the yield surface expands, translates, or rotates as plastic deformation proceeds, a shape must be defined to account for initial anisotropy.

If the yield surface distorts during deformation, a unique shape can still be used to describe an average material response over a certain deformation range (Ref 17). Because mechanical data are used as input, these models can still be relatively accurate when the strain is moderate. This is typically the case for sheet forming. However, for larger strains and for abrupt strain path changes, evolution is an issue (for instance, see Ref 18 to 26). Nevertheless, the description of plastic anisotropy based on the concept of yield surfaces and isotropic hardening is convenient and time-efficient for engineering applications such as forming-process simulations. Moreover, the translation of a yield surface (kinematic hardening), which captures phenomena such as the Bauschinger effect, can be easily integrated in an FE formulation.

In view of the previous section, it is obvious that it is difficult to develop constitutive models for forming applications that capture all the macroscopic and microscopic phenomena involved in plastic deformation and ductile fracture. Therefore, the discussion is mostly restricted to behavior where isotropic hardening is a good approximation. Practically, this approach is robust and reasonably accurate in many situations. In classical plasticity, the material description is fully defined using the following set of equations:

$$\Phi(\sigma_{ij}) = \bar{\sigma} \quad (\text{yield function/effective stress}) \quad (\text{Eq 3})$$

$$\bar{\sigma} = h(\bar{\epsilon}) \quad (\text{yield condition}) \quad (\text{Eq 4})$$

$$\dot{\epsilon}_{ij} = \dot{\lambda} \frac{\partial \Phi}{\partial \sigma_{ij}} \quad (\text{associated or normality flow rule}) \quad (\text{Eq 5})$$

where σ_{ij} and $\dot{\epsilon}_{ij}$ are the stress and strain-rate tensor components, and $\dot{\lambda}$ is a proportionality factor. The overdot indicates the derivative with respect to time. The variable h is the strain-hardening law (function), which expands the

yield surface as plastic deformation accumulates. The symbol $\bar{\sigma}$ is the effective stress, and $\bar{\epsilon}$ is the work-equivalent effective strain defined incrementally as:

$$\bar{\sigma} \dot{\bar{\epsilon}} = \sum_{i,j} \sigma_{ij} \dot{\epsilon}_{ij} = \sigma_{ij} \dot{\epsilon}_{ij} \quad (\text{Eq 6})$$

The last expression is an abbreviation of the summation using the Einstein convention. Any repeated index indicates the summation of a product over 1 to 3. Note that this formulation (Eq 3 to 6) is consistent with the general framework defined by Eq 1 and 2. The problem reduces to the definitions of the hardening law and yield function, h and $\bar{\sigma}$ (or Φ), respectively.

The Swift power law (Ref 27), a very popular approximation of the hardening function h , is defined as:

$$h(\bar{\epsilon}) = K(\epsilon_0 + \bar{\epsilon})^n \quad (\text{Eq 7})$$

where K and n are the strength coefficient and strain-hardening exponent, respectively. The symbol ϵ_0 is another coefficient that, if equal to zero, reduces Eq 7 to the Hollomon (Ref 28) hardening law. However, one of the outcomes of the dislocation-based Kocks and Mecking approach mentioned previously is that, macroscopically, the strain-hardening behavior for aluminum alloys can be better described with the Voce law (Ref 29):

$$h(\bar{\epsilon}) = A - B \exp(-C\bar{\epsilon}) \quad (\text{Eq 8})$$

where A , B , and C are constant coefficients. Therefore, this equation is often preferred to represent the hardening behavior of aluminum alloys, although, as discussed in the section "Test Data Analysis" in this article, is necessary to understand the consequences of the fitting procedure on the modeled material response. It can be assumed that the effects of temperature and strain rate can be included in the formulation through h , for instance, using $h = h(\bar{\epsilon}, \dot{\bar{\epsilon}}, T)$. As an example, a practical way to include strain-rate effects is to separate this variable from strain hardening through the use of the strain-rate sensitivity parameter m :

$$h = g(\bar{\epsilon}) \left(\frac{\dot{\bar{\epsilon}}}{\dot{\bar{\epsilon}}_r} \right)^m \quad (\text{Eq 9})$$

where g is the strain-hardening law at the reference strain rate $\dot{\bar{\epsilon}}_r$, and m is the strain-rate sensitivity parameter defined as:

$$m = \left. \frac{\partial \ln(\sigma)}{\partial \ln(\dot{\bar{\epsilon}})} \right|_{\epsilon} \quad (\text{Eq 10})$$

It is worthy to note that the strain-rate sensitivity parameter m is very close to zero for most aluminum alloys at room temperature. However, m can be slightly higher at low temperature and relatively large at higher temperature (Ref 30), particularly for conditions of superplastic deformation (Ref 6).

For cubic metals, there are usually enough potentially active slip systems to accommodate

any shape change imposed to the material. Compressive and tensile yield strengths are virtually identical, and yielding is not influenced by the hydrostatic pressure. The yield surface of such materials is usually represented adequately by an even function of the principal values S_k of the stress deviator \mathbf{s} , such as proposed by Hershey (Ref 31) and Hosford (Ref 32), that is:

$$\phi = |S_1 - S_2|^a + |S_2 - S_3|^a + |S_3 - S_1|^a = 2\bar{\sigma}^a \quad (\text{Eq 11})$$

With respect to the stress tensor components σ_k , the deviatoric stresses S_k are given by:

$$S_k = \sigma_k - (\sigma_1 + \sigma_2 + \sigma_3)/3 \quad (\text{Eq 12})$$

The yield function in Eq 11 can be framed into the general form of Eq 3, using the simple transformation $\Phi = (\phi/2)^{1/a}$. The exponent "a" is related to the crystal structure of the lattice, that is, 6 for body-centered cubic (bcc) and 8 for face-centered cubic (fcc) materials (Ref 33, 34). This was established as a result of many polycrystal simulations. Therefore, although this model is macroscopic, it contains some information pertaining to the structure of the material.

For the description of incompressible plastic anisotropy, many yield functions have been suggested based on the isotropic-hardening assumption (Ref 35–39). Among them, Cazacu and Barlat (Ref 39) introduced a general formulation that originated from the rigorous theory of representation of tensor functions. However, with this approach, the conditions for the convexity of the yield surface are difficult to impose. As mentioned previously in this section, the convexity has a physical basis, and, in addition, this property ensures numerical stability in computer simulations. For this reason, a particular case of this general theory, which is based on linearly transformed stress components, has received more attention. Barlat et al. (Ref 37) applied this method to a general stress state in an orthotropic material, and Karafillis and Boyce (Ref 38) generalized it as the so-called isotropic plasticity equivalent theory, with a more general yield function and a linear transformation that can accommodate lower material symmetry. Cazacu et al. (Ref 40) proposed a criterion based on a linear transformation that accounts for the strength-differential effect, particularly prominent in hexagonal close-packed metals.

Because the aforementioned functions are not able to capture the anisotropic behavior of aluminum sheet to a desirable degree of accuracy, Barlat et al. (Ref 41, 42) introduced two linear transformations operating on the sum of two yield functions in the case of plane stress and general stress states, respectively. Bron and Besson (Ref 43) further extended Karafillis and Boyce's approach to two linear transformations. These recently proposed yield functions include more anisotropy coefficients and therefore give a better description of the anisotropic properties of a material. This is particularly obvious for

the description of uniaxial tension properties (Ref 42).

Extensions of Eq 11 to planar anisotropy for plane stress and general stress states are briefly summarized in the section "Anisotropic Yield Functions" in this article. Both formulations are based on two linear transformations of the stress deviator. The two linear transformations can be expressed as:

$$\begin{aligned} \tilde{\mathbf{s}}' &= \mathbf{C}' \mathbf{s} = \mathbf{C}' \mathbf{T} \boldsymbol{\sigma} = \mathbf{L}' \boldsymbol{\sigma} \\ \tilde{\mathbf{s}}'' &= \mathbf{C}'' \mathbf{s} = \mathbf{C}'' \mathbf{T} \boldsymbol{\sigma} = \mathbf{L}'' \boldsymbol{\sigma} \end{aligned} \quad (\text{Eq 13})$$

where \mathbf{T} is a matrix that transforms the Cauchy stress tensor $\boldsymbol{\sigma}$ to its deviator \mathbf{s} :

$$\mathbf{T} = \frac{1}{3} \begin{bmatrix} 2 & -1 & -1 & 0 & 0 & 0 \\ -1 & 2 & -1 & 0 & 0 & 0 \\ -1 & -1 & 2 & 0 & 0 & 0 \\ 0 & 0 & 0 & 3 & 0 & 0 \\ 0 & 0 & 0 & 0 & 3 & 0 \\ 0 & 0 & 0 & 0 & 0 & 3 \end{bmatrix} \quad (\text{Eq 14})$$

In Eq 13, $\tilde{\mathbf{s}}'$ and $\tilde{\mathbf{s}}''$ are the linearly transformed stress deviators, while \mathbf{C}' and \mathbf{C}'' (or \mathbf{L}' and \mathbf{L}'') are the matrices containing the anisotropy coefficients. Specific forms of these matrices are given subsequently for materials exhibiting the orthotropic symmetry, that is, with three mutually orthogonal planes of symmetry at each point of the continuum, such as in sheet metals or tubes. The unit vectors describing the symmetry axes are denoted by \mathbf{x} , \mathbf{y} , and \mathbf{z} , which, for sheet materials, correspond to the rolling, transverse, and normal directions, respectively.

Anisotropic Yield Functions. For plane stress, these two linear transformations can be defined as:

$$\begin{aligned} \begin{bmatrix} \tilde{s}'_{xx} \\ \tilde{s}'_{yy} \\ \tilde{s}'_{xy} \end{bmatrix} &= \begin{bmatrix} \alpha_1 & 0 & 0 \\ 0 & \alpha_2 & 0 \\ 0 & 0 & \alpha_7 \end{bmatrix} \begin{bmatrix} s_{xx} \\ s_{yy} \\ s_{xy} \end{bmatrix} \\ \begin{bmatrix} \tilde{s}''_{xx} \\ \tilde{s}''_{yy} \\ \tilde{s}''_{xy} \end{bmatrix} &= \frac{1}{3} \begin{bmatrix} 4\alpha_5 - \alpha_3 & 2\alpha_6 - 2\alpha_4 & 0 \\ 2\alpha_3 - 2\alpha_5 & 4\alpha_4 - \alpha_6 & 0 \\ 0 & 0 & 3\alpha_8 \end{bmatrix} \\ &\quad \times \begin{bmatrix} s_{xx} \\ s_{yy} \\ s_{xy} \end{bmatrix} \end{aligned} \quad (\text{Eq 15})$$

By denoting \tilde{S}'_j and \tilde{S}''_j the principal values of the tensors $\tilde{\mathbf{s}}'$ and $\tilde{\mathbf{s}}''$ defined previously, the plane-stress anisotropic yield function Yld2000-2d is then defined as:

$$\phi = |\tilde{S}'_1 - \tilde{S}'_2|^a + |2\tilde{S}''_2 + \tilde{S}''_1|^a + |2\tilde{S}''_1 + \tilde{S}''_2|^a = 2\bar{\sigma}^a \quad (\text{Eq 16})$$

Note that this formulation is isotropic and reduces to Eq 11 if \mathbf{C}' and \mathbf{C}'' are both equal to the identity matrix. It also reduces to the classical von Mises and Tresca yield functions if $a = 2$ (or 4) and $a = 1$ (or ∞), respectively. More

details regarding Yld2000-2d are given in Ref 41 and 44.

For a full three-dimensional stress state, the linear transformations can be expressed in the most general form with the following matrices:

$$\mathbf{C}' = \begin{bmatrix} 0 & -c'_{12} & -c'_{13} & 0 & 0 & 0 \\ -c'_{21} & 0 & -c'_{23} & 0 & 0 & 0 \\ -c'_{31} & -c'_{32} & 0 & 0 & 0 & 0 \\ 0 & 0 & 0 & c'_{44} & 0 & 0 \\ 0 & 0 & 0 & 0 & c'_{55} & 0 \\ 0 & 0 & 0 & 0 & 0 & c'_{66} \end{bmatrix};$$

$$\mathbf{C}'' = \begin{bmatrix} 0 & -c''_{12} & -c''_{13} & 0 & 0 & 0 \\ -c''_{21} & 0 & -c''_{23} & 0 & 0 & 0 \\ -c''_{31} & -c''_{32} & 0 & 0 & 0 & 0 \\ 0 & 0 & 0 & c''_{44} & 0 & 0 \\ 0 & 0 & 0 & 0 & c''_{55} & 0 \\ 0 & 0 & 0 & 0 & 0 & c''_{66} \end{bmatrix}$$

(Eq 17)

The anisotropic yield function Yld2004-18p is defined as:

$$\begin{aligned} \phi = \phi(\tilde{S}'_i, \tilde{S}'_j) &= |\tilde{S}'_1 - \tilde{S}'_1|^a + |\tilde{S}'_1 - \tilde{S}'_2|^a \\ &+ |\tilde{S}'_1 - \tilde{S}'_3|^a + |\tilde{S}'_2 - \tilde{S}'_1|^a + |\tilde{S}'_2 - \tilde{S}'_2|^a \\ &+ |\tilde{S}'_2 - \tilde{S}'_3|^a + |\tilde{S}'_3 - \tilde{S}'_1|^a + |\tilde{S}'_3 - \tilde{S}'_2|^a \\ &+ |\tilde{S}'_3 - \tilde{S}'_3|^a = 4\bar{\sigma}^a \end{aligned}$$

(Eq 18)

This formulation is isotropic if all the coefficients c'_{ij} and c''_{ij} reduce to unity. The reader is referred to Ref 42 for additional information about this model.

Strain-Rate Potentials. In order to represent the rate-insensitive plastic behavior of materials phenomenologically, it is typical, as explained previously, to use a yield surface, the associated flow rule, and a hardening law. Ziegler (Ref 45) and Hill (Ref 46) have shown that, based on the work-equivalence principle, Eq 6, a meaningful strain-rate potential can be associated to any convex stress potential (yield surface). Therefore, an alternate approach to describe plastic anisotropy is to provide a strain-rate potential $\Psi(\dot{\boldsymbol{\epsilon}}) = \bar{\epsilon}$, expressed as a function of the traceless plastic strain-rate tensor $\dot{\boldsymbol{\epsilon}}$, the gradient of which leads to the direction of the stress deviator \mathbf{s} , that is:

$$s_{ij} = \mu \frac{\partial \Psi}{\partial \dot{\epsilon}_{ij}} \quad (\text{Eq 19})$$

In the previous equation, μ is a proportionality factor necessary to scale the stress deviator. Note the similarity between Eq 19 and Eq 5. This approach has been used for the description of the plastic behavior of fcc single crystals (Ref 47), bcc polycrystals (Ref 48–50), and cubic polycrystals (Ref 51–52). In the latter works,

the strain-rate potential $\Psi = (\psi/k)^{1/b}$ for an incompressible isotropic material was defined using:

$$\begin{aligned} \psi &= \left| \frac{2\dot{E}_1 - \dot{E}_2 - \dot{E}_3}{3} \right|^b + \left| \frac{2\dot{E}_2 - \dot{E}_3 - \dot{E}_1}{3} \right|^b \\ &+ \left| \frac{2\dot{E}_3 - \dot{E}_1 - \dot{E}_2}{3} \right|^b = |\dot{E}_1|^b + |\dot{E}_2|^b + |\dot{E}_3|^b \\ &= k\bar{\epsilon}^b \end{aligned}$$

(Eq 20)

where \dot{E}_i represents the principal values of the plastic strain-rate tensor $\dot{\boldsymbol{\epsilon}}$, and $\bar{\epsilon}$ is the effective strain rate defined using the plastic work equivalence principle with the effective stress $\bar{\sigma}$ (Eq 6). The constant k defines the size of the potential, and the exponent “ b ” was shown to be $3/2$ and $4/3$ for an optimal representation of bcc and fcc materials, respectively. For orthotropic materials, the principal values \dot{E}_i of a linearly transformed plastic strain rate tensor $\dot{\boldsymbol{\epsilon}}$, that is:

$$\dot{\boldsymbol{\epsilon}} = \mathbf{B}\dot{\boldsymbol{\epsilon}} \quad (\text{Eq 21})$$

where \mathbf{B} is the matrix containing six anisotropy coefficients, are substituted for \dot{E}_i in Eq 20. This formulation reduces to isotropy when \mathbf{B} becomes the identity matrix (i.e., $\dot{\boldsymbol{\epsilon}} = \dot{\boldsymbol{\epsilon}}$). However, it is generally accepted that six coefficients are not sufficient to describe the plastic behavior of anisotropic aluminum alloy sheets very accurately. Therefore, a formulation that accounts for two linear transformations on the traceless plastic strain-rate tensor $\dot{\boldsymbol{\epsilon}}$ was recently introduced:

$$\dot{\boldsymbol{\epsilon}}' = \mathbf{B}'\dot{\boldsymbol{\epsilon}} = \mathbf{B}'\mathbf{T}\dot{\boldsymbol{\epsilon}} \quad (\text{Eq 22})$$

$$\dot{\boldsymbol{\epsilon}}'' = \mathbf{B}''\dot{\boldsymbol{\epsilon}} = \mathbf{B}''\mathbf{T}\dot{\boldsymbol{\epsilon}} \quad (\text{Eq 23})$$

where $\dot{\boldsymbol{\epsilon}} = \mathbf{T}\dot{\boldsymbol{\epsilon}}$ is another expression of the traceless plastic strain-rate tensor, necessary to ensure that the strain-rate potential is a cylinder through the transformation represented by \mathbf{T} defined previously. The specific strain-rate potential, called Srp2004-18p, was postulated (Ref 53):

$$\begin{aligned} \psi &= \psi(\tilde{E}'_i, \tilde{E}''_j) = |\tilde{E}'_1|^b + |\tilde{E}'_2|^b + |\tilde{E}'_3|^b \\ &+ |\tilde{E}''_2 + \tilde{E}''_3|^b + |\tilde{E}''_3 + \tilde{E}''_1|^b + |\tilde{E}''_1 + \tilde{E}''_2|^b \\ &= (2^{2-b} + 2)\bar{\epsilon}^b \end{aligned}$$

(Eq 24)

where \tilde{E}'_i and \tilde{E}''_j are the principal values of the tensors $\dot{\boldsymbol{\epsilon}}'$ and $\dot{\boldsymbol{\epsilon}}''$. Here, the anisotropy coefficients are contained in matrices \mathbf{B}' and \mathbf{B}'' , both of a form similar to \mathbf{C}' and \mathbf{C}'' in Eq 17.

Experiments and Constitutive Parameters

Testing Methods. Multiaxial experiments have been used to characterize a yield surface, and many issues have been addressed (Ref 54,

55). Recently, Banabic et al. (Ref 56) improved a procedure for biaxial testing of cruciform specimens machined from thin sheets, and for measuring the first quadrant of the yield locus (both stresses positive). In these tests, the onset of plastic deformation is detected from temperature measurements of specimens using an infrared thermocouple positioned at an optimized distance. This method is based on the fact that the specimen temperature drops first due to thermoelastic cooling and then rises significantly when dissipative plastic flow initiates. In spite of this and other types of improvements, multiaxial testing is tedious, difficult to conduct and interpret, and not suitable for quick characterization of anisotropy. This is more a technique for careful verifications of concepts and theories. Therefore, more practical and time-efficient methods are required to test materials and identify material coefficients in constitutive equations, in particular for sheets.

Anisotropic properties can be assessed by performing uniaxial tension tests in the \mathbf{x} and \mathbf{y} axes (rolling and transverse directions, respectively) and in a direction at θ degrees with respect to \mathbf{x} . Practically, the anisotropy is characterized by the yield stresses σ_0 , σ_{45} , σ_{90} ; the r -values (width-to-thickness strain ratio in uniaxial tension) r_0 , r_{45} , r_{90} ; and their respective averages $\bar{q} = (q_0 + 2q_{45} + q_{90})/4$ and variations $\Delta\bar{q} = (q_0 - 2q_{45} + q_{90})/2$. For a better characterization of anisotropy, tensile specimens are cut from a sheet at angles of 0, 15, 30, 45, 60, 75, and 90° from the rolling direction. Tension tests are usually conducted at room temperature (RT), and standard (ASTM International) methods are used to measure the yield stresses and r -values. For some aluminum alloys, however, the stress-strain curve exhibits serrations, resulting from nonhomogeneous deformation of the tensile specimen. For instance, Fig. 1 shows the engineering tensile stress-strain curves measured in the 0, 45, and 90° directions at RT for a 5019A-O sheet sample. Because this phenomenon is due to inhomogeneous plastic deformation, the plastic strains measured with extensometers are not reliable and can lead to erroneous r -values. In order to overcome this problem, tension tests can be conducted at a somewhat higher temperature, where serrated flow is suppressed. For instance, Fig. 1 shows the engineering stress/engineering strain curves in the 0, 45, and 90° tension directions measured at RT and at a temperature of 93 °C (200 °F) for a 5019A-H48 sheet sample (Ref 57).

The balanced biaxial yield stress (σ_b) is an important parameter to measure for sheet material characterization. This stress can be obtained by conducting a hydraulic bulge test (Ref 58). Figure 2 shows a schematic diagram of this test in which a sheet blank is clamped between a die with a large circular opening and a holder. A pressure, p , is gradually applied under the blank, which bulges in a quasi-spherical shape. The radius of curvature, R , and strains at the pole of

the specimen are measured independently, using mechanical or optical instruments. The stress $\sigma = pR/2t$ is simply obtained from the membrane theory using the thickness, t . This test is interesting not only because it gives information on the yield surface, but also because it allows measurements of the hardening behavior up to strains of approximately twice those achieved in uniaxial tension. This is because geometrical instabilities occur during uniaxial tension (see the section “Strain-Based Forming-Limit Curves” in this article). However, the yield point is not well defined in the bulge test because of the low curvature of the specimen in the initial stage of deformation. As for uniaxial tension, this test can be conducted at different strain rates in order to assess the strain-rate sensitivity parameter m .

Because the biaxial stress state in the bulge test is not exactly balanced, measures of the corresponding strain state may lead to substantial errors. This is because the yield locus curvature

is usually high in this stress state. Barlat et al. (Ref 41) proposed the disk-compression test, which gives a measure of the flow anisotropy for a balanced biaxial stress state, assuming that hydrostatic pressure has no influence on plastic deformation. In this test, a 12.7 mm (0.5 in.) disk is compressed through the thickness direction of the sheet. The strains measured in the x and y directions lead to a linear relationship in which the slope is denoted by r_b by analogy to the r -value in uniaxial tension:

$$r_b = d\epsilon_{yy}^p / d\epsilon_{xx}^p \tag{Eq 25}$$

This parameter is a direct measure of the slope of the yield locus at the balanced biaxial stress state. Figure 3 shows deformed specimens for 6111-T4 aluminum alloy sheet samples processed with two different routes, and the corresponding strain measures performed during this test. Pöhlandt et al. (Ref 59) proposed to determine the parameter r_b using the in-plane biaxial tension test.

Other tests can be used to characterize the material behavior of sheet samples. Directional tension of wide specimens can be used to characterize plane-strain tension anisotropy (Ref 60, 61). This test does not produce a uniform state of stress within the specimen and generally leads to more experimental scatter than the uniaxial test.

Simple shear tests (Ref 62) can be carried out to characterize the anisotropic behavior of the simple shear flow stress. A relatively simple device mounted on a standard tensile machine is needed for this test. A rectangular specimen is clamped with two grips, which move in opposite directions relative to each other (Fig. 4). By simply reversing the direction of the grip displacements, forward and reverse loading sequences can be conducted in order to measure the Bauschinger effect. In-plane tension-compression tests of thin sheets have also been used for this purpose (Ref 63, 64), but special precautions need to be taken because of the

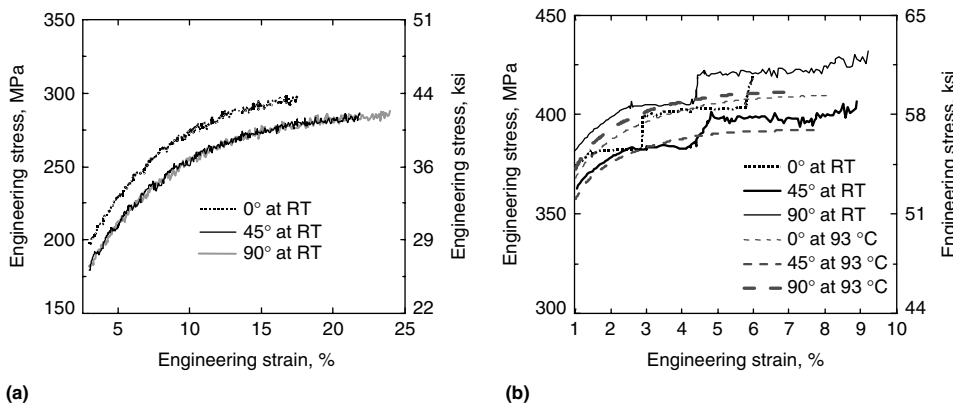


Fig. 1 Stress-strain curves. (a) Aluminum alloy 5019A-O sheet sample for three tensile directions at room temperature (RT). (b) Aluminum alloy 5019A-H48 sheet sample for three tensile directions and two temperatures. Source: Ref 57

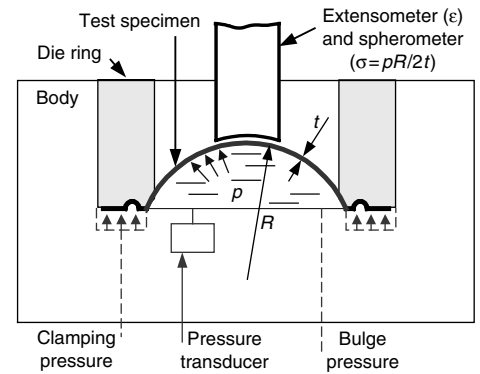


Fig. 2 Schematic illustration of the bulge test. p , pressure; R , radius of curvature; t , thickness. Source: Ref 17

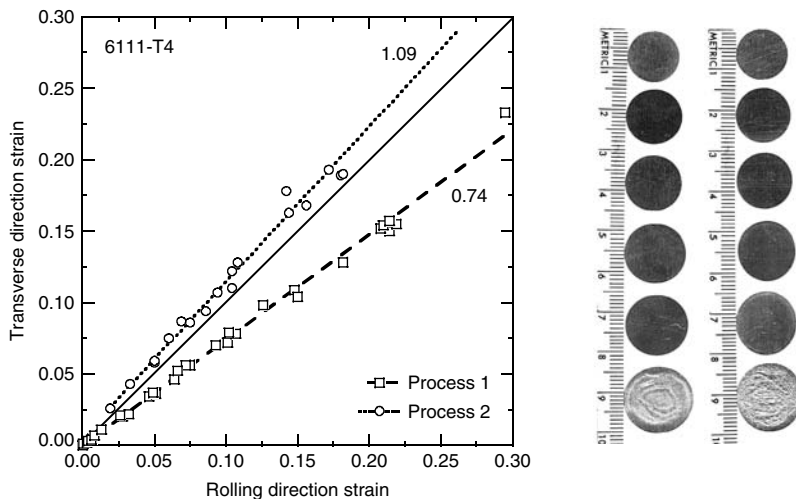


Fig. 3 Disk-compression test results for an aluminum alloy 6111-T4 sheet sample processed using two different flow paths, and selected test specimens. Source: Ref 17



Fig. 4 Simple shear test device

buckling tendency of the specimen during the compressive step.

Although the previously described tests and other experimental procedures are available to test materials in different stress states, it is not always possible to probe all of them. In this case, microstructural modeling can be used to replace the missing experimental data. For instance, the resistance to through-the-thickness shear of a sheet, σ_s , is not readily available from experimental measurements. However, crystal plasticity with a measure of the crystallographic texture of the sheet can be used to compute σ_s . A rougher approximation is to assume that this value is equal to the isotropic shear stress, which, using Eq 11 and 12, for pure shear ($\sigma_2 = -\sigma_1$, $\sigma_3 = 0$) is equal to:

$$\frac{\sigma_s}{\bar{\sigma}} = \frac{1}{(2^{a-1} + 1)^{1/a}} \quad (\text{Eq 26})$$

Test Data Analysis. From the experimental tests, it is necessary to extract the right information that is most suitable for the identification of the constitutive parameters. For instance, the yield stresses can be used as input data to calculate the anisotropic yield function coefficients. However, as mentioned previously, the yield stress from the bulge test is not very accurate. Moreover, any stress at yield is determined in the region of the stress-strain curve where the slope is the steepest, which may involve additional inaccuracy. Finally, the yield stress is associated with a very small plastic strain and may not reflect the anisotropy of the material over a larger strain range. For these reasons, the flow stresses at equal amount of plastic work along different loading paths could be selected as input data instead of the yield stress. Figure 5 shows how the flow stresses in tension and balanced biaxial tension (bulge test) can be defined at equal amounts of plastic work ($w_p = \int \sigma_{ij} \dot{\epsilon}_{ij} d\tau_{ij}$, where τ is the time). For many aluminum alloys, experimental observations show that after a few percent plastic strain, the flow stress anisotropy does not vary significantly, as illustrated by Fig. 6(a) and (b).

In the examples shown later in this article, the stress-strain curves employed in the forming simulations were measured using the bulge test, whenever possible. This test is important be-

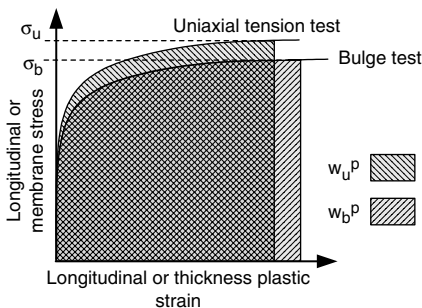


Fig. 5 Flow stresses at equivalent amount of plastic work in uniaxial tension, W_u^p , and balanced biaxial tension (bulge test), W_b^p , i.e., for $W_u^p = W_b^p$

cause extrapolation of uniaxial tension curves with the Voce law usually leads to an underestimation of strain hardening for strains higher than the limit of uniform elongation in tension. This is demonstrated in Fig. 6(c), which shows the Voce approximation of the bulge test data using two different strain ranges, that is, from zero up to strains of 0.2 and 0.53. These strain ranges are typical for uniaxial tension and balanced biaxial tension (bulge), respectively, for annealed aluminum alloys. This figure illustrates the risks of extrapolating flow stresses beyond the range of strains that was used for the fit. The stress-strain curve extrapolated

from the fit in the strain range 0–20% exhibits a much lower rate of strain hardening ($d\sigma/d\epsilon$) after 25% deformation compared to the curve obtained experimentally with the bulge test.

Similar remarks hold for r -values, which can be defined as instantaneous quantities near yield or as the standard slope of the width strain/thickness strain curve over a given deformation range in tension. On one hand, the yield stresses and instantaneous r -values at yield seem to be appropriate to define the coefficients of the yield function. On the other hand, flow stresses defined at a given amount of plastic work and standard r -values can characterize the average behavior of the material over a finite deformation range. These values are more suitable and more descriptive of the average response of the material for sheet forming simulations. In this case, it would be more appropriate to talk about flow function and flow surface instead of yield function and yield surface, although, mathematically, yield or flow functions are identical concepts.

The anisotropy coefficients are calculated from flow stresses and r -values. For the yield function Yld2000-2d, the eight coefficients are computed numerically, using a Newton-Raphson numerical solver using eight input data: the flow stresses σ_0 , σ_{45} , σ_{90} , σ_b and the r -values r_0 , r_{45} , r_{90} , and r_b (Ref 41). For the yield function Yld2004-18p, the 18 coefficients are computed numerically with an error-minimization method using 16 experimental input data: the flow stresses σ_0 , σ_{15} , σ_{30} , σ_{45} , σ_{60} , σ_{75} , σ_{90} , σ_b and the r -values r_0 , r_{15} , r_{30} , r_{45} , r_{60} , r_{75} , r_{90} , and r_b . The remaining inputs, related to the through-the-thickness properties, are assumed to be equal to the isotropic values or are computed with a crystal-plasticity model (Ref 42). As an illustration of Yld2000-2d and Yld2004-18p, the predicted directionalities of the uniaxial flow stress and r -value for a 5019A-H48 aluminum alloy sheet sample are compared with experimental results in Fig. 7. This figure also shows that the yield function Yld91 (Ref 37), which uses only one linear transformation on the stress tensor, cannot properly capture the experimental variation of the r -value.

Tensile Instability

The success of a sheet-forming operation can be limited by several phenomena, such as plastic flow localization, fracture, and buckling. For a given forming operation, the sheet may undergo deformation up to a given strain prior to failure by one of the limiting phenomena. In this section, analyses for plastic flow localization are discussed.

Strain-Based Forming-Limit Curves. The forming-limit curve (FLC) corresponds to the maximum admissible local strains achievable just before necking. This curve is usually plotted on axes representing the major (ϵ_1) and the minor (ϵ_2) strains in the plane of a sheet. Actually, for anisotropic materials, the major strain in the

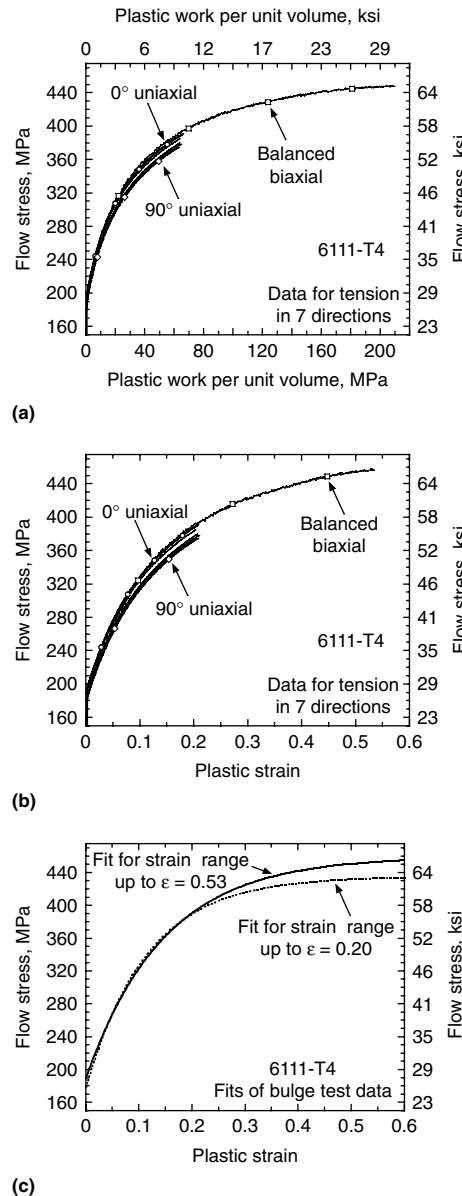


Fig. 6 Flow stress as a function of (a) plastic work or (b) plastic strain for an aluminum alloy 6111-T4 sheet sample measured in balanced biaxial tension (bulge test) and uniaxial tension for directions at every 15° from the rolling direction. (c) Fit of Voce law to bulge-test data over two different strain ranges

rolling direction is different from the major strain in the transverse or in any other direction. Nevertheless, this convention is adopted in this section, although it lacks generality.

Different models have been proposed in the past to calculate the FLC. Swift (Ref 27) derived equations to predict diffuse necking. In real parts, however, the maximum admissible strains are typically limited by localized (through-thickness) necking, and Swift's equations have only limited applicability. The relationships giving the limit strain under local necking conditions were developed by Hill (Ref 65). His theory predicts that localized necking occurs in the characteristic directions of zero extension in the plane of the sheet. However, Hill's theory can only predict localized necking if one of the strains in the plane of the sheet is negative, that is, between uniaxial and plane-strain tension. This does not agree with experiments, because necking also occurs in stretching processes for which both in-plane principal strains are positive. To explain such behavior, Marciniak and Kuczynski (Ref 66) proposed an analysis in which the sheet metal is supposed to contain a region of local imperfection. Heterogeneous plastic flow develops and eventually localizes

in the imperfection. The Marciniak and Kuczynski (MK) model can predict the FLC when minor strains are either positive or negative. It was initially developed within the flow theory of plasticity, using quadratic plastic potentials. However, for balanced biaxial stretching ($\epsilon_2 = \epsilon_1$) and within the classical plasticity approach (J_2 flow theory), this model largely overestimates the limit strains. Therefore, Hutchinson and Neale (Ref 67) extended this model using the deformation theory of plasticity and were able to make predictions that were in better agreement with the experiments. Many other works have been published to show the influence of various parameters on calculated forming limits (for instance, Ref 68). Stören and Rice (Ref 69) gave another description of the plastic flow localization using a bifurcation analysis.

In the MK model, an infinite sheet metal is assumed to contain an imperfection, which is represented as a linear band of infinite size whose thickness t^I is smaller than the thickness of the homogeneous region of the sheet, t . The superscript "I" is used here for all the variables in the imperfection. Quantitatively, this two-zone material is characterized by parameter D:

$$D = 1 - t^I/t \tag{Eq 27}$$

There is no imperfection when both thicknesses are identical, that is, when parameter D reduces to 0, and no plastic flow localization can be predicted with the MK model. However, if D has a starting value larger than zero, it will increase as plastic deformation proceeds. At each step of the calculation, the ratio of the effective strain rate in the homogeneous region ($\dot{\epsilon}$) to the effective strain rate in the imperfection ($\dot{\epsilon}^I$) is evaluated. Plastic flow localization occurs when this ratio approaches 0. The basic equations of the MK model are related to equilibrium and compatibility requirements. The first condition indicates that the force perpendicular to the necking band is transmitted from the homogeneous region to the imperfection, whereas, the second requirement indicates that the elongation in the direction of the necking band is identical in both regions. For materials exhibiting isotropy or planar isotropy (same properties in any direction in the plane of the sheet), the main equilibrium equation of the MK model reduces to the following form:

$$[1 - D] \frac{h(\bar{\epsilon}^I)}{h(\bar{\epsilon})} \left[\frac{\bar{\sigma}_1^I}{\bar{\sigma}_1} \right] = 1 \tag{Eq 28}$$

where $h(\bar{\epsilon})$ is the hardening law, and $\bar{\sigma}_1 = \sigma_1/\bar{\sigma}$ is the maximum principal stress normalized by the effective stress.

The MK model also suggests the necking direction per se. In the negative ρ range ($\rho = d\epsilon_2/d\epsilon_1 \leq 0$) lying between uniaxial tension and plane-strain tension, the necking direction is at an angle with respect to the maximum principal strain. However, in the biaxial stretching range (both ϵ_1 and ϵ_2 are positive), necking occurs mainly in a direction perpendicular to the major

principal strain, which corresponds to the assumption of Eq 28. The product of the three quantities within the square brackets on the left side of Eq 28 must be constant. The first quantity ($1 - D$) is related to the imperfection, and it decreases when D increases. However, the two other quantities tend to balance the equation. Because of the smaller thickness, there is more plastic deformation and consequently more plastic work in the necking band than in the homogeneous region. Therefore, the ratio $h(\bar{\epsilon}^I)/h(\bar{\epsilon})$ becomes larger than 1. In addition, it has been shown (Ref 70) that the stress state in the imperfection moves toward a plane-strain state. Thus, the ratio $\bar{\sigma}_1^I/\bar{\sigma}_1$ also increases, because the yield stress is at a maximum stationary value for plane strain. As a result, the increasing defect size is counterbalanced by two types of material hardening. The first one is strain hardening, whereas the second one, termed yield-surface shape hardening (Ref 71), is related to the yield surface shape. In particular, it has been shown that the ratio $P = \sigma_y/\sigma_b$ of the plane-strain to balanced biaxial yield stresses is a good parameter to evaluate sheet stretchability (Ref 71). When this ratio is much larger than 1, as it is for an isotropic von Mises material ($P \approx 1.15$), the predicted limit strain for balanced biaxial stretching is very large. However, the isotropic Tresca material, for which $P = 1$, exhibits a very low forming limit for the same strain path (Ref 72). For plane-strain tension, the ratio $\bar{\sigma}_1^I/\bar{\sigma}_1$ is always equal to 1, regardless of the yield surface shape, and Eq 28 becomes:

$$(1 - D) \frac{h(\bar{\epsilon}^I)}{h(\bar{\epsilon})} = 1 \tag{Eq 29}$$

This explains why the plane-strain deformation state always leads to the lowest forming limit. Materials cannot take advantage of the yield-surface shape-hardening effect in this deformation state, and only strain hardening is available to counterbalance the imperfection growth.

The previous analysis can also be used to explain qualitatively the effects of strain-rate sensitivity and kinematic hardening on formability. For strain-rate-sensitive materials, the left side of Eq 28 is multiplied by an additional (strain-rate) hardening term, $(\dot{\epsilon}^I/\dot{\epsilon})^m$, where m is the strain-rate sensitivity parameter. Because the strain rate is larger in the necking band than in the homogeneous region, this parameter is larger than 1, when m is positive, and therefore tends to stabilize plastic flow. If kinematic hardening applies, the yield surface moves toward the stress or strain-rate direction without changing its shape. This has the effect of decreasing the ratio P and consequently the forming limit, as predicted by Tvergaard (Ref 73).

Needleman and Triantafyllidis (Ref 74) showed that the imperfection can be attributed to material heterogeneities. In particular, it can be viewed as a difference in surface area transmitting the load. Hence, it can be assumed that internal damage mostly is responsible for the

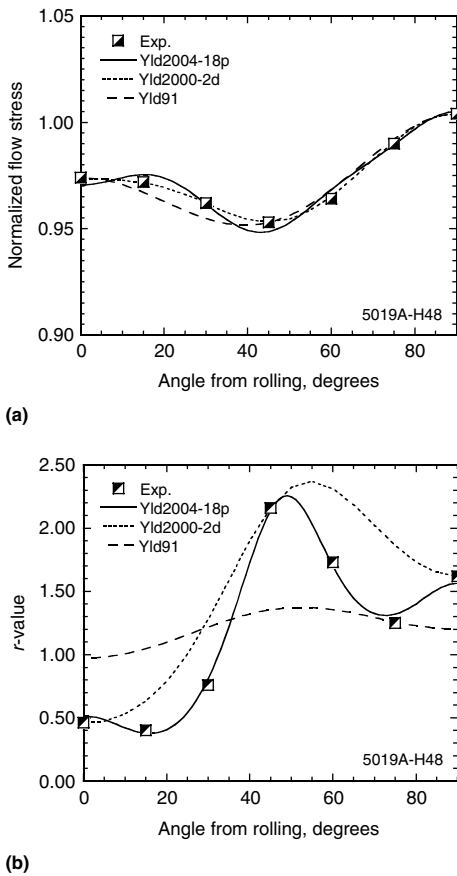


Fig. 7 Experimental results and predictions based on different yield functions of the (a) normalized tensile flow stress, and (b) r -value as a function of the angle between tensile and rolling directions for an aluminum alloy 5019A-H48 sheet sample

imperfection. In this context, damage is defined as the nucleation, growth, and coalescence of microvoids in a material due to plastic deformation. Studies of damage based on microscopic observations and probability calculations have shown that the order of magnitude of D in Eq 28 for typical commercial alloys is 0.4% (Ref 75–77). In the following discussion, the value of $1 - D = 0.996$ has been used to quantitatively characterize the imperfection.

Figure 8 shows an FLC computed for a 2008-T4 alloy sheet sample using two yield surfaces

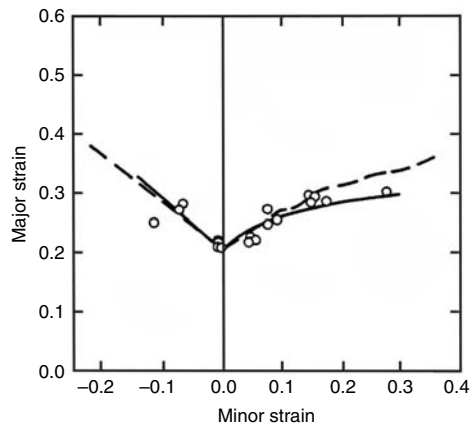


Fig. 8 Experimental forming-limit curve for an aluminum alloy 2008-T4 sheet sample (data points), and calculated curves based on the Yld89 (a special case of Yld2000-2d) yield function (solid line) and a crystal-plasticity model (dashed line). $A = 447$ MPa (65 ksi); $B = 248$ MPa (36 ksi); $C = 4.3$ (Voce coefficients in Eq 8). Assumed initial imperfection size, $t^0/t = 0.996$. Source: Ref 78

(Ref 78). The first yield condition was described with the function Yld89 (Ref 36), a particular case of Yld2000-2d. The second yield condition was based on the Bishop and Hill (Ref 16) crystal-plasticity model. The same Voce-type work-hardening law, Eq 8, was used for both simulations. Both predictions are in good agreement with experimental data. In the stretching range, the imperfection orientation was assumed to be perpendicular to one of the orthotropic axes (rolling or transverse direction). The FLC was the lowest of the two curves calculated for the major strain either in the rolling or in the transverse direction. Experience in such computations shows that, for weakly textured materials, the forming limit is minimal for either case. However, for strongly textured aluminum alloy sheet, this is not necessarily the case. The influence of texture and microstructure on the FLC has been investigated by many authors (Ref 79–87).

Stress-Based Forming-Limit Curves. The previous discussion assumed that deformation occurs along linear strain paths, that is, $\rho = de_2/de_1$ is constant. In practice, particularly for multistep forming, this is not the case. Moreover, it was shown by Kikuma et al. (Ref 88) that nonlinear strain paths have an influence on the FLC. Kobayashi et al. (Ref 89) and Graf and Hosford (Ref 90, 91) showed that the FLC strongly depends on the strain path for steel and aluminum alloy sheets, respectively. The characterization of forming limits in strain space is therefore a practical challenge for complex forming processes due to this sensitivity.

For computational purposes, one of the most promising solutions for dealing with strain path

effects on the FLC is to use a stress-based approach, as proposed by Kleemola and Pelkkikangas (Ref 92), Arrieux et al. (Ref 93), Stoughton (Ref 94), and Stoughton and Yoon (Ref 95). These authors have shown that the FLC in stress space is path-independent and should be suitable to the analysis of any forming problem. As can be seen in Fig. 9, the FLCs described in strain space with different prestrains are mapped to a single curve in stress space. This verifies the path independence of the stress-based FLC. Recently, Kuwabara et al. (Ref 96) measured the stress state near the forming limit of tube deformed using internal pressure and end feed under proportional and nonproportional loading conditions. These authors confirmed that the forming limit as characterized by the state of stress is insensitive to the loading history.

Although not practical in a press shop, the stress-based FLC can be very effective when it is used to assess the safety margins in finite element simulations of forming processes. In order to compute the stress-based FLC, a representation of the forming-limit behavior for proportional loading in strain space, that is, the locus of principal strains, is specified as follows:

FLC (strain-based)

$$\equiv \begin{bmatrix} e_1^{FLC} \\ e_2^{FLC} \end{bmatrix} = e_1^{FLC}(\rho) \begin{bmatrix} 1 \\ \rho \end{bmatrix} \quad (\text{Eq 30})$$

where e_1^{FLC} and e_2^{FLC} are the coordinates of the FLC for linear strain paths, that is, major and minor principal strains. These points can be either measured or calculated, for instance, with the MK model. The strain path $\rho = e_2^{FLC}/e_1^{FLC}$ is consistent with the definition in the previous

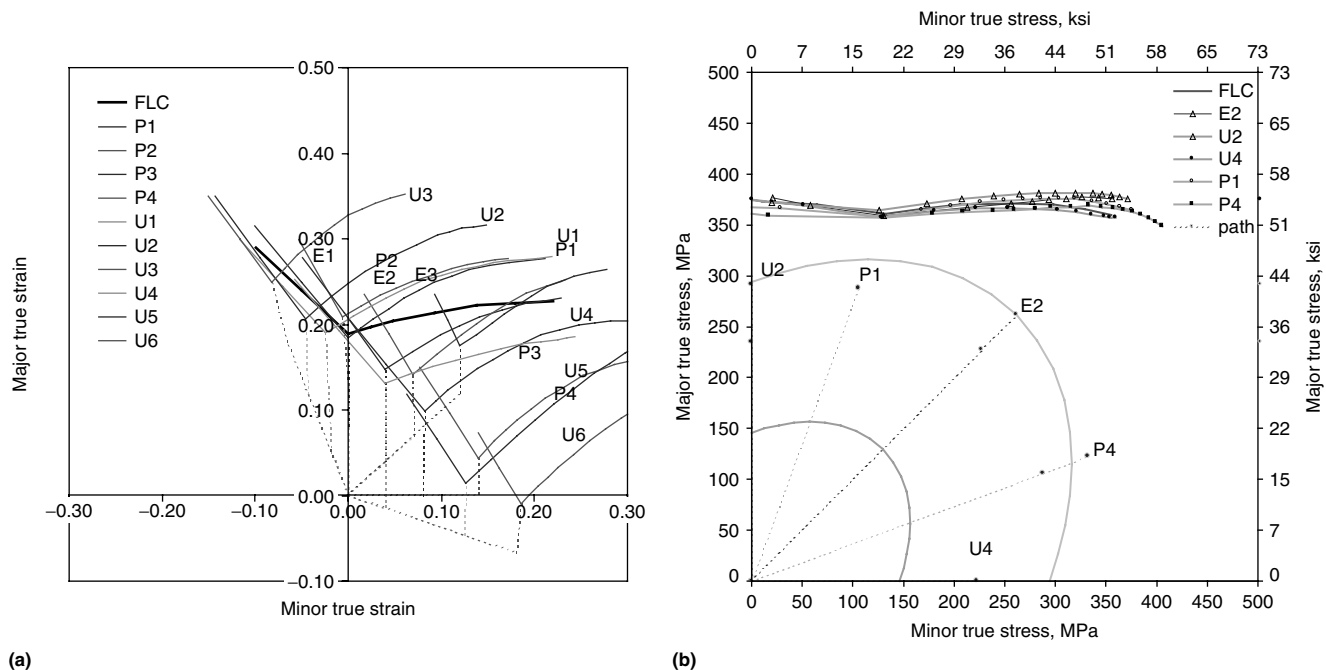


Fig. 9 Effect of strain path on forming-limit curves (FLCs). (a) Strain-based FLC (exhibiting a path effect). (b) Stress-based FLC (limited path effect). Source: Ref 95

section and can vary in the range $\rho = [-1, +1]$. Because Eq 30 is assumed to accurately characterize the strain-based forming limit under proportional loading, it can be used with a plasticity model (yield function and strain hardening) to calculate the path-independent stress-based FLC, which can be similarly represented as:

$$FLC \text{ (stress-based)} = \begin{bmatrix} \sigma_1^{FLC} \\ \sigma_2^{FLC} \end{bmatrix} = \sigma_1^{FLC}(\alpha) \begin{bmatrix} 1 \\ \alpha \end{bmatrix} \quad \text{(Eq 31)}$$

In Eq 31, α is the ratio of the minor to the major principal stresses ($\sigma_2^{FLC}/\sigma_1^{FLC}$) of the stress-based FLC.

Although this FLC is assumed to be path-independent, the stresses calculated in the finite element (FE) analysis are path-dependent variables. Therefore, it is necessary to monitor the stress state at each step of the computation and determine if it is below or above the stress-based FLC. For this purpose, it is convenient to use a single parameter to monitor the formability margin, as follows (Ref 95):

$$\gamma_c = \frac{\bar{\sigma}(\sigma_{ij})}{h(\bar{\epsilon}^{FLC})} \quad \text{(Eq 32)}$$

where:

$$\bar{\epsilon}^{FLC} = \frac{e_1^{FLC}(1 + \rho)}{\frac{\partial \bar{\sigma}}{\partial \sigma_{11}} + \frac{\partial \bar{\sigma}}{\partial \sigma_{22}}} \quad \text{(Eq 33)}$$

In Eq 32, γ_c is a single stress-scaling factor representing the degree of formability according to the criteria:

$$\begin{aligned} \gamma_c < 1 & \text{ safe} \\ \gamma_c > 1 & \text{ necked (failure occurs)} \end{aligned} \quad \text{(Eq 34)}$$

The formability margin as defined previously is based on the assumption that the forming limit is isotropic in the plane of the sheet. This assumption justifies the use of principal stresses and the representation of the forming limit as a curve in a two-dimensional diagram. In general, Graf and Hosford (Ref 90, 91) and others have shown that the forming limit is anisotropic. The method to deal with anisotropic data in stress-based FLC is explained in Ref 95.

Compressive Instability

Wrinkling occurs when a blank is subjected to compressive stresses during the forming process, as, for instance, in the flange of a cup during drawing, triggered by the elastoplastic buckling of the thin structure. Although the failure limit due to plastic flow localization can be simply defined by the FLC at each point of a continuum, the wrinkling limit cannot be defined with simple variables such as strain, stress, and thickness. Buckling is also strongly affected by the mechanical properties of the sheet material, the geometry of the blank, and contact conditions. The analysis of wrinkling initiation and growth is

therefore difficult to perform due to the complex synergistic effects of the controlling parameters. Furthermore, commonly observed in instability phenomena, small variations of the parameters can result in widely different wrinkling behaviors. In the face of these difficulties, the study of wrinkling has generally been conducted case by case. A unique wrinkling criterion, which could be used effectively for various sheet-forming processes, has not been proposed yet.

Most of the studies related to wrinkling were carried out experimentally or analytically before the numerical simulation of stamping processes (Ref 97–99). An analytical bifurcation can give a useful estimate of the elastoplastic buckling of a plate with a basic geometrical shape and subjected to simple boundary conditions. This analysis, however, cannot be employed in general sheet metal forming processes. With the rapid development of computing power, wrinkling has also been studied using the FE method. Wrinkling can be analyzed in the same way as most buckling problems, that is, assuming a nonlinear elastic material behavior and ignoring complex contact conditions. Because wrinkling occurs in the plastic region, for a more realistic approach, the computations need to be based on an elastoplastic material model and take into account the complex contact conditions inherently present in sheet-forming processes.

Two types of buckling analyses are performed with the FE method: a bifurcation analysis of a structure without imperfection (Ref 100–103) and a nonbifurcation analysis, which assumes an initial imperfection or disturbing force due to load eccentricities (Ref 104–108). Because the FE analyses of sheet metal forming processes involve strong nonlinearities in geometry, material, and contact, convergence problems are frequently observed. Nonbifurcation analyses sometimes lead to reasonable results, because all real structures have inherent imperfections, such as material nonuniformity or geometric unevenness. Thus, most wrinkling analyses have been carried out using a nonbifurcation analysis. However, the results obtained from a nonbifurcation analysis are sensitive to the amplitude of the initial imperfection, which is chosen arbitrarily. As a result, bifurcation algorithms have been implemented into the FE method in order to analyze more rigorously the wrinkling behavior of sheet metal during forming (Ref 102, 103).

A number of studies have been devoted to the plastic buckling problem as a bifurcation phenomenon. The buckling of a column or a compressed circular plate and the wrinkling of a deep-drawn cup are typical examples of bifurcation problems. Shanley (Ref 109) first showed that the buckling load of a centrally compressed short column coincides theoretically with the tangent modulus. Hill (Ref 110) later generalized Shanley's concept and established a uniqueness criterion for the mathematical solution of elastic-plastic solids. This theory is now widely accepted in the analysis of bifurcation problems. Hutchinson (Ref 111)

specialized Hill's bifurcation criterion (Ref 110) to a class of loadings characterized by a single parameter and studied the postbifurcation behavior associated with the lowest possible bifurcation load. He showed that the initial slope of the load-deflection curve governs the material behavior in only a very small neighborhood of the bifurcation point, and that the rates of change of the instantaneous moduli at bifurcation have a major effect on the postbifurcation behavior. Prebuckling and postbuckling analyses were carried out with an FE method by incorporating the arc-length control scheme (Ref 100). In the bifurcation problem (Fig. 10), the stiffness matrix of the linearized FE equation becomes singular at a bifurcation point, and the Newton-Raphson solver cannot proceed further. Riks (Ref 100) proposed the continuation method by which the postbifurcation analysis can be carried out along the secondary solution branch (path) and implemented it for the buckling of elastic shell structures. In the work of Kim et al. (Ref 103), the continuation method was introduced in order to analyze the initiation and growth of wrinkles in deep drawing processes. A brief summary of the Riks method applied to sheet metal forming simulations is summarized as follows.

For a conservative system, the change of the total potential energy, $\Delta\Pi$, due to an admissible variation $\delta\mathbf{u}$ of the displacement field \mathbf{u} can be written as:

$$\Delta\Pi(\mathbf{u}, \delta\mathbf{u}) = \frac{\partial\Pi}{\partial u_i} \delta u_i + \frac{1}{2} \frac{\partial^2\Pi}{\partial u_i \partial u_j} \delta u_i \delta u_j + \dots \quad \text{(Eq 35)}$$

The second variation term must be positive definite for a stable system, a condition that can be written as:

$$\frac{\partial^2\Pi}{\partial u_i \partial u_j} \delta u_i \delta u_j = K_{ij} \delta u_i \delta u_j > 0 \quad \text{(Eq 36)}$$

where K_{ij} represents the component of the tangent stiffness matrix \mathbf{K} . Therefore, the stability limit is reached when matrix \mathbf{K} ceases to be

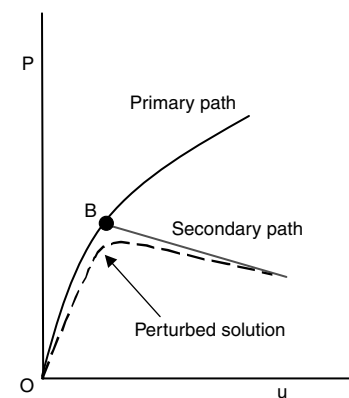


Fig. 10 Schematic illustration of solution paths in load-displacement (P-u) space for bifurcation-type problems

positive definite, that is, when:

$$\det[\mathbf{K}] = 0 \quad (\text{Eq 37})$$

In sheet metal forming process simulations, it is difficult to find the exact bifurcation point, because the control parameters in most of the problems are based on displacements. As a consequence, the determinant in Eq 37 changes sign abruptly within one incremental step in implicit analyses. The bifurcation point is, therefore, found by checking each value of the diagonal terms of a triangular form of the stiffness matrix.

The FE solution past the bifurcation point should not be the primary branch (path) but the secondary or bifurcated branch (path). In most of the bifurcation problems, the eigenvector is orthogonal to the primary branch. Thus, the increment of the nodal displacement field along the secondary branch $\Delta \mathbf{u}^s$ can be simply taken as (Ref 100–103, 112, 113):

$$\Delta \mathbf{u}^s = \chi \mathbf{v} \quad (\text{Eq 38})$$

In Eq 38, χ is a positive scalar, which should be determined, and \mathbf{v} is an eigenvector at a singular point, that is, calculated from the matrix identity:

$$\mathbf{K} \mathbf{v} = \mathbf{0} \quad (\text{Eq 39})$$

In Eq 38, the trial increment $\Delta \mathbf{u}^s = \mathbf{v}$ is used as an initial estimate for the Newton-type solution scheme, and it is updated during the iterations. The effect of magnitude of χ on the wrinkling behavior is, therefore, eliminated. The details of this method are discussed in Ref 102 and 103.

Springback

Springback refers to the undesirable shape change due to the release of the tools after a sheet-forming operation. Previous studies indicated that the final part shape after springback depends on the amount of elastic energy stored in the part during forming (Ref 114–119). Unfortunately, the elastic energy stored is a function of the process parameters, geometry of the tools and the blank, friction conditions, and material behavior. Moreover, the prediction of springback is very sensitive to the numerical parameters used in the simulations (Ref 120, 121). Therefore, predicting and compensating springback are very complicated tasks. The analytical and FE approaches for the prediction of springback were very well summarized in Ref 122 (see also the article “Springback” in this Volume).

The elastic modulus and yield strength are the first-order material parameters that influence springback. This can be perceived intuitively by considering a stress-strain curve. The amount of recoverable stored energy, $\Delta E_r \cong \sigma \epsilon = \sigma^2/E$, decreases when the Young's modulus increases (0 for a rigid-plastic material) and the yield strengths decreases. Aluminum alloys have similar yield strengths but lower

elastic moduli than mild steels and consequently tend to generate more springback. However, other material parameters have an effect as well. Geng and Wagoner (Ref 123) discussed the importance of plastic anisotropy and the role of the yield surface. Time-dependent springback was investigated by Wagoner et al. (Ref 124) for a 6022-T4 aluminum alloy sheet sample. This effect was incorporated in finite element (FE) model using constitutive equations involving creep deformation (Ref 125).

During springback, when the tools are removed from a formed part, the material unloads elastically and, depending on the geometry, some elements can experience re-loading in the reverse direction even beyond the yield limit. This plastic deformation can, in turn, influence the amount of springback. Due to the Bauschinger effect discussed previously, that is, the yield stress for reverse loading is lower than the flow stress just before unloading, the springback can be altered. Therefore, it is often necessary to account for the Bauschinger effect in springback simulations. The isotropic hardening is no longer valid, and an effective way to model this effect is to assume that the yield surface translates in stress space. This assumption, called kinematic hardening, was introduced by Prager (Ref 126), and some modifications were proposed by Ziegler (Ref 127). In order to describe the expansion and translation of the yield surface during plastic deformation, the combination of isotropic and kinematic hardening is also commonly used (Ref 128). Other approaches based on two or multiple embedded yield surfaces (Ref 129–131) account for the Bauschinger effect as well. Because the model proposed by Chaboche built on a single yield surface, its use in FE simulations is more cost-effective compared to the more sophisticated multisurface models. In addition to the Bauschinger effect, a transient hardening behavior is also observed during reverse loading, and some of the aforementioned models can account for this phenomenon. In particular, the Bauschinger effect as well as its associated transient behavior, which result from dislocation pattern reorganization, were effectively and elegantly modeled by Teodosiu and Hu (Ref 20).

A formulation for kinematic hardening that can accommodate any yield function is well summarized in Ref 132 to 134. Assuming a homogenous yield function ϕ of degree a , translated in stress space by the backstress $\boldsymbol{\alpha}$, a tensorial state variable, the yield condition can be expressed as:

$$\phi(\sigma_{ij} - \alpha_{ij}) - \bar{\sigma}_{iso}^a = 0 \quad (\text{Eq 40})$$

where σ_{ij} are the components of the Cauchy stress tensor, and $\bar{\sigma}_{iso}$ is the stress measuring the size of the yield surface. The rate of plastic work, \dot{w} , dissipated during deformation becomes:

$$\dot{w} = \sigma_{ij} \dot{\epsilon}_{ij} = (\sigma_{ij} - \alpha_{ij}) \dot{\epsilon}_{ij} + \alpha_{ij} \dot{\epsilon}_{ij} \quad (\text{Eq 41})$$

where $\dot{\epsilon}_{ij}$ are the components of the strain rate (or rate of deformation) tensor. The effective quantities are now defined considering the following modified plastic work-equivalence relationship:

$$\dot{w}_{iso} = (\sigma_{ij} - \alpha_{ij}) \dot{\epsilon}_{ij} = \bar{\sigma}_{iso} \dot{\bar{\epsilon}} \quad (\text{Eq 42})$$

where $\dot{\bar{\epsilon}}$ is the effective plastic strain rate. As for isotropic hardening, the normality rule is assumed to hold, and the model is complete with the definition of an evolution equation for the backstress.

Finite Element Modeling

Nonlinear FE methods are becoming very popular in sheet metal forming process simulations. A problem is nonlinear if the force-displacement relationship depends on the current state, that is, on current displacement, force, and stress-strain relationship:

$$\mathbf{P} = \mathbf{K}(\mathbf{P}, \mathbf{u}) \mathbf{u} \quad (\text{Eq 43})$$

where \mathbf{u} is a displacement vector, \mathbf{P} a force vector, and \mathbf{K} the stiffness matrix. Linear problems form a subset of nonlinear problems. For example, in classical linear elastostatics, this relationship can be written in the form:

$$\mathbf{P} = \mathbf{K} \mathbf{u} \quad (\text{Eq 44})$$

where the stiffness matrix \mathbf{K} is independent of both \mathbf{u} and \mathbf{P} . If the matrix \mathbf{K} depends on other state variables, such as temperature, radiation, etc., but does not depend on displacement or loads, the problem is still linear. Similarly, if the mass matrix is constant, the following dynamic problem is also linear:

$$\mathbf{P} = \mathbf{M} \ddot{\mathbf{u}} + \mathbf{K} \mathbf{u} \quad (\text{Eq 45})$$

There are three sources of nonlinearities: material, geometry, and boundary condition. The material nonlinearity results from the nonlinear relationship between stresses and strains due to material plasticity. Geometric nonlinearity results from the nonlinear relationship between strains and displacements or the nonlinear relationship between stresses and forces. If the stress measure is energetically conjugate to the strain measure, both sources of nonlinearity have the same form. This type of nonlinearity is mathematically well defined but often difficult to treat numerically. Boundary conditions such as contact or friction are also sources of nonlinearities. This type of nonlinearity manifests itself in several real-life situations, for instance, in metal forming, gears, interfaces of mechanical components, pneumatic tire, and crash. A load on a structure causes nonlinearity if it changes with the displacement and deformation of the structure (such as pressure loading). Sheet metal forming processes include all of these three types of nonlinearities, in particular, elastoplastic material behavior,

large rotations, and contacts between the tools and the blank.

General Kinematics

The kinematics of deformation can be described by Lagrangian, Eulerian, and Arbitrary Lagrangian-Eulerian (ALE) formulations. In the Lagrangian method, the FE mesh is attached to the material and moves through space along with the material. In the Eulerian formulation, the FE mesh is fixed in space, and the material flows through the mesh. In the ALE formulation, the grid moves independently from the material, yet in a way that spans the material at any time. The Lagrangian approach can be further classified in two categories: the total and the updated Lagrangian methods. In the total Lagrangian approach, equilibrium is expressed with the original undeformed reference frame, while, in the updated Lagrangian approach, the current configuration acts as the reference frame. In the latter, the true or Cauchy stresses and an energetically conjugate strain measure, namely, the true strain, are used in the constitutive relationships. The updated Lagrange approach is useful in:

- Analyses of shell and beam structure in which rotations are large so that the nonlinear terms in the curvature expressions may no longer be neglected
- Large strain-plasticity analyses in which the plastic deformations cannot be assumed to be infinitesimal

In general, this approach can be used to analyze structure where inelastic behavior causes large deformations. The (initial) Lagrangian coordinate frame has little physical significance in these analyses, because inelastic deformations are, by definition, permanent. Therefore, the updated Lagrangian formulation is appropriate for the simulations of sheet metal forming processes. For these analyses, the Lagrangian frame of reference is redefined at the last completed iteration of the current increment. The variational form of the equation for the static problem in the updated Lagrangian approach is given as:

$$\int_V \frac{\partial \delta u_i}{\partial x_j} \sigma_{ij} dV - \int_{\Gamma} \delta u_i f_i d\Gamma = 0 \tag{Eq 46}$$

where V is the volume considered, Γ is the surface on which the traction components f_i are imposed, and σ_{ij} is the Cauchy stress. The linearized variational form of Eq 46 needed for the Newton-Raphson numerical solver can be written as:

$$\begin{aligned} & \int_V \frac{\partial \delta u_i}{\partial x_j} C_{ijkl} \frac{\partial \Delta u_k}{\partial x_l} dV + \int_V \frac{\partial \delta u_i}{\partial x_j} \sigma_{jl} \frac{\partial \Delta u_i}{\partial x_l} dV \\ & = - \int_V \frac{\partial \delta u_i}{\partial x_j} \sigma_{ij} dV + \int_{\Gamma} \delta u_i f_i d\Gamma \end{aligned} \tag{Eq 47}$$

The left side of Eq 47 corresponds to the material and geometric stiffness, while its right side is associated with the internal and external force vectors, respectively. In the FE method, the left side dominates the convergence rate, and the right side directly controls the accuracy of the solution.

Element Formulation

Finite element analyses of sheet metal forming processes can be broadly classified into three categories according to the element types used: membrane analysis (plane stress without bending stiffness), shell analysis (plane stress with bending stiffness), and continuum analysis (general stress state). For sheet metal forming simulations, the shell analysis is the most popular.

Wang and Budiansky (Ref 135) suggested an elastic-plastic membrane formulation based on the plane-stress assumption for forming sheet metal exhibiting normal anisotropy (also called planar isotropy). This type of anisotropy characterize a sheet with identical properties in any direction in its plane but different properties in its normal direction. These authors provided an example on the axisymmetric stretching of a sheet with a hemispherical punch. Yang and Kim (Ref 136) derived a membrane-based rigid plastic FE method incorporating material and geometric nonlinearities for materials exhibiting planar anisotropy, which was described by Hill’s 1948 yield criterion. Hora et al. (Ref 137) analyzed the forming of an arbitrary-shaped auto-body panel, which is a drawing-dominant process, based on membrane elements. Yoo et al. (Ref 138) suggested the bending energy augmented membrane approach in order to overcome the inherent numerical buckling occurring due to the lack of rotational stiffness in the membrane analysis. Kubli and Reissner (Ref 139) analyzed complicated panels, considering bending effects using the uncoupled solutions of membrane and bending analyses. However, the membrane analysis provides insufficient information for the treatment of bending-dominant forming processes.

Two basic approaches concerning the development of nonlinear shell FEs can be identified: classical shell elements and degenerated solid elements. The classical shell elements are directly based on the governing differential equations of an appropriate shell theory. Despite the potential economy of such elements, the development of nonlinear shell elements involves mathematical complexities. The degenerated solid element, which was initiated by Ahmad et al. (Ref 140) for the linear analysis of continuum formulation, is reduced in dimensionality by direct imposition of kinematics and constitutive constraints. The works of Ramm (Ref 141), Parish (Ref 142), Hughes and Liu (Ref 143, 144), Dvorkin and Bathe (Ref 145), and Liu et al. (Ref 146), among many others, constitute representative examples of this methodology carried out in the most general way for the nonlinear regime. The books of Bathe

(Ref 147), Hughes (Ref 148), and the thesis of Stanley (Ref 149) offer a comprehensive overview of the degenerated solid approach and related methodologies. A point frequently made for the degenerated approach is that it avoids the mathematical complexities associated with the classical shell theory and hence is much easier for numerical implementation. Similarly, Belytschko et al. (Ref 150), Hallquist et al. (Ref 151), and Belytschko and Leviathan (Ref 152) developed one-point quadrature shell elements for the explicit FE methods applicable to both linear and nonlinear plate and shell analyses.

Finite element analyses using shell elements have shown a remarkable progress in the last few years with respect to both accuracy and efficiency. Recently, Cardoso and Yoon (Ref 153, 154) suggested new one-point quadrature elements considering element warping and thickness strain. In addition, Batoz et al. (Ref 155) suggested a membrane-bending FE model with membrane effects represented by constant-strain triangular elements and the bending effect represented by discrete Kirchhoff triangular elements. Alves de Sousa et al. (Ref 156) recently proposed one-point quadrature solid-shell elements that have eight nodes and consider multiple integration points through the thickness within one element layer, which can be applied for springback analysis. The application of shell elements to sheet-forming simulations can be found in Ref 154 and 157 to 161. The kinematics for a continuum-based shell is summarized as follows.

Kinematic Hypotheses. The physical spatial region of the shell element is described with coordinates (ξ, η, ζ) , as shown in Fig. 11. The current position vector \mathbf{x} of a generic point of the shell is defined by:

$$\mathbf{x}(\xi, \eta, \zeta) = \bar{\mathbf{x}}(\xi, \eta) + \zeta \tilde{\mathbf{x}}(\xi, \eta) \tag{Eq 48}$$

where $\tilde{\mathbf{x}}(\xi, \eta, \zeta) = \zeta \mathbf{t}(\xi, \eta) / 2$.

In Eq 48, the reference surface $\bar{\mathbf{x}}(\xi, \eta)$ is chosen to be the midsurface, that is $\bar{\mathbf{x}}(\xi, \eta) = \mathbf{x}(\xi, \eta, \zeta = 0)$. The symbol $\tilde{\mathbf{x}}$ is the unit fiber vector emanating from the midsurface, and t is the shell thickness. Equation 48 is often referred to as straight normal assumption. Equation 48 prescribes a linear ζ -dependence, which constrains the unit fiber vector to remain straight but not necessarily normal to the reference surface. Equation 48 can be interpolated from the node positions to any point of a shell element through the shape functions:

$$\mathbf{x}(\xi, \eta, \zeta) = \sum_{p=1}^{N_{en}} N_p(\xi, \eta) \{ \bar{\mathbf{x}}_p + \zeta \tilde{\mathbf{x}}_p \} \tag{Eq 49}$$

where:

$$\tilde{\mathbf{x}}(\xi, \eta, \zeta) = \zeta \sum_{p=1}^{N_{en}} N_p(\xi, \eta) \mathbf{t}_p$$

In the previous equation, the subscript “p” ranges over the number of nodes per element N_{en} . The shape functions, N_p , are typically selected

from the Lagrange interpolation family. The displacement, \mathbf{u} , of a generic point is the difference between its current position, \mathbf{x} , and its reference position, \mathbf{X} :

$$\mathbf{u}(\xi, \eta, \bar{z}) = \mathbf{x}(\xi, \eta, \bar{z}) - \mathbf{X}(\xi, \eta, \bar{Z}) \quad (\text{Eq 50})$$

or

$$\mathbf{u}(\xi, \eta, \bar{z}) = \bar{\mathbf{u}}(\xi, \eta) + \bar{z}\bar{\mathbf{u}}(\xi, \eta) + (\bar{z} - \bar{Z})\bar{\mathbf{X}} \quad (\text{Eq 51})$$

where $\mathbf{X}(\xi, \eta, \bar{Z}) = \bar{\mathbf{X}}(\xi, \eta) + \bar{Z}\bar{\mathbf{X}}(\xi, \eta)$.

The displacement vector, \mathbf{u} , can be obtained by assuming that the fiber vector is inextensible. This assumption allows fiber vectors to rotate, but they cannot be stretched or contracted. Therefore, $\bar{\mathbf{x}}$ remains a unit vector and the quantity $\bar{z} - \bar{Z}$ in Eq 51 vanishes. By applying the straight normal kinematics $\bar{z} - \bar{Z} = 0$ in Eq 51, the position of a continuum point is defined as:

$$\mathbf{u}(\xi, \eta, \bar{z}) = \bar{\mathbf{u}}(\xi, \eta) + \bar{z}\bar{\mathbf{u}}(\xi, \eta) \quad (\text{Eq 52})$$

or

$$\Delta\mathbf{u}(\xi, \eta, \bar{z}) = \Delta\bar{\mathbf{u}}(\xi, \eta) + \bar{z}\Delta\bar{\mathbf{u}}(\xi, \eta) \quad (\text{Eq 53})$$

with $\Delta\mathbf{u} \cdot \bar{\mathbf{x}} = 0$.

Equation 52 is referred to as the incremental rigid normal assumption. In addition, the kinematics of the shell element is defined in terms of the same shape functions introduced previously in Eq 49:

$$\mathbf{u}(\xi, \eta, \bar{z}) = \sum_{p=1}^{N_{en}} N_p(\xi, \eta) \{\bar{\mathbf{u}}_p + \bar{z}\bar{\mathbf{u}}_p\} \quad (\text{Eq 54})$$

where the six global incremental nodal variables at the p^{th} node are:

$$\Delta\mathbf{a}_p = [\Delta\bar{\mathbf{u}}_{1p} \ \Delta\bar{\mathbf{u}}_{2p} \ \Delta\bar{\mathbf{u}}_{3p} \ \Delta\bar{\mathbf{u}}_{1p} \ \Delta\bar{\mathbf{u}}_{2p} \ \Delta\bar{\mathbf{u}}_{3p}]^T \quad (\text{Eq 55})$$

Static Hypotheses. In addition to the kinematics, the static hypotheses are used to exploit the relative insignificance of the stress component acting directly on the reference surface. The first static hypothesis, zero normal stress, simply consists of eliminating this component whenever it explicitly appears in the governing equations:

$$\sigma_{33} = 0 \quad (\text{zero normal stress}) \quad (\text{Eq 56})$$

The second hypothesis is, in some sense, the time derivative of the zero normal stress because, if a quantity is identically zero, its derivative expressed in an appropriate frame should vanish as well:

$$\dot{\sigma}_{33} = 0 \quad (\text{zero normal stress rate}) \quad (\text{Eq 57})$$

For details, the reader is referred to Ref 161.

Matrix Formulation

The assembled FE matrix of the linearized variational form in Eq 47 is obtained by replacing the incremental and variational displacements ($\Delta\mathbf{u}$ and $\delta\mathbf{u}$) by their discrete element approximation and by incorporating the kinematic and static hypotheses, Eq 53 and 57. Then, the resulting equation is integrated element-wise over the entire problem domain. Using the arbitrariness of the weighting coefficients, the system of equations for the nodal displacement increments are:

$$(\mathbf{K}^{\text{matl}} + \mathbf{K}^{\text{geom}})\Delta\mathbf{a} = \mathbf{F}^{\text{ext}} - \mathbf{F}^{\text{int}} \quad (\text{Eq 58})$$

In Eq 58, \mathbf{F}^{ext} is the assembled external force vector, \mathbf{F}^{int} is the assembled internal force vector, and \mathbf{K}^{matl} and \mathbf{K}^{geom} are the assembled material and geometric stiffness matrices, respectively. Detailed information about Eq 58 is given in Ref 147 and 148.

Equation 58 forms a system of equations for the so-called implicit method. By ignoring the left side, that is, $\mathbf{F}^{\text{ext}} - \mathbf{F}^{\text{int}} = 0$, Eq 58 becomes an equation for the so-called explicit method. Numerical solution schemes are often referred to as being explicit or implicit. When a direct computation of the dependent variables can be made in terms of known quantities, the computation is said to be explicit. In contrast, when the dependent variables are defined by a coupled set of equations, an iterative technique is needed to obtain the solution, such as for Eq 58, and the numerical method is said to be implicit. As mentioned in the section "General Kinematics" in this article, the right side of Eq 58 controls the solution accuracy, and the left side dominates the convergence rate. Because the explicit method does not involve the left side, stiffness matrix assembling and convergence checking are not required. Therefore, it is very attractive when

convergence is a big hurdle, as it may be for complicated sheet metal stamping problems. However, the explicit solution is only stable if the time step size is smaller than a critical value:

$$\Delta t \leq \Delta t^{\text{crit}} = \frac{2}{\omega_{\text{max}}} \quad (\text{Eq 59})$$

which guarantees the accuracy of the solution. Here, ω_{max} is the largest natural frequency of the system (characteristics of the mesh size and material density). Usually, the explicit stable time step size is extremely small compared to the implicit solution (approximately 1000 smaller). Furthermore, the mesh size is proportional to $1/\omega_{\text{max}}$. Therefore, the stable time step size becomes smaller when the mesh size decreases. In particular, when mesh refinement is conducted during the analysis, mesh sizes become approximately one quarter smaller per one time of mesh refinement. Because the stable time step size in an explicit code is determined by the minimum element length, it causes the analysis time to be much longer. In contrast, the implicit solution is always stable; that is, the time step can be arbitrarily large for a linear problem. For nonlinear problems, the implicit time step size may need to become smaller according to convergence difficulties.

Elastic-Plastic Stress Integration

Most rate-independent plastic models are formulated in terms of rate-type constitutive equations, for which the integration method has a considerable influence on the efficiency, accuracy, and convergence of the solution. In the simulation of sheet forming processes, the constitutive equation is integrated along an assumed deformation path. Among the infinite ways to assume the deformation path, the minimum plastic work path in homogeneous deformation has been found to have several advantages. Requirements for achieving minimum plastic work paths in homogeneous deformation are well documented in Ref 162 to 165. The minimum work path, which is also the proportional logarithmic (true) strain paths, is achieved under two conditions. First, the set of three principal axes of stretching is fixed with respect to the material; second, the logarithms of the principal stretches remain in a fixed ratio. The incremental deformation theory based on the minimum plastic work path enables convenient decoupling of deformation and rotation by the polar decomposition at each process increment. The resulting incremental constitutive law is frame-indifferent (objective), because the theory uses a materially embedded coordinate system. The incremental deformation theory is useful for the FE modeling of rigid-plastic and elastoplastic constitutive formulations. In rigid plasticity, the theory was introduced for process analyses by Yang and Kim (Ref 136), Germain et al. (Ref 166), Chung and Richmond (Ref 167, 168), and Yoon et al.

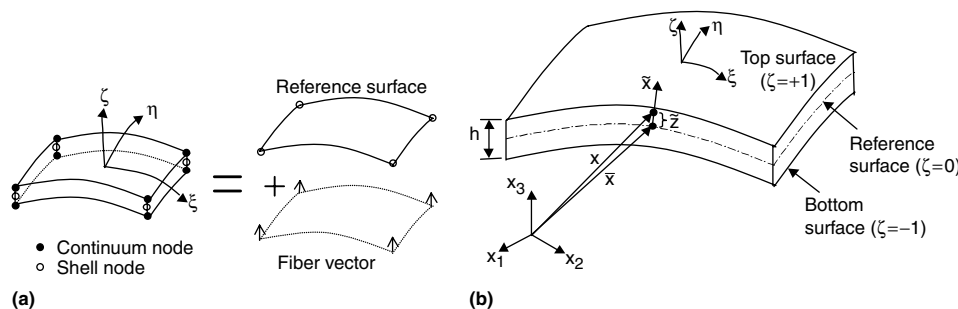


Fig. 11 Continuum-based shell elements. (a) Construction of a typical shell element. (b) Shell geometry

(Ref 169). For elastoplastic materials, the incremental deformation theory has been successfully applied for materials exhibiting isotropy (Ref 170) and planar anisotropy (Ref 161, 171).

Continuum Models. The most popular scheme for stress integration is the predictor-corrector method (often called return mapping). This method is applied in two successive steps: the prediction step, during which a trial stress state is estimated, and the corrector step, during which a flow rule is applied by return mapping procedures in order to bring (project) the stress onto the yield surface or, in other words, to ensure the consistency condition (i.e., the stress state must be on the yield surface). During the return mapping procedure, a reasonable assumption for the deformation path must be imposed. A return mapping procedure was first introduced in the paper of Wilkins (Ref 172). The works of Ortiz and Pinsky (Ref 173) and Ortiz et al. (Ref 174) apply the closet point-projection method to perform the procedure in plane-stress conditions. Later, Ortiz and Simo (Ref 175) developed a new class of integration algorithms based on the cutting-plane approach. However, this approach has no clear physical meaning in the deformation path viewpoint. Recently, Yoon et al. (Ref 161) proposed the multistage return mapping method based on incremental deformation theory, which follows the minimum plastic work path. In this work, it was proven that, when the consistency condition and normality rule (strain increment normal to yield surface) are imposed, this new projection during the current unknown step becomes the closet point projection. The stress integration procedure is briefly summarized as follows.

The increment of the Cauchy stresses is given by applying the fourth-order elastic modulus tensor C^e to the incremental second-order elastic strain tensor $\Delta\epsilon - \Delta\epsilon^p$:

$$\Delta\sigma = C^e(\Delta\epsilon - \Delta\epsilon^p) \tag{Eq 60}$$

in which $\Delta\epsilon$ and $\Delta\epsilon^p$ are the total and plastic strain increments, respectively. The relationship in Eq 60 is assumed to be expressed in a material-embedded coordinate system. Therefore, it is objective with respect to (independent of) the material rotation. In order to follow the minimum plastic work path in the incremental deformation theory, the logarithmic plastic strain needs to remain normal to the yield surface at the representative stress state, that is:

$$\Delta\epsilon^p = \Delta\bar{\epsilon}^p \frac{\partial \bar{\sigma}}{\partial \sigma} = \gamma \mathbf{m} \tag{Eq 61}$$

where $\mathbf{m} = \partial \bar{\sigma} / \partial \sigma$ is a symbolic notation that represents the tensor of component $m_{ij} = \partial \bar{\sigma} / \partial \sigma_{ij}$. The condition stipulating that the updated stress stays on the strain-hardening curve provides the following equation:

$$\begin{aligned} F(\lambda) &= \bar{\sigma}(\sigma_n + \Delta\sigma) - h(\bar{\epsilon}_n^p + \lambda) \\ &= \bar{\sigma}[\sigma_n + C^e(\Delta\epsilon - \lambda \mathbf{m})] - h(\bar{\epsilon}_n^p + \lambda) = 0 \end{aligned} \tag{Eq 62}$$

where the subscript “n” denote quantities at step “n” in the simulation.

The predictor-corrector scheme based on the Newton-Raphson method is generally used to solve the nonlinear system in Eq 62 for $\lambda = \Delta\bar{\epsilon}^p$. However, while a mathematical solution to this equation does exist, it can be difficult to obtain numerically if the strain increment is not small enough. In the examples in the next section, a multistage return mapping procedure based on the control of the residual suggested by Yoon et al. (Ref 161) was employed. The proposed method is applicable to nonquadratic yield functions and general strain-hardening laws without a line search algorithm, even for a relatively large strain increment (10%). At the end of the step, when Eq 62 is solved, all kinematic variables and stresses are updated.

In order to consider the rotation of the anisotropic axes, a co-rotational coordinate system (constructed at each integration point), is

defined and initially coincides with the material symmetry axes. For the examples discussed in the section “Application Examples” in this article, it is assumed that the orthogonality of the anisotropy axes is preserved during sheet forming under the isotropic hardening assumption. This assumption is generally considered as appropriate in sheet-forming process simulations. From the polar decomposition theorem, the deformation of a material element represented by the deformation gradient tensor, \mathbf{F} , is the combination of a pure rotation, \mathbf{R} , and a pure stretch, \mathbf{U} ($\mathbf{F} = \mathbf{R}\mathbf{U}$). The rotation of the anisotropy axes is updated incrementally at every step by the rotation amount (\mathbf{R}) obtained from the polar decomposition (Fig. 12). For instance, if at the first step ${}^0\lambda$ and ${}^0\mu$ are the unit vectors coinciding with the rolling and transverse directions, respectively, the updated axes are given by:

$$\begin{aligned} \lambda &= \mathbf{R} {}^0\lambda \\ \mu &= \mathbf{R} {}^0\mu \end{aligned} \tag{Eq 63}$$

Crystal-Plasticity Models. These models account for the deformation of a material by crystallographic slip and for the reorientation of the crystal lattice. The influence of crystal symmetry on elastic constants can be included, and the strain-hardening and cross-hardening effects between the slip systems can be incorporated through the use of state variables. Furthermore, a rate-dependent approach is also typically employed to relate the shear stresses and shear strains on the different slip systems. The kinematics of the model was summarized by Dao and Asaro (Ref 176). The deformation gradient, \mathbf{F} , is decomposed into a plastic deformation, \mathbf{F}^p , which is the summation of the shear strain for each slip system, and a combination of elastic deformation and rigid body motion of the crystal lattice, \mathbf{F}^e , as shown in Fig. 13, that is:

$$\mathbf{F} = \mathbf{F}^e \mathbf{F}^p \tag{Eq 64}$$

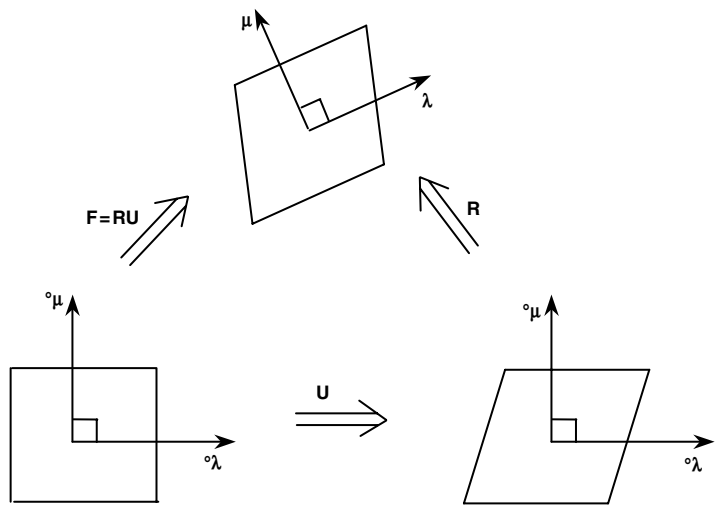


Fig. 12 Rotation of anisotropic axes during deformation. \mathbf{F} , deformation gradient tensor; \mathbf{R} , pure rotation; \mathbf{U} , pure stretch; ${}^0\mu$, unit vector for transverse direction; ${}^0\lambda$, unit vector for rolling direction

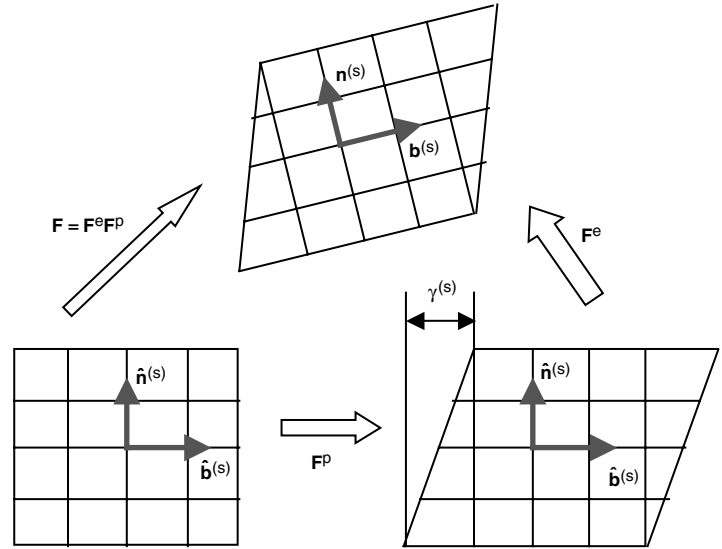


Fig. 13 Multiplicative decomposition of deformation gradient. See text for description.

Because plasticity occurs by dislocation slip, the plastic deformation rate, \mathbf{L}^p , is determined by the summation of the shear strain contribution over all of the slip system (Ref 176):

$$\mathbf{L}^p = \sum_{(s)} \dot{\gamma}^{(s)} \mathbf{b}^{(s)} \mathbf{n}^{(s)} \quad (\text{Eq 65})$$

Here, (s) denotes a slip system, $\mathbf{n}^{(s)}$ is the normal of the slip plane, and $\mathbf{b}^{(s)}$ is the vector in the slip direction. Both vectors are orthogonal, that is, $\mathbf{n}^{(s)} \times \mathbf{b}^{(s)} = \mathbf{0}$, and are assumed to rotate with the elastic spin of the lattice. In general, these vectors are not unit vectors like in a phenomenological model because they are allowed to stretch. Using Eq 65, the symmetric and skew symmetric parts of \mathbf{L}^p the rate of deformation tensor \mathbf{D}^p and plastic spin \mathbf{W}^p , respectively, can be written as:

$$\begin{aligned} \mathbf{D}^p &= 1/2(\mathbf{L}^p + \mathbf{L}^{pT}) = \sum_{(s)} \dot{\gamma}^{(s)} 1/2(\mathbf{b}^{(s)} \mathbf{n}^{(s)} + \mathbf{n}^{(s)} \mathbf{b}^{(s)}) \\ \text{or } \mathbf{D}^p &= \sum_{(s)} \dot{\gamma}^{(s)} \mathbf{P}_{(s)} \quad (\text{Eq 66}) \end{aligned}$$

$$\begin{aligned} \mathbf{W}^p &= 1/2(\mathbf{L}^p - \mathbf{L}^{pT}) = \sum_{(s)} \dot{\gamma}^{(s)} 1/2(\mathbf{b}^{(s)} \mathbf{n}^{(s)} - \mathbf{n}^{(s)} \mathbf{b}^{(s)}) \\ \text{or } \mathbf{W}^p &= \sum_{(s)} \dot{\gamma}^{(s)} \mathbf{W}_{(s)} \quad (\text{Eq 67}) \end{aligned}$$

where the tensors $\mathbf{P}_{(s)}$ and $\mathbf{W}_{(s)}$ have been introduced for notational convenience.

Usually, the Cauchy or true stress, $\boldsymbol{\sigma}$, is employed for the stress integration. However, in this section, the Kirchhoff stress, $\boldsymbol{\tau}$, is considered. By ignoring the elastic volume change, the Cauchy stress is related to the Kirchhoff stress, $\boldsymbol{\tau}$, through the relationship $\boldsymbol{\tau} = J\boldsymbol{\sigma}$, where J is the determinant of \mathbf{F}^e . Writing the rate of deformation tensor as the sum of elastic and plastic parts, an objective stress rate, $\check{\boldsymbol{\tau}}$, can be expressed as:

$$\begin{aligned} \check{\boldsymbol{\tau}} &= \mathbf{K} : \mathbf{D} - \sum_{(s)} \dot{\gamma}^{(s)} (\mathbf{K} : \mathbf{P}_{(s)} + \mathbf{W}_{(s)} \cdot \boldsymbol{\tau} - \boldsymbol{\tau} \cdot \mathbf{W}_{(s)}) \\ &= \mathbf{K} : \mathbf{D} - \sum_{(s)} \dot{\gamma}^{(s)} \mathbf{R}_{(s)} \quad (\text{Eq 68}) \end{aligned}$$

where \mathbf{K} is the fourth-order elastic modulus tensor, and \mathbf{D} is the rate of deformation tensor. Then, the resolved shear stress at the end of the time step becomes:

$$\begin{aligned} \tau_{t+\Delta t}^{(s)} &= \tau_t^{(s)} + \Delta t \check{\tau}^{(s)} = \tau_t^{(s)} + \Delta t \mathbf{R}_{(s)} : \mathbf{D} - \Delta t \\ &\quad \times \sum_{(a)} \dot{\gamma}^{(a)} \mathbf{R}_{(s)} : \mathbf{P}_{(a)} \quad (\text{Eq 69}) \end{aligned}$$

where $\mathbf{R}_{(s)} = \mathbf{K} : \mathbf{R}_{(s)} + \mathbf{W}_{(s)} \times \boldsymbol{\tau} - \boldsymbol{\tau} \times \mathbf{W}_{(s)}$.

The resolved shear stress, $\tau^{(s)}$, also follows the rate-dependent hardening rule:

$$\tau^{(s)} = g^o \left(\frac{|\dot{\gamma}^{(s)}|}{\dot{\gamma}_o} \right)^m \text{sign} \left(\dot{\gamma}^{(s)} \right) \quad (\text{Eq 70})$$

where g^o is the shear yield stress on a slip system.

Finally, the resolved shear stress defined by Eq 69 and 70 must have the same value at $t + \Delta t$:

$$\begin{aligned} E^s(\dot{\gamma}^{(s)}) &= \tau_t^{(s)} + \Delta t \mathbf{R}_{(s)} : \mathbf{D} - \Delta t \\ &\quad \times \sum_{(a)} \dot{\gamma}^{(a)} \mathbf{R}_{(s)} \times \mathbf{P}_{(a)} - g^o \left(\frac{|\dot{\gamma}^{(s)}|}{\dot{\gamma}_o} \right)^m \text{sign} \left(\dot{\gamma}^{(s)} \right) = 0 \quad (\text{Eq 71}) \end{aligned}$$

Equation 71 is a nonlinear equation. It is solved with the Newton-Raphson method after linearization (Ref 177), that is:

$$E^s(\dot{\gamma}^{(s)}) + \sum_{(a)} \frac{dE^s}{d\dot{\gamma}^{(a)}} d\dot{\gamma}^{(a)} = 0 \quad (\text{Eq 72})$$

Ideal Forming Design Theory

Finite element (FE) methods are used mostly for analysis of boundary-value problems. This means that the problem is well set, with known tool and blank geometries, material and interface properties, and realistic stress- and displacement-imposed boundary conditions. This type of application of the method is referred to as FE analysis. However, in practice, the final shape of the product is imposed, and the manufacturing process needs to be designed around it. Therefore, in order to improve the conventional trial-and-error-based practices for optimizing forming processes, either by experiments or FE analysis, an FE design theory, called ideal forming theory, was proposed (Ref 167, 168, 178). The FE implementation is a time-efficient one-step code, providing not only the initial blank geometry but all the intermediate shapes and the entire load history necessary to achieve it, thus providing invaluable information about the ideal process parameters. This application is referred to as FE design.

In this theory, materials are prescribed to deform following the minimum plastic work path. The final product shape is specified, and the initial blank shape is obtained from the global extremum plastic work criterion as a one-step backward solution. Although the theory is general enough to accommodate any other form of constraints, the underlying physical assumption of this extremum work condition is that the strain gradients are minimized on the overall part, thus departing as much as possible from plastic flow localization modes. In order to consider local thinning effects due to friction, a method based on a modified extremum work criterion has also been developed (Ref 178). The ideal forming theory has been successfully applied for sheet-forming processes to optimize flat blanks (Ref 179–181) and also for bulk forming in steady (Ref 182–185) and nonsteady flows (Ref 186, 187).

When a sheet (or tube) is discretized with meshes and the surface tractions are approximated by point forces, the total plastic work, W ,

becomes a function of the initial and final configurations, assuming that the minimum plastic work path is imposed on each material element, that is:

$$W = W[\bar{\boldsymbol{\varepsilon}}(\mathbf{x}^i, \mathbf{X}^i)] = \iiint \bar{\sigma}(\bar{\boldsymbol{\varepsilon}}) \bar{\boldsymbol{\varepsilon}} dV_0 \quad (\text{Eq 73})$$

where $\bar{\sigma}(\bar{\boldsymbol{\varepsilon}})$, $\bar{\boldsymbol{\varepsilon}} = \int d\bar{\boldsymbol{\varepsilon}}$, and V_0 are the effective stress, the effective strain, and the initial volume of the part, respectively. The parameters \mathbf{x}^i and \mathbf{X}^i are the final and initial positions of the i th node in the global Cartesian coordinate system. As mentioned previously, in this method, the part shape (\mathbf{x}^i) is prescribed, and the initial blank shape (\mathbf{X}^i) is the output of the numerical simulation. Therefore, the optimization is performed with respect to the initial configuration. In the ideal forming theory, when the minimum plastic work path is imposed for each material element, the initial blank shape is obtained by optimizing the plastic work or, more specifically, by imposing $dW/d\mathbf{X}^i = 0$. Another term is added to this equation when friction is taken into account. In this optimization, constraints pertaining to the initial shape are also imposed. For instance, the initial blank must be on a given surface, for instance, a flat sheet, a cylindrical tube, and so on. In tube hydroforming, the preform shape must be straight with a uniform cross section if the tube is extruded. Therefore, the additional constraint is that each node-set in Fig. 14 must move the same amount in the \bar{X}_3 direction. Because of the mathematical form of Eq 73, it is much more convenient to describe the material with a strain-rate potential (see the section “Strain-Rate Potentials” in this article), which emphasizes the importance of this type of material description, particularly applied to aluminum alloy products. The combination of plastic work optimization, material behavior, friction conditions, and initial shape constraints reduces to a system of nonlinear equations that can be solved for \mathbf{X}^i (corresponding to the initial blank shape), using a Newton-Raphson solver.

Of course, this theory is based on ideal deformation conditions. More realistic simulations can be achieved with FE analysis codes, but the ideal forming theory provides a quick and excellent initial mapping of the forming process needed to manufacture a product, thus limiting the number of costly experimental and FE analysis trials.

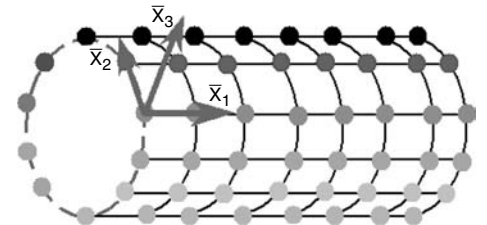


Fig. 14 Local Cartesian coordinate systems defined on an assumed cross section of the initial tube

Application Examples

Example 1: Shear Testing Simulation. This first example pertains to the simulation of the simple shear test. This example illustrates the numerical testing and possible issues, such as implementation, input data, and so on, that should be addressed before performing the simulation of a complex forming operation. Simple examples also validate the choice of the constitutive models used in the simulations. In this particular example, the simple shear test shows that the constitutive response of material subjected to a given deformation mode (e.g., shear) can be well approximated using constitutive equations identified using information measured on different stress states (e.g., uniaxial tension or balanced biaxial tension).

Simple shear tests were conducted on a commercial-purity 1050-O and automotive 6022-T4 aluminum alloy sheet samples on a device similar to that shown in Fig. 4. The testing was performed in two specimen orientations, that is, with shear in the transverse direction (TD) or at 45° from the rolling direction (RD). The

1050-O sheet sample was 3 mm (0.12 in.) thick, and the shear specimen was 40 by 40 mm (1.6 by 1.6 in.), with a shear zone width of 8 mm (0.3 in.) (Fig. 15). The 6022-T4 sheet sample was 1 mm (0.04 in.) thick, and the shear specimen was 60 by 15 mm (2.4 by 0.6 in.), with a shear zone width of 3 mm (0.12 in.) (Fig. 15). More details concerning these tests are reported in Ref 177, 188, and 189.

For 1050-O, the experimental shear stress/shear strain curves along the two shear directions showed that the material exhibits anisotropic strain hardening (Fig. 16). The strain hardening in the initial stage of plastic deformation is higher for simple shear in the TD (90°) but saturates prematurely compared to simple shear at 45° from the RD. For 6022-T4, this effect is also observed but much less pronounced. In previous work (Ref 23, 188, 189), two microstructural parameters were invoked to explain this phenomenon: dislocation cell structure and crystallographic texture. The pole figures were measured using standard x-ray diffraction techniques. The resulting (111) pole figures (Fig. 17) indicated that both as-received materi-

als exhibited a preponderant {100}<001> cube texture, although stronger in the 1050-O sheet sample than in the 6022-T4. As expected, the 1050-O sample developed a well-defined dislocation microstructure during deformation, principally dislocation walls on the (111) planes oriented near the planes of maximum shear stress. The 6022-T4 alloy also displayed a dislocation structure with similar features, but the walls were much fainter and the overall dislocation distribution was more uniform (Fig. 18).

Simulations. Two constitutive models, phenomenological and polycrystal, were implemented into the user material subroutines provided in FE commercial codes (Yld2004-18p yield function into MSC.Marc HYPELA2, MSC. Software Corp., and polycrystal model into ABAQUS UMAT, ABAQUS Inc.) and used for the simple shear test simulations. The meshes and boundary conditions for the shear tests are represented in Fig. 19. The left grip was fixed, while the right grip was allowed to move along the vertical direction only. The FE meshes were generated only for the shear deformation zone of the specimens (not the grip area), using 320 and 800 uniform elements for 1050-O and 6022-T4, respectively, with a single layer through the thickness direction (Fig. 19).

The input data and resulting Yld2004-18p coefficients (see the section “Anisotropic Yield Functions” in this article) for the 1050-O and 6022-T4 sheet samples are given in Tables 1 and 2, respectively. For the FE simulations performed with Yld2004-18p, isotropic hardening was assumed with the stress-strain relationships:

- 1050-O: $\bar{\sigma} = K(\bar{\epsilon} + \bar{\epsilon}_0)^n$, $K = 132 \text{ MPa}$ (19 ksi), $\bar{\epsilon}_0 = 0.0005$, and $n = 0.285$
- 6022-T4: $\bar{\sigma} = A - B \exp(-C\bar{\epsilon})$, $A = 396 \text{ MPa}$ (57 ksi), $B = 234 \text{ MPa}$ (34 ksi), $C = 6.745$

as measured with the RD uniaxial tension and bulge tests, respectively.

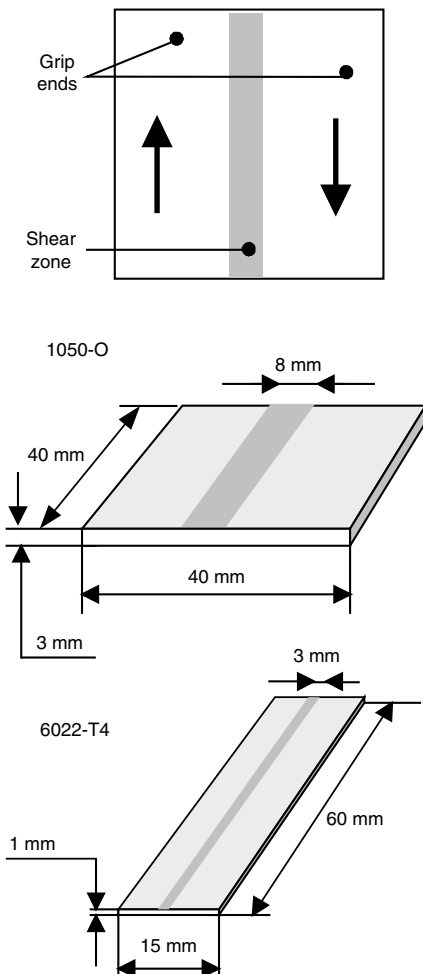


Fig. 15 Shear test-specimen geometry. Source: Ref 177

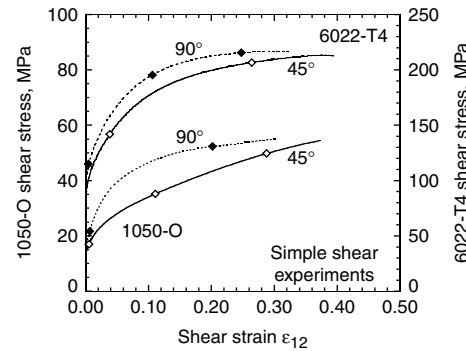


Fig. 16 Simple shear stress-strain curves measured along different directions with respect to the rolling direction for aluminum alloy 1050-O and 6022-T4 sheet samples. Source: Ref 177

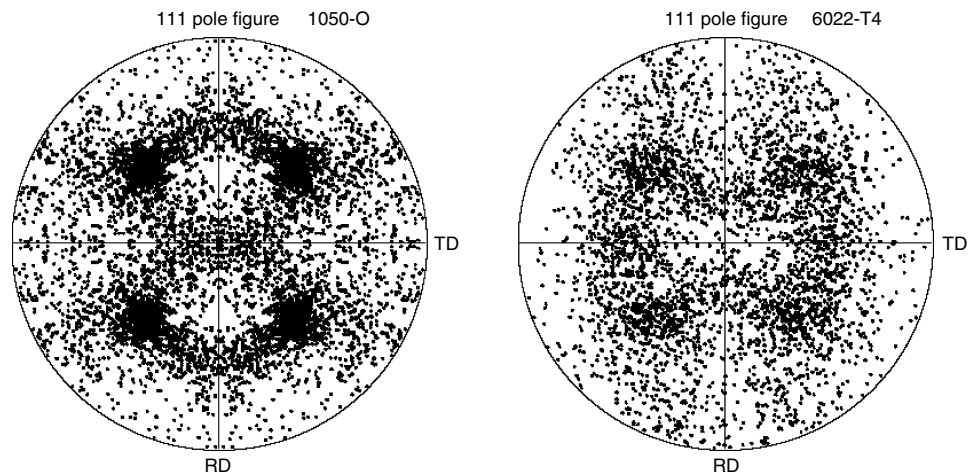


Fig. 17 111 pole figures for aluminum alloy 1050-O and 6022-T4 sheet samples. RD, rolling direction; TD, transverse direction. Source: Ref 177

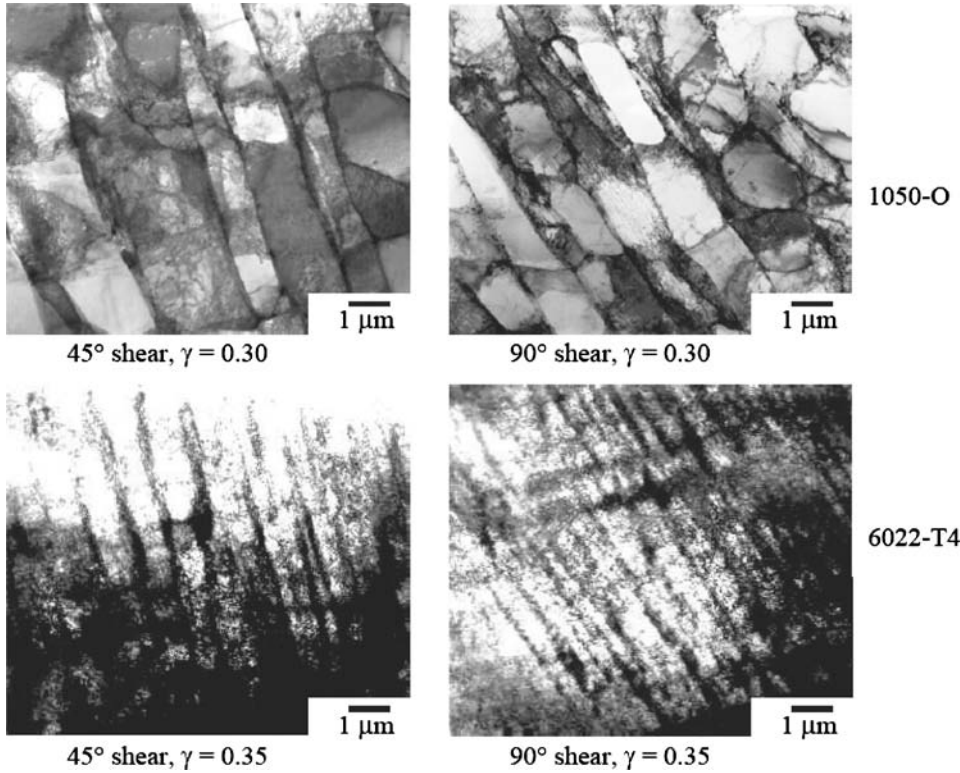


Fig. 18 Dislocation substructure developed during simple shear of aluminum alloy 1050-O and 6022-T4 sheet samples (for different amounts of shear strain: $\epsilon_{12} = 0.5 \times \gamma$). Source: Ref 177

Figure 20 represents the effective stress contours for the shear specimens deformed up to a shear strain of $\gamma/2 = 0.25$ for the 1050-O and 6022-T4 sheet samples. It was observed that the experimental and predicted shapes of the specimen ends were very similar. Moreover, the FE simulations indicated that, for the strain range investigated, the deformation in the shear specimens was quite uniform, that is, end effects were minimal. The shear stress/shear strain curves along the two shear directions (at 45° from RD and in the TD) for the 1050-O and 6022-T4 sheet samples as predicted with Yld2004-18p are given in Fig. 21. The results were found to be in good agreement with the experimental trends (Fig. 16). For 1050-O, although the material was assumed to exhibit isotropic hardening, the simulations were able to reproduce a certain amount of anisotropic hardening observed experimentally during simple shear. For 6022-T4, although the difference in hardening between the two test orientations was noticeable and consistent with the experiments, this effect was small. The influence of the element size was evaluated by performing simulations with only one element (1 by 1 by 0.1, unit: millimeters) for both materials. It was shown that the element size had only a negligible effect on the results (Fig. 21). Therefore, the simulations using crystal plasticity were performed with only one element.

For simulations using a rate-dependent crystal-plasticity model (see the section “Crystal-Plasticity Models” in this article), a

Table 2 Yld2004-18p coefficients for 1050-O and 6022-T4 (exponent $a=8$)

	1050-O			6022-T4			
c'_{12}	1.019520	c''_{12}	0.830052	c'_{12}	0.755194	c''_{12}	1.120720
c'_{13}	1.094320	c''_{13}	0.850783	c'_{13}	0.799378	c''_{13}	1.056340
c'_{21}	1.270160	c''_{21}	0.537084	c'_{21}	0.773630	c''_{21}	1.146560
c'_{23}	1.127570	c''_{23}	0.753355	c'_{23}	0.865580	c''_{23}	1.132990
c'_{31}	0.794215	c''_{31}	1.119190	c'_{31}	1.047560	c''_{31}	0.763656
c'_{32}	0.829394	c''_{32}	1.009200	c'_{32}	1.088160	c''_{32}	0.954688
c'_{44}	7.713050	c''_{44}	7.717600	c'_{44}	1.016290	c''_{44}	1.009770
c'_{55}	1.004780	c''_{55}	1.009920	c'_{55}	0.993625	c''_{55}	0.994796
c'_{66}	1.282290	c''_{66}	0.302787	c'_{66}	0.624258	c''_{66}	1.208880

trial-and-error method was employed to find the hardening parameters that provided a good approximation of the uniaxial hardening curves (and biaxial curve for 6022-T4). The strain-rate sensitivity coefficient for 1050-O was set to 0.01, which corresponds to the experimental value. For 6022-T4, the strain-rate sensitivity coefficient was arbitrarily set to 0.001, because the experimental value for this type of material is usually close to zero or slightly negative. The textures corresponding to the (111) pole figures (Fig. 17), which include approximately 1000 grain orientations each, were used as input. The simple shear-hardening curves predicted with crystal plasticity are shown in Fig. 22 for both sheet samples. Again, the trends predicted with this model were in very good agreement with the experiments (Fig. 16). The relative shapes of the stress-strain curves predicted with crystal plasticity were similar to those predicted with the phenomenological model, but the strain-hardening difference was larger.

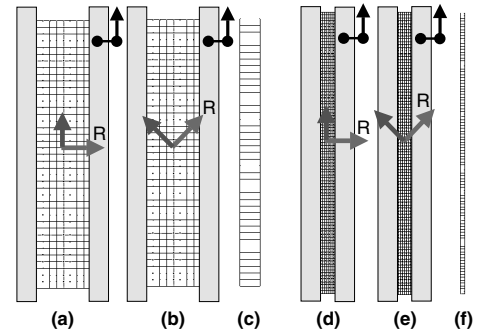


Fig. 19 Initial meshes with boundary conditions and material orientations for the simulations of simple shear. Left grip is fixed, and right grip moves in the vertical direction only. (a) 1050-O, 90° shear. (b) 1050-O, 45° shear. (c) 1050-O, side view of mesh. (d) 6022-T4, 90° shear. (e) 6022-T4, 45° shear. (f) 6022-T4, side view of mesh. R denotes the rolling direction. Source: Ref 177

Table 1 Mechanical anisotropy data for 1050-O and 6022-T4

Alloy	$\sigma_0/\bar{\sigma}$	$\sigma_{45}/\bar{\sigma}$	$\sigma_{90}/\bar{\sigma}$	$\sigma_y/\bar{\sigma}$	r_0	r_{45}	r_{90}
1050-O	1.000	1.000	1.000	0.999	0.61	0.21	0.87
6022-T4	1.045	1.003	0.975	1.000	0.73	0.43	0.51

In summary, the simple shear stress-strain curves of 1050-O and 6022-T4 aluminum alloy sheet samples were predicted using FE analyses with two constitutive material descriptions. Although the constitutive coefficients were identified using uniaxial tension and bulge test stress-strain curves, the simple shear-hardening responses were in good agreement with the experiments. It was shown that, even for a material exhibiting an isotropic strain-hardening behavior, the simple shear behavior could display an apparent anisotropic strain-hardening behavior due to the combined effect of plastic anisotropy and realistic boundary conditions. Crystal plasticity, led to a real anisotropic-hardening effect resulting from crystallographic texture evolution. Both effects, apparent and real, could fully explain the behavior of 1050-O and 6022-T4 sheet samples in simple shear. It was also concluded that the apparent anisotropic hardening was due to texture but not to dislocation microstructure. More details can be found in Ref 177.

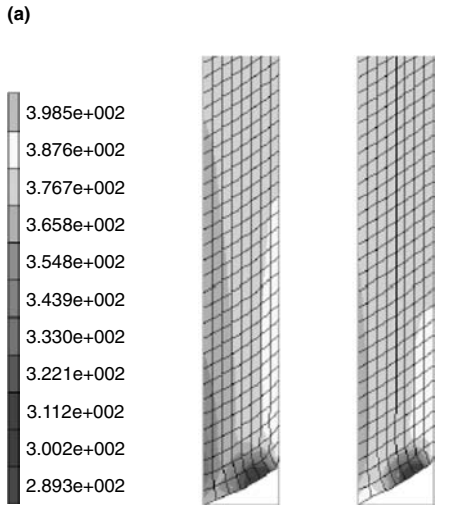
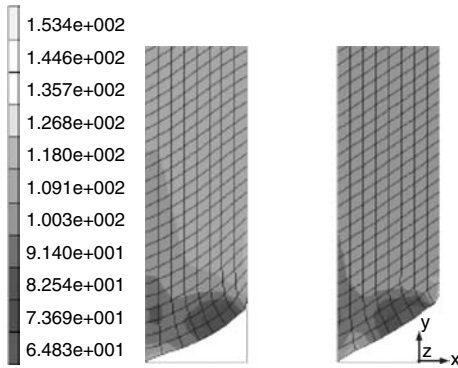


Fig. 20 Predicted effective stress superimposed on the deformed mesh for simple shear specimens of aluminum alloy sheet samples: (a) 1050-O and (b) 6022-T4. Source: Ref 177

Example 2: Finite Element Analysis of Cup Drawing.

Cup drawing is not only a material test but also a forming operation, which accounts for the combined effects of blankholder force, friction, and sheet bending/unbending. Drawing of a circular blank with a circular punch is one of the best benchmarks to evaluate planar anisotropy. After this operation, the wall-height profile around the periphery of the resulting cup is usually not constant but exhibits peaks (also called ears) and valleys. The objective of this example is to show how FE analysis can be used to describe cup drawing for a 2090-T3 alloy sheet, which exhibits more than four ears. The Yld2004-18p yield function (see section “Material Modeling” in this article, and Ref 42) was used for the description of the plastic behavior of the aluminum alloy sheet. The FE cup-height profile was computed and compared with the results of a simple but more time-efficient analytical model as well as with experimental results.

Using the isotropic-hardening assumption, there have been previous efforts to simulate anisotropic phenomena such as the formation of ears in drawing circular blanks for aluminum alloy sheets. For this purpose, Chung and Shah (Ref 190) and Yoon et al. (Ref 169), respectively,

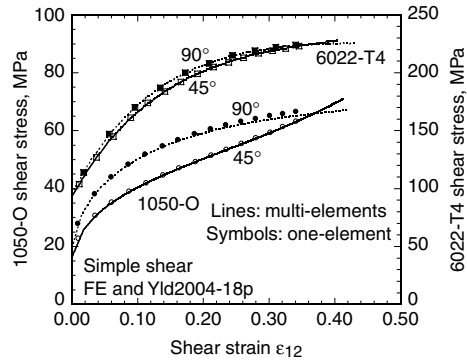


Fig. 21 Finite-element predictions of shear stress-strain curves for 1050-O and 6022-T4 sheet samples from one-element or multiple-element simulations using Yld2004-18p

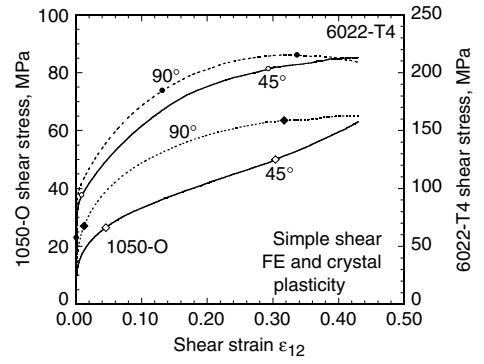


Fig. 22 Finite-element predictions of simple shear stress-strain curves for 1050-O and 6022-T4 sheet samples using a crystal-plasticity model (one-element simulations). Source: Ref 177

Table 3 Normalized yield stress input data to determine Yld2004-18p coefficients for aluminum alloy 2090-T3 sheet sample, $\bar{\sigma}/\sigma_0$

In-plane	σ_0/σ_0	σ_{15}/σ_0	σ_{30}/σ_0	σ_{45}/σ_0	σ_{60}/σ_0	σ_{75}/σ_0	σ_{90}/σ_0	σ_b/σ_0
Experimental results	1.0000	0.9605	0.9102	0.8114	0.8096	0.8815	0.9102	1.0350
Out-of-plane	$\sigma_{45}^{TD-ND}/\sigma_0$		$\sigma_{45}^{ND-RD}/\sigma_0$		τ^{TD-ND}/σ_0		τ^{ND-RD}/σ_0	
Crystal-plasticity results	0.92		0.89		0.48		0.47	

Table 4 *r*-value input data to determine Yld2004-18p coefficients for aluminum alloy 2090-T3 sheet sample

In-plane	r_0	r_{15}	r_{30}	r_{45}	r_{60}	r_{75}	r_{90}	r_b
Experimental results	0.2115	0.3269	0.6923	1.5769	1.0385	0.5384	0.6923	0.67

applied the stress and the strain-rate potentials proposed by Barlat et al. (Ref 37, 51) for a 2008-T4 aluminum alloy sheet. Andersson et al. (Ref 191) employed the criterion by Karafillis and Boyce (Ref 38) for the limiting dome height test. Yoon et al. (Ref 192) used Yld96, the yield function suggested by Barlat et al. (Ref 193) for circular deep drawing of a 2090-T3 aluminum alloy sheet. Yoon et al. (Ref 44, 194) simulated a reverse cup-drawing test using Yld2000-2d (see the section “Anisotropic Yield Functions” in this article, and Ref 41). Recently, Yoon et al. (Ref 195) successfully predicted six and eight ears in a circular cup drawing using Yld2004-18p (Ref 42).

Finite-Element-Based Earing Profile. The input data used to determine the anisotropy coefficients of the 2090-T3 aluminum alloy sheet sample are given in Tables 3 and 4. Polycrystal calculations were used to determine the out-of-plane properties given in Table 3. The out-of-plane data consisted of uniaxial tension yield stresses obtained at 45° between the symmetry axes in the planes (RD, normal direction, or ND; RD) and (TD, ND), where ND is the normal direction of the sheet, and the simple shear yield stresses in these planes. Therefore, the 18 coefficients for the yield function were optimized using 20 input data. The Yld2004-18p coefficients (see the section “Anisotropic Yield Functions” in this article) are given in Table 5. It is worth noting that, if a crystal-plasticity model were not available or if a plane-stress shell model

was employed for Yld2004-18p, the assumption $\alpha_7 = \alpha_8 = \alpha_{16} = \alpha_{17} = 1$ could be employed for the out-of-plane anisotropy coefficients. The stress-strain curve used for the simulation was given by the relationship $\bar{\sigma} = 646(0.025 + \bar{\epsilon})^{0.227}$ (MPa). Figure 23 shows the yield surfaces of the 2090-T3 sheet sample predicted using Yld2004-18p. Figure 24 depicts the normalized yield stress and *r*-value anisotropies, calculated with Yld2004-18p and determined experimentally. In Fig. 24, the results of another yield function, denoted Yld96 (Ref 193), are included for comparison purposes. Yld2004-18p accounts for uniaxial properties measured every 15° in the plane of the sheet, whereas the other yield function accounts for tensile properties in only three directions. These figures show that Yld2004-18p accurately captures yield stress and *r*-value directionalities very well.

A sketch of the cup-drawing process that was simulated is shown in Fig. 25. The specific dimensions of the tooling and the process variables used in the simulations for the 2090-T3 sheet sample are as follows:

Punch diameter:	$D_p = 2R_p = 97.46$ mm (3.84 in.)
Punch profile radius:	$r_p = 12.70$ mm (0.50 in.)
Die opening diameter:	$D_d = 2R_d = 101.48$ mm (4.00 in.)
Die-profile radius:	$r_d = 12.70$ mm (0.50 in.)
Blank radius:	$D_b = 2R_b = 158.76$ mm (6.26 in.)
Initial sheet thickness:	1.6 mm (0.06 in.)
Coulomb coefficient of friction:	0.1
Blankholding force:	22.2 kN (2.5 tonf)

The blankholding force was selected to provide a pressure of approximately 1% of the yield stress in order to prevent wrinkling. The friction coefficient was chosen as a typical value for a well-lubricated interface between the sheet and the blankholder. Only a quarter section of the cup with the associated symmetry boundary conditions was analyzed in light of the orthotropic material symmetry. A total of 340 solid elements and 747 nodes with one layer of elements through the sheet thickness were used for the simulation. A user-material subroutine combined with MSC.Marc was employed, based on an implicit time-integration scheme. The Newton-Raphson residual norm of 0.0001 was chosen in the FE simulations for the

convergence criterion. Approximately 2 h were required to complete the FE cup-drawing analysis using an HP 730 computer (Hewlett-Packard Co.).

Figure 26 shows the deformed configurations of the completely drawn cups. The results obtained with Yld96 are included for comparison purposes. It can be seen that Yld96 predicts four ears, while Yld2004-18p predicts six. In Fig. 27, measured and predicted cup-height profiles (also called earing profiles) are compared for the 2090-T3 sheet sample. For an orthotropic material, the cup-height profile between 0 and 90° should be a mirror image of the cup-height profile between 90 and 180° with respect to the 90° axis. However, the measured earing profile slightly deviates from this condition. This deviation may have occurred because the center of the blank was not aligned properly with the centers of the die and the punch during the drawing experiment. Generally, this plot shows that the earing profile obtained from the present theory is in very good agree-

ment with the measured 2profile. In particular, the small ears around 0° (or 360°) and 180° are well predicted.

In summary, this example indicates that an appropriate phenomenological yield function can be used in the FE simulation of the drawing process to predict an earing profile in good agreement with the experimental profile, even for a cup exhibiting more than four ears. In order to obtain this type of accuracy, the anisotropy of the tensile properties must be described very accurately. In the present case, *r*-values and flow stresses were determined with tensile tests conducted every 15° in the plane of the sheet and were very well captured with the yield function Yld2004-18p.

Analytical Earing Profile. Sometimes, for a quick assessment, it is advantageous to use a simple analytic equation to predict the earing profile. For this purpose, the blank of a cup is viewed as a ring (Fig. 28), the inner edge of which is drawn into the inside cavity under uniform displacement boundary control. When the ring starts to draw in, different levels of compressive strains are generated circumferentially due to planar anisotropy. The corresponding radial strains, contributing to the cup-height profile (earing profile), result from the incompressibility condition under a plane-stress state.

From Fig. 28, it is clear that the behavior of the ring in the rolling direction is controlled by the property of the material in compression in the transverse direction. Generalizing, the behavior of the ring in the direction defined by θ is controlled by the property of the material in compression in the direction defined by $\theta + 90^\circ$. Assuming that, for a given direction, uniaxial tension and compression lead to identical properties, the *r*-value directionality can provide a reasonable approximation of the strains at the rim of the ring (Ref 180).

Table 5 Yield function coefficients for aluminum alloy 2090-T3 (exponent $a=8$)

c_{12}^7	-0.0699	c_{12}^{11}	0.9812
c_{13}^7	0.9364	c_{13}^{11}	0.4767
c_{21}^7	0.0791	c_{21}^{11}	0.5753
c_{23}^7	1.0031	c_{23}^{11}	0.8668
c_{31}^7	0.5247	c_{31}^{11}	1.1450
c_{32}^7	1.3632	c_{32}^{11}	-0.0793
c_{44}^7	1.0238	c_{44}^{11}	1.0517
c_{55}^7	1.0691	c_{55}^{11}	1.1471
c_{66}^7	0.9543	c_{66}^{11}	1.4046

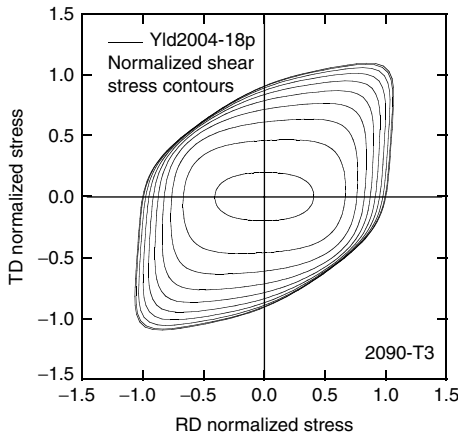


Fig. 23 Yield surface shape for an aluminum alloy 2090-T3 sheet sample. TD, transverse direction; RD, rolling direction. Source: Ref 195

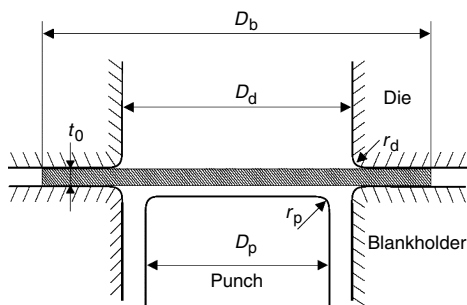


Fig. 25 Schematic illustration of the cup-drawing process. See text for description.

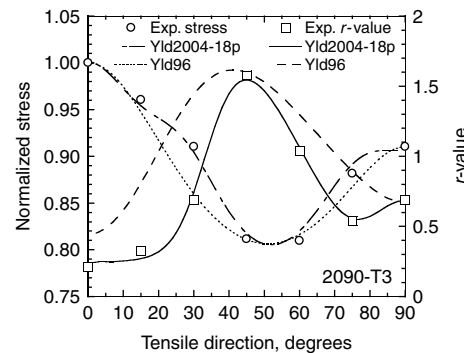


Fig. 24 Measured and calculated variations of the normalized yield stress and *r*-value as a function of the angle between rolling and tensile direction for aluminum alloy 2090-T3. Source: Ref 195

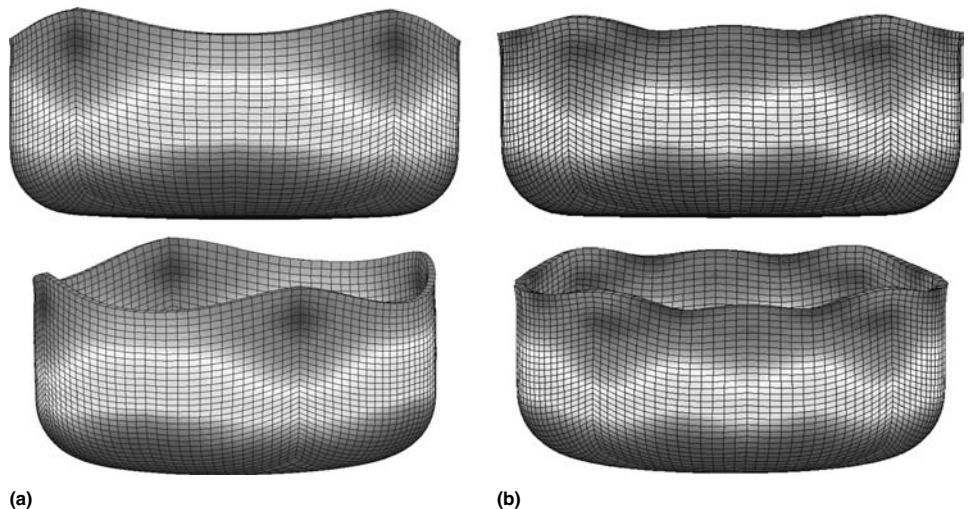


Fig. 26 Finite element predictions of the completely drawn cups for aluminum alloy 2090-T3 using (a) Yld96 and (b) Yld2004-18p yield functions

For the completely drawn cup (Fig. 29), it is assumed that no deformation of the sheet occurs at the flat punch head. Hence, the wall deformation can be mapped with the deformation of the flange, leading to an expression for the total cup height as a function of the parameter θ (Ref 194):

$$H_0 = r_p + (R_b - R_c) + \frac{r_{0+90}}{(r_{0+90} + 1)} \times \left((R_c - R_b) + R_b \ln \left(\frac{R_b}{R_c} \right) \right) \quad (\text{Eq 74})$$

where R_c is given by $R_c = (R_p + R_d)/2$. The parameter θ describes the angle (in degrees) between the position of the rim considered and the rolling direction. Equation 74 was derived based on a midplane geometry by neglecting the sheet thickness. Using this equation, it is possible to calculate the approximate cup height from the initial blank size, cup geometry and r -value directionality.

The analytical prediction H_0 (Fig. 27) leads to six ears, in agreement with the FE simulation results obtained with Yld2004-18p and the experimental data. It is also worth mentioning that the resulting cup-height profiles exhibit a number of peaks and valleys equal to the number

of maxima and minima of the r -value directionality (Fig. 24). More precisely, peaks and valleys as defined by the angle θ in the earing profile correspond to maxima and minima, respectively, in the r -value directionality expressed as a function of $\theta + 90^\circ$. Although additional verifications are needed, these results suggest that, for a given material, the relative earing profile and r -value directionality are “mirror images” of each other with respect to the transverse direction.

Example 3: Finite Element Simulation of Reverse Cup Drawing. Reverse cup drawing, proposed as a benchmark example at the NUMISHEET '99 conference (Ref 196) illustrates the importance of the yield function for accurate FE modeling simulations. In this process, plastic anisotropy, friction, and sheet bending/unbending are all relevant parameters. Simulation results were compared with data available from the conference proceedings (Ref 196).

The workpiece material was an aluminum alloy 6016-T4 sheet sample. The stress-strain curve and yield surfaces were described by the Swift law and the Yld2000-2d yield function (Ref 41), respectively. Because the biaxial yield stress was not available for this material, the assumption $\sigma_b = \sigma_0$ was employed, based on

the properties of similar materials. The eight coefficients of Yld2000-2d were obtained with seven input data using the practical assumption $c''_{12} = c''_{21} = 0$ (see the section “Anisotropic Yield Functions” in this article). Tables 6 to 8 list the different data and coefficients used for this material. For this 6016-T4 sheet sample, an excellent agreement was observed between experimental and calculated (Yld2000-2d) variations of the r -value and the flow stress as a function of the angle between rolling and tension direction (Fig. 30). For comparison purposes, the amplitude of the flow stress anisotropy predicted with Hill’s 1948 yield function, also represented in Fig. 30, is largely overestimated. This is because with this classical yield function, the anisotropy coefficients are calculated with the r -values only as input, not the flow stresses.

The specific dimensions of the tools are given in the NUMISHEET '99 proceedings (Ref 196). Only a quarter section of the cup was analyzed in light of the orthotropic material symmetry. Figure 31 shows the FE mesh used for the analysis; it comprised 1050 continuum-based shell elements (Ref 161). The process variables were as follows:

Initial sheet thickness:	1.15 mm (0.045 in.)
Coulomb coefficient of friction:	0.1
Gap between blankholder and die:	2.0 mm (0.08 in.)

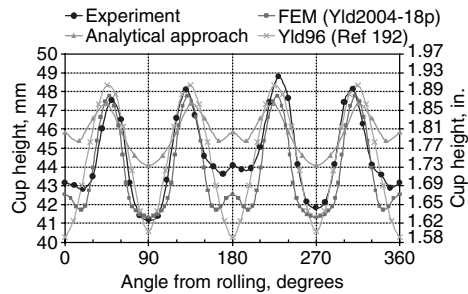


Fig. 27 Comparison of measured earing profiles for deep-drawn cups of aluminum alloy 2090-T3 with predictions from finite element simulations (using two different yield functions) and an analytical model. Source: Ref 195

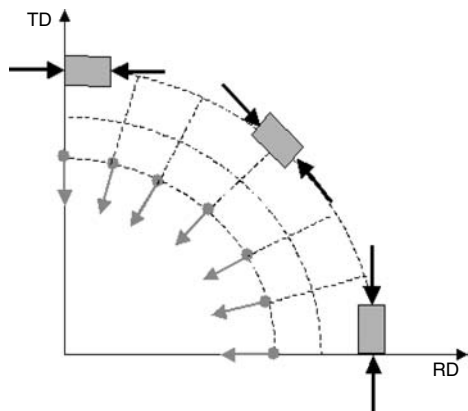


Fig. 28 Illustration of the compressive stresses developing in the elements at the rim of circular blank drawn into a circular cup. TD, transverse direction; RD, rolling direction

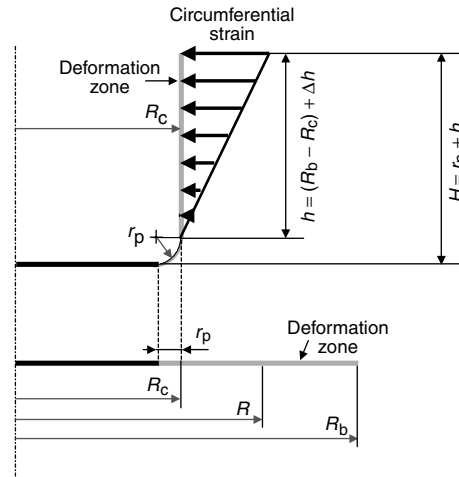


Fig. 29 Initial blank and drawn-cup geometries showing the deformation zone for an analytical solution of the earing problem

Table 6 Swift parameters for aluminum alloy 6016-T4 sheet

Strength coefficient (K)	ϵ_0	Strain-hardening exponent (n)
385.5	0.082	0.239

Table 7 Normalized flow stresses and r -values for aluminum alloy 6016-T4 sheet

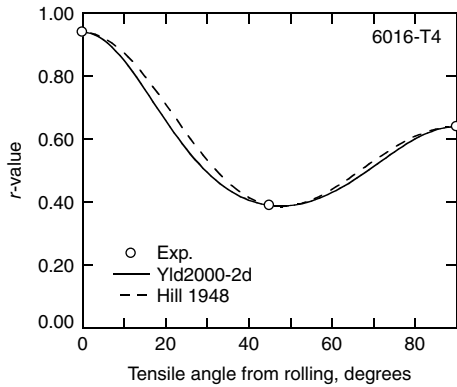
Test	0° uniaxial	45° uniaxial	90° uniaxial	Biaxial
Flow stress	1.000	0.984	0.944	1.000
r -value	0.94	0.39	0.64	n/a

Table 8 Yield function Yld2000-2d coefficients

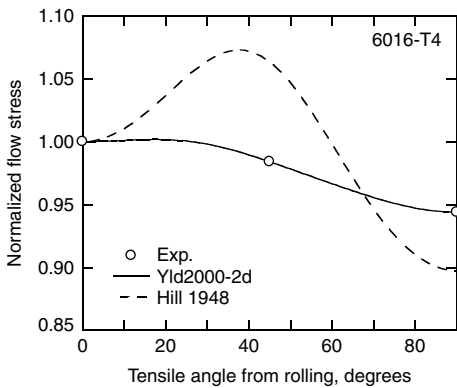
a	α_1	α_2	α_3	α_4	α_5	α_6	α_7	α_8
8	0.9580	1.0450	0.9485	1.0568	0.9938	0.9397	0.9200	1.1482

The cup-drawing simulation was performed assuming isotropic hardening; that is, the yield-function coefficients were kept constant during deformation. It took 120 and 180 steps to translate the punch 60 mm (2.4 in.) in the forward and 80 mm (3.2 in.) in the reverse directions, respectively.

Experimental Validation. Figure 32 shows the deformed cups at intermediate and final stages of the forward and reverse drawing steps. Figure 33 shows that the predicted load-displacement curves agree qualitatively with the experimental curves, although the simulated results underestimate the measured loads. This can probably be attributed to the lack of transverse shear stress in the general thin-shell formulation. Figures 34(a) and (b) show the predicted and experimental thickness-strain distributions measured along the rolling and diagonal (45° from RD) directions, respectively, after the forward and reverse drawing operations. Although the simulated thickness in the flange area in the diagonal direction is slightly



(a)



(b)

Fig. 30 Experimental and predicted (Yld2000-2d and *r*-value-based Hill's 1948) (a) *r*-value and (b) normalized flow stress as a function of tensile angle from rolling for a 6016-T4 aluminum alloy sheet sample

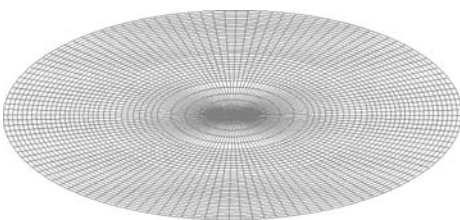
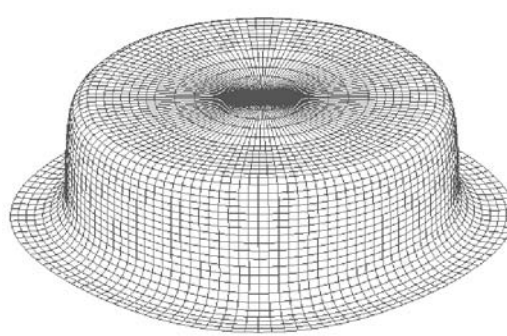


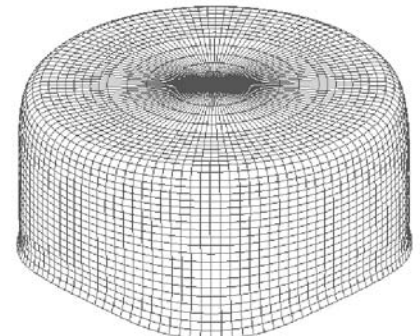
Fig. 31 Initial finite element mesh of the circular blank

overestimated, the agreement between predictions and measurements is generally excellent. The overestimation in the diagonal direction is presumably due to the thin-shell formulation without half-thickness consideration of the sheet material.

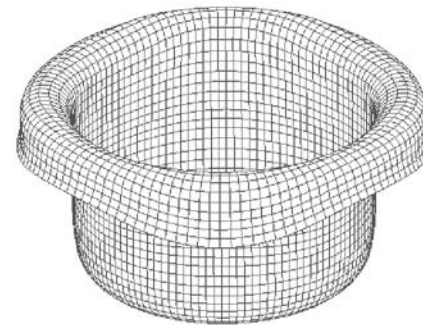
Nevertheless, this example shows that the material description with Yld2000-2d was able to capture experimental results very well despite the assumption of isotropic hardening, in particular, the different strain profiles in the two directions (rolling and diagonal) investigated. Moreover, separate simulations using the more classical yield function proposed by Hill (Ref 35) could not be completed because of convergence issues. It is believed that these problems were



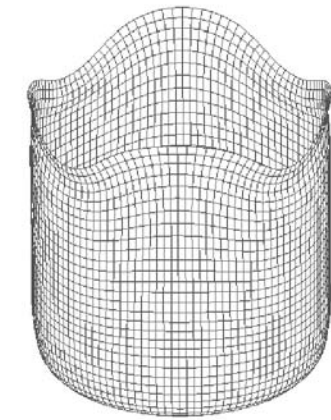
(a)



(b)



(c)



(d)

Fig. 32 Finite element meshes during and after (a) and (b) forward and (c) and (d) reverse drawing operations. Source: Ref 194

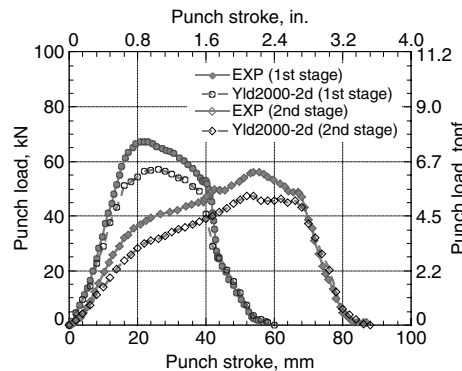


Fig. 33 Measured and FE predicted punch load versus displacement during drawing and redrawing for aluminum alloy 6016-T4 sheet. Source: Ref 194

due to the anisotropy of the sheet, which, as suggested by Fig. 30, was largely overestimated using the more classical yield function. This anisotropy was thought to be responsible for locally excessive blankholder force and element distortion, leading, in turn, to a numerical instability.

Example 4: Modeling of Wrinkling During Cup Drawing. Finite element analysis has also been applied to analyze wrinkling during cup

drawing. For this example, the dimensions of the tooling are as follows:

Punch diameter:	$D_p = 85 \text{ mm (3.3 in.)}$
Punch-profile radius:	$r_p = 7 \text{ mm (0.28 in.)}$
Die opening diameter:	$D_d = 88 \text{ mm (3.5 in.)}$
Die-profile radius:	$r_d = 8 \text{ mm (0.32 in.)}$

The FE analyses were carried out using the Yld91 (Ref 37) planar anisotropic material model (a particular case of Yld2004-18p). One-half of the circular blank was discretized into 2100 elements (30 elements in the radial direction and 70 elements in the circumferential direction) and 2201 nodes (Fig. 35). The wrinkling behavior was described using the bifurcation algorithm mentioned in the section "Compressive Instability" in this article. The process parameters and material constants used in the analysis are listed in Table 9.

Finite element analyses and experiments were carried out to determine the onset of wrinkling and the number of wrinkles for various values of the blankholding force. Figure 36 shows the measured and computed configurations of the cup after partial drawing. The experiments were carried out three times for each value of the blankholding force. When this force was set to 2 kN (0.22 tonf), 14 wrinkles resulted from the FE analysis, while 9, 11, and 12 wrinkles were

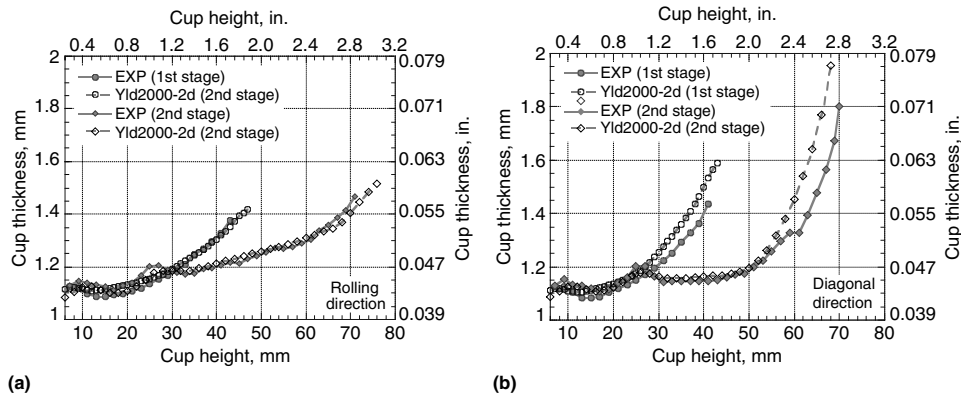


Fig. 34 Cup thickness profiles after drawing/redrawing operations measured along (a) rolling direction and (b) diagonal direction (45° from rolling direction). Source: Ref 194

Table 9 Material constants and friction coefficient for cylindrical cup drawing

Process parameters/material constants	Values
Material	Al 6111-T4
Initial blank thickness	0.9144 mm (0.036 in.)
Coulomb friction coefficient	0.1
Yield stress	185.92 MPa (26.96 ksi)
Young's modulus (<i>E</i>)	69 GPa (10 × 10 ⁶ psi)
Poisson's ratio	0.33
Stress-strain curve	$\bar{\sigma} = 454.8 - 268.8 \exp(-6.45\bar{\epsilon})$
<i>r</i> -value	$r_0 = 0.83, r_{45} = 0.86, r_{90} = 1.42, \bar{r} = 0.99$
Anisotropic coefficients for Barlat's yield (Ref 37)	$c_1 = 1.0406, c_2 = 0.9582, c_3 = 0.9962, c_4 = c_5 = c_6 = 0.9071, a = 8.0$

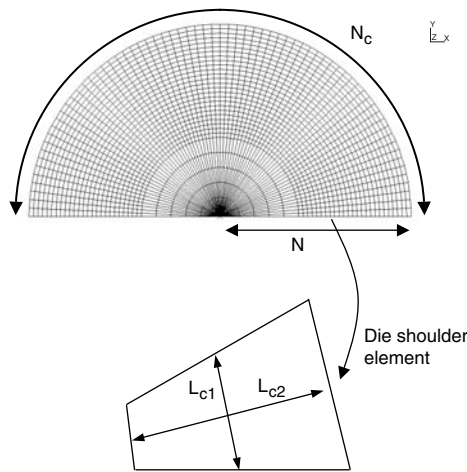


Fig. 35 Mesh used in the analysis of wrinkling and the definition of characteristic lengths

observed experimentally. When the blankholding force was equal to 5 kN (0.56 tonf), 22 wrinkles were predicted, and 17, 18, and 19 were measured. Finally, for a blankholding force of 8 kN (0.90 tonf), the predicted wrinkle number was 32, while the experimental numbers were 24, 27, and 28. The number of wrinkles obtained from the FE analyses were in reasonable agreement with the experimental results. Moreover, the larger number of wrinkles measured on the

cups drawn with a higher blankholding force was well captured by the model.

Figure 37(a) shows the critical punch stroke at which wrinkling grew abruptly, and Fig. 37(b) shows the normalized wrinkle wavelength. In Fig. 37(a), it is shown that the load corresponding to the onset of wrinkling was overestimated by the FE analyses and that the onset and growth of wrinkles was retarded as the blankholding force increased. It is thought that initial imperfections, such as eccentricity of the circular blank with the tool and the nonflatness of the initial blank, may have accelerated the initiation of wrinkling. With the application of grease as a lubricant, a lower force may have led to a larger gap between the blank and blankholder, which could have resulted in imperfections with higher initial amplitudes. Figure 37(b) shows that the normalized wrinkle wavelength decreased (more wrinkles) as the blankholding force increased. This is because, as the blankholding force increased, the lower bifurcation mode was constrained, and wrinkling took place in a higher bifurcation mode. It was also shown in Fig. 37(b) that the number of wrinkles is overestimated (wrinkling wavelength underestimated) by the FE analysis, which is also thought to be due to the effects of imperfections.

Figure 38 shows the normalized critical wrinkling stress for various blankholding forces, which was obtained by averaging the circumferential stress of the edge elements for the

punch stroke at which wrinkling grew abruptly. As can be expected, the critical wrinkling stress increased as the blankholding force increased. Considering the difficulty and sensitivity of all contributing parameters in the modeling of wrinkling, the predictions of the FE analysis are considered to be in very good agreement with the experimental results. This shows that the FE analysis, combined with a bifurcation algorithm, can be used reliably for the analysis of wrinkle initiation and growth in sheet metal forming processes.

Material and Friction Effects. Material properties such as strain-hardening rate and plastic anisotropy can have an effect on the wrinkling behavior of sheet metal. In order to investigate this effect, the initiation and growth of wrinkles in the cylindrical cup-drawing process were computed with the Swift hardening law and Hill's 1948 yield function, assuming planar isotropy (in-plane properties are the same; also called normal anisotropy). Figure 39 shows the simulated critical punch stroke at which wrinkling initiates for various values of the normal anisotropy coefficient, *r*, and of the strain-hardening exponent, *n*. In Fig. 39(a), wrinkling initiation occurred at higher punch strokes (loads) as the value of the anisotropy coefficient increased, and it disappeared when this coefficient reached a value of 2.0. Examination of the yield surface shows that the material can flow plastically with a lower pure shear stress (σ_x) in the flange when the anisotropy parameter *r* is higher. This means that a lower in-plane compressive stress ($\sigma = -\sigma_x$) is needed to deform the material, thus postponing wrinkling to higher loads. Figure 39(b) shows that increasing values of the strain-hardening exponent delayed the onset of wrinkling. Moreover, strain-hardening exponents of 0.25 and 0.3 inhibited the occurrence of wrinkling. This result appears to be reasonable, because a higher strain-hardening exponent leads to a larger elastoplastic modulus. All these simulation results were consistent with the experiments of Narayanasamy and Sowerby (Ref 197), who showed that sheets with higher normal anisotropy and strain-hardening rate resist wrinkling better.

Finite element simulations were also carried out with the Yld91 yield function (Ref 37) in order to assess the influence of planar anisotropy (different in-plane properties) on the wrinkling behavior. The anisotropy coefficients used in this investigation are listed in Table 9. A blankholding force of 3 kN (0.34 tonf) was imposed. Figures 40(a) and (b) show the deformed configurations analyzed with normal anisotropy (Hill's 1948) and planar (Yld91) anisotropy, respectively. For normal anisotropy, wrinkling was predicted to occur at a punch stroke of 25 mm (1.0 in.), and the number of wrinkles was 20. For planar anisotropy, however, the compressive instability initiated at a punch stroke of 20 mm (0.8 in.) and produced 18 wrinkles. This effect was explained by the thickness in the flange, which is no longer uniform due to planar anisotropy. This nonuniformity could induce

imperfections and modify the susceptibility to wrinkling. However, the comparison between these two simulations is not rigorous because, in addition to the two types of anisotropy (normal and planar), two yield functions were used. The difference in wrinkle number could also be influenced by the generally higher shear yield stress of Hill's 1948 yield function compared to Yld91.

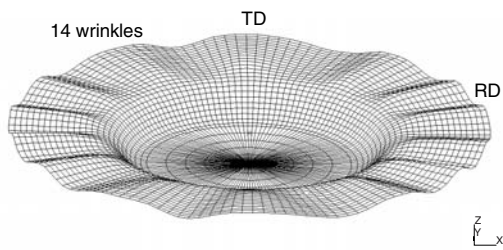
Finite element analyses were performed under constant blankholder force (BHF) with various values of the Coulomb friction coefficient. The corresponding deformed configurations are shown in Fig. 41. When the friction coefficient increased, the number of wrinkles decreased, and when this coefficient reached a value of 0.2, tearing took place instead of wrinkling. Figure 42 shows the number of wrinkles, the critical punch

stroke at which wrinkling grows abruptly, and the edge draw-in for various values of the friction coefficient. It was shown that if wrinkling initiates a higher punch stroke, the number of wrinkles decreases. This is due to the fact that edge draw-in decreases because of the higher friction force, and therefore, lower compressive circumferential stress is induced.

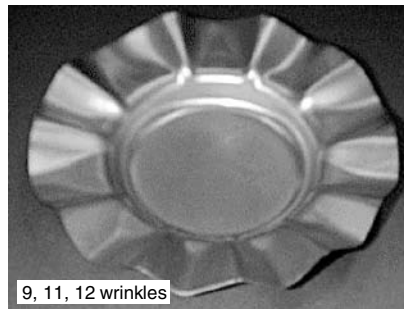
Example 5: Finite Element Simulation of Hemming Operations. Hemming is a process used in the automotive industry to join inner and outer skins of components such as hoods, doors and deck lids. Hemming is a 180° bending operation conducted in three steps: a bending or flanging step, followed by prehemming and final hemming steps. Parameters such as the die radius, the flange radius and length, and the prehemming punch travel influence the final

product quality. Typical Al-Mg-Si 6XXX-T4 sheet processed by conventional means usually produces acceptable relieved flat hem ratings.

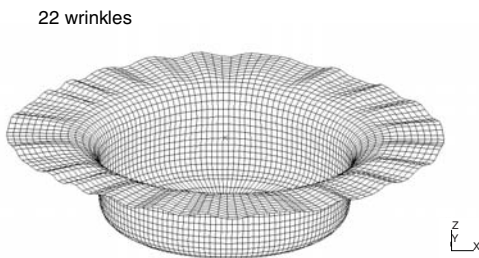
In this example, a specific 6XXX-T4 alloy sheet exhibited successful flat hemming when the hem line was aligned with the rolling



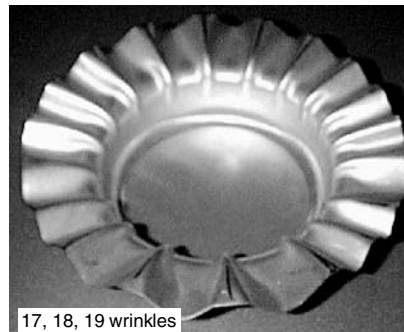
(a)



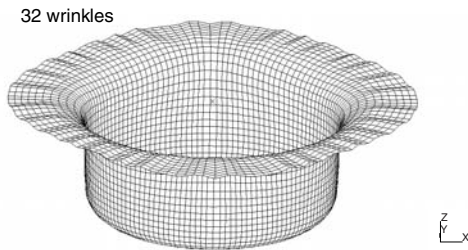
(b)



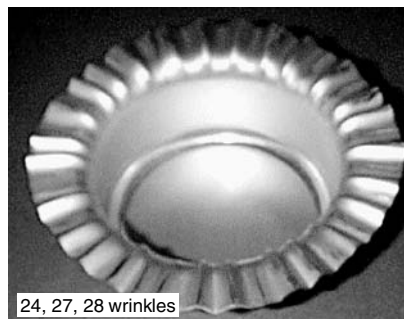
(c)



(d)

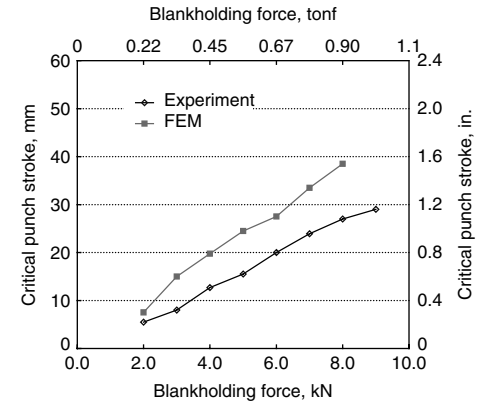


(e)

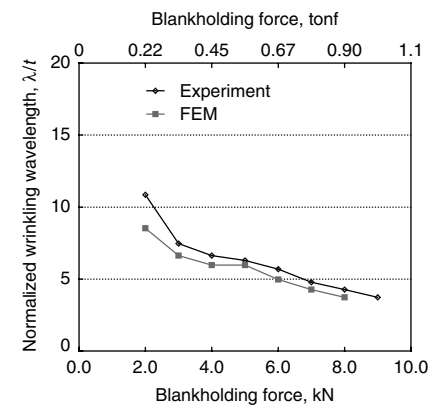


(f)

Fig. 36 Finite element predictions (FE) and experimental observations (EXP) of wrinkling in cups drawn with various levels of blankholder force (BHF). (a) FE, BHF = 2 kN (0.22 tonf), stroke = 12 mm (0.5 in.). (b) EXP, BHF = 2 kN (0.22 tonf), stroke = 10 mm (0.4 in.). (c) FE, BHF = 5 kN (0.56 tonf), stroke = 30 mm (1.2 in.). (d) EXP, BHF = 5 kN (0.56 tonf), stroke = 20 mm (0.8 in.). (e) FE, BHF = 8 kN (0.90 tonf), stroke = 40 mm (1.6 in.). (f) EXP, BHF = 8 kN (0.90 tonf), Exp, stroke = 35 mm (1.4 in.). Source: Ref 103



(a)



(b)

Fig. 37 Comparison of measurements and finite element (FE) predictions of (a) critical punch stroke and (b) normalized wrinkling wavelength for various levels of blankholder force. Source: Ref 103

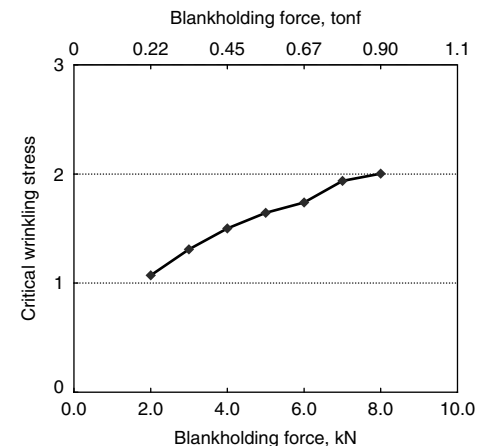


Fig. 38 Finite element predicted normalized critical wrinkling stress for various levels of blankholder force. Source: Ref 103

direction (RD-oriented hem). However, when the hem line was aligned with the transverse direction (TD-oriented hem), unacceptable hem ratings, that is, with some amount of cracking, could be observed. Because of mechanical

fibering, it is counterintuitive that the RD-oriented hem leads to a better performance than the TD-oriented hem.

It is known that the stress level affects shear localization and cracking, everything else being constant. Therefore, these analyses pointed to the influence of the stress on fracture during hemming. The stress state that is prominent in hemming corresponds to plane strain, characterized by the major component σ_p . The relevant values of this stress component are associated with the RD and TD directions for the

two specific cases of TD- and RD-oriented hemming, respectively. These stresses can be evaluated relative to the RD tensile yield stress, σ_y , using the yield surface concept. The plane-strain yield stress is a function of the anisotropy ratio $H = \sigma_p/\sigma_y$, which depends on the yield-surface shape and consequently on crystallographic texture. Therefore, texture analyses and crystal-plasticity yield-surface calculations were conducted for typical and experimental 6XXX-T4 sheet samples. The results showed that, in general, the yield surface was distorted (anisotropic) and that the RD plane-strain yield stress, σ_p^{RD} , was higher than the TD plane-strain yield stress, σ_p^{TD} , particularly for the experimental material. This may explain why RD-oriented hemming was acceptable (lower σ_p^{TD}) and TD-oriented hemming was more prone to fracture (σ_p^{RD} much higher) for the experimental material. Because it is usually desired to maximize σ_y for product applications, the other control parameter, H , can be modified to reduce the plane-strain yield stress. In this particular example, texture analyses and crystal-plasticity models can be used to define the appropriate texture and provide information for alloy processing. This aspect is not covered here, but the simulation of the hemming process is.

Finite element simulations of the hemming process were carried out for the 6XXX-T4 sheet sample in the RD and TD orientations using the Yld2004-18p yield function to account for plastic anisotropy. The material data for the conventionally processed alloy are shown in Ref 198. Figure 43 summarizes the results. This figure shows that the maximum plastic strain computed in the bent area is approximately the same for all specimens but one, that is, the TD-oriented hem specimen for the experimental alloy. This is in good agreement with observations, because this specimen only exhibits cracks on the hem line. Figure 44 shows a close-up view of one of the simulated hem specimens. It shows that the maximum strain is not located at 90° with respect to the plane of the sheet but in a location that agrees well with experimental observations of the cracking zone.

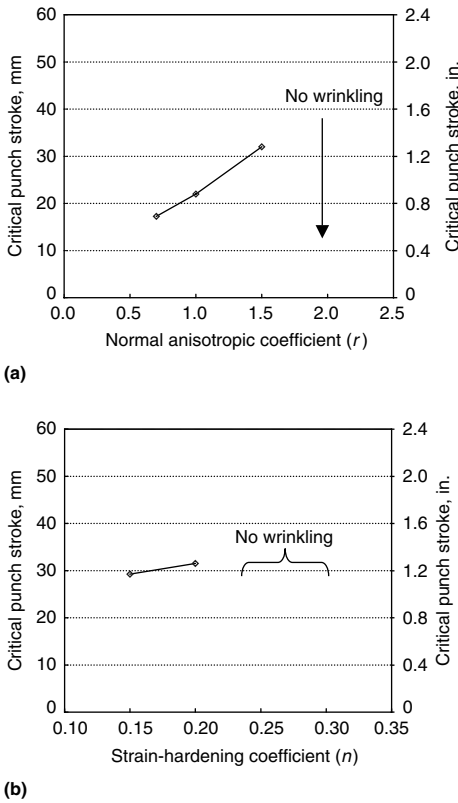


Fig. 39 Finite element (FE) predicted dependence of the critical punch stroke on (a) normal anisotropy (r -value) and (b) strain-hardening exponent (n -value in Swift law). Source: Ref 103

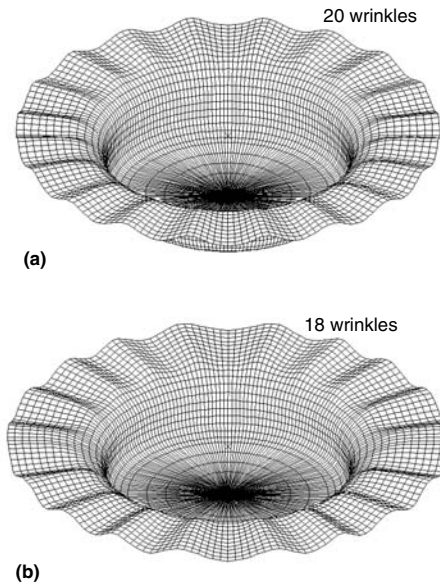


Fig. 40 FE predicted effect of planar anisotropy on wrinkling behavior. (a) Normal anisotropy (Hill's 1948 yield function, stroke = 25 mm, or 1.0 in.). (b) Planar anisotropy (Yld91 yield function, stroke = 20 mm, or 0.8 in.). Source: Ref 103

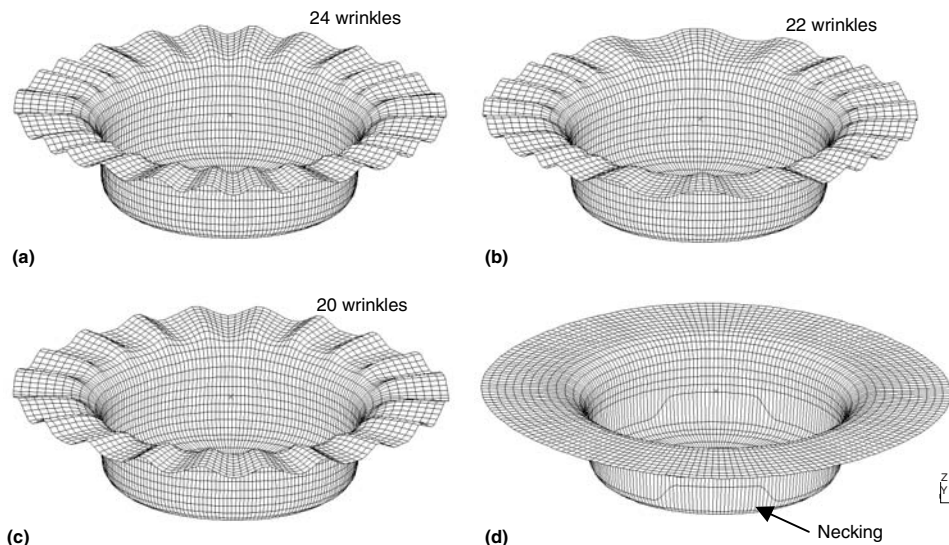


Fig. 41 FE predictions of the effect of friction on wrinkling behavior. (a) $\mu = 0.0$. (b) $\mu = 0.05$. (c) $\mu = 0.1$. (d) $\mu = 0.2$. Source: Ref 103

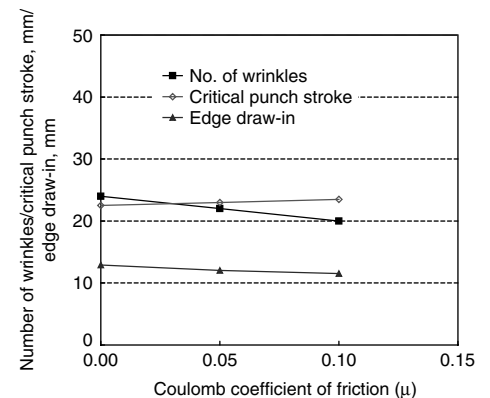


Fig. 42 Effect of Coulomb coefficient of friction on wrinkling behavior. Source: Ref 103

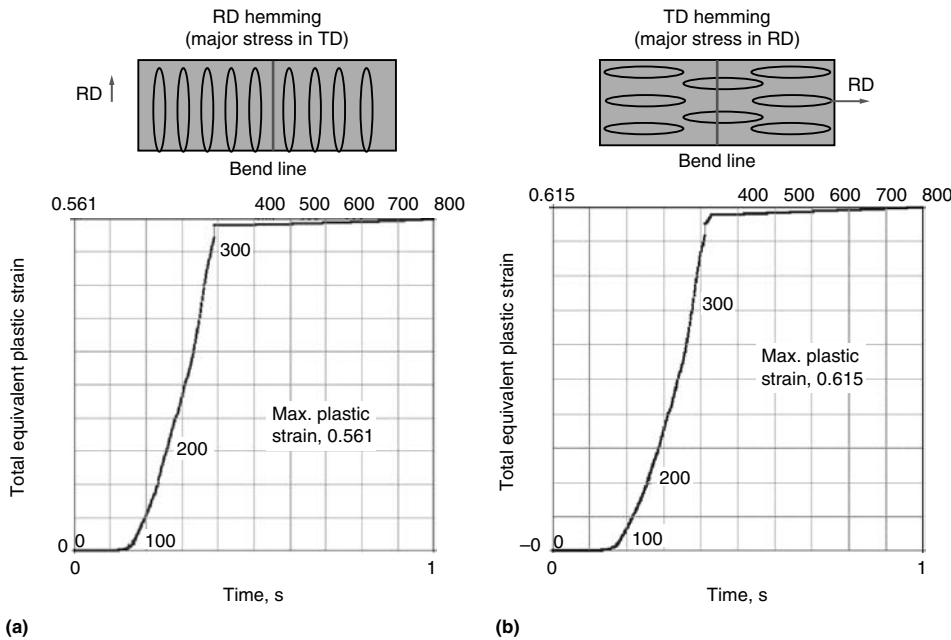


Fig. 43 Simulation of hemming directionality for experimental Al-Mg-Si T4 alloy sheet. (a) Bend line parallel to rolling direction (RD). Failure resistance is lower but so is driving force (strain); better overall. (b) Bend line perpendicular to rolling direction. Failure resistance is higher, but so is driving force (strain); worse overall

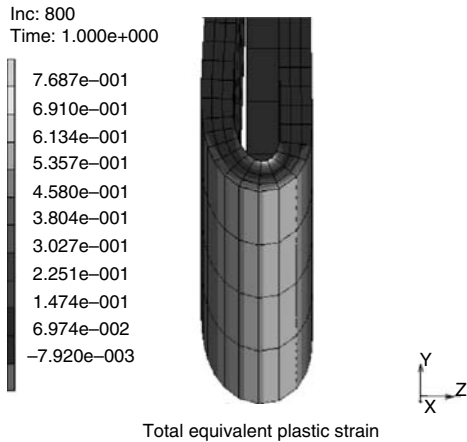


Fig. 44 Close-up view of finite element (FE) predicted plastic strain distribution after flat hemming

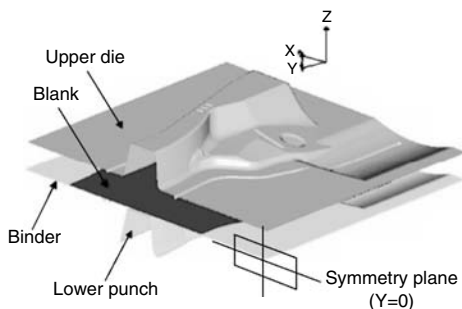


Fig. 45 Forming tool setup for an automotive underbody cross-member panel

Example 6: Finite Element Simulation of Automotive Panel Stamping. Finite element analysis can be applied to the more complex forming problems encountered in industry. The present example deals with the application of FE analysis to the stamping of an automotive component. The final shape of an underbody cross-member panel results from three major steps: forming, trimming/piercing, and springback. In this example, the final shape of the part is particularly dominated by the effect of springback. The lower punch, binder, and upper die used during forming are illustrated in Fig. 45. This tooling geometry had a x - z plane of symmetry at $y = 0$. A 5182-O aluminum alloy sheet, 1.6 mm (0.06 in.) thick, was used as a blank material. In order to characterize the material with Yld2000-2d and Yld2004-18p yield functions (see the section “Anisotropic Yield Functions” in this article), tensile tests conducted in different directions from rolling, with angles in 15° steps, as well as bulge and disk-compression tests were performed. Figure 46 shows that the experimental r -value and flow-stress directionalities are very well captured Yld2000-2d and Yld2004-18p yield functions.

The process parameters used in the forming simulation were as follows:

Total blankholder force:	400 kN (45 tonf)
Binder travel:	100 mm (4 in.)
Tool moving direction	
Upper die:	Moving in the $-z$ -direction
Binder:	Moving in the $-z$ -direction

In the forming simulation, the maximum downward velocity of the upper die was limited

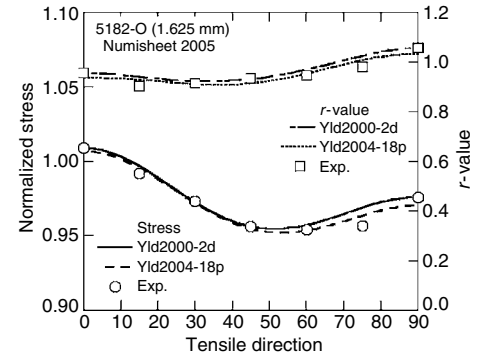


Fig. 46 Normalized flow stress and r -value experimentally measured and calculated using Yld2000-2d and Yld2004-18p yield functions as a function of the angle between the rolling and tensile directions for an aluminum alloy 5182-O sheet sample

to 5 m/s (16 ft/s). The initial setup positions and physical dimensions of the draw beads were well described in the benchmark specifications (Ref 198). In the present forming simulation, line beads were used. The initial blank was modeled with coarse meshes (3124 shell elements). During the forming simulation, two-level adaptive mesh refinement was applied, and the final number of elements after forming was 27,610. Figure 47 shows that the plastic strain contours predicted with Yld2000-2d and Yld2004-18p are almost coincident. The reason is that, as suggested in Fig. 46, both yield functions predict the same plastic behavior. The calculations based on Yld2000-2d and Yld2004-18p took approximately 3 and 13 h, respectively.

Figure 48 shows the sections used for the draw-in measurements (d_1 , d_2 , etc.). In this simulation, a penalty method was used to enforce the contact conditions. The use of a very large penalty coefficient could cause partial contact of the left lower corner of the part, because of the coarseness of the mesh. This partial contact could result in very inaccurate draw-in. In order to establish the whole contact of the sheet under the binder, an appropriate penalty coefficient should be used. In this work, a finer mesh was used, which drastically reduced, the influence of the penalty parameter. Table 10 shows that the amounts of draw-in predicted by the FE simulation were in good agreement with the measurements, even though the simulation used a line-bead approach.

After forming, trimming and piercing were simulated with the aid of the IGES line data (a given international standard for surface file format). Figure 49 shows the step-by-step procedure. All the state variables were mapped without any changes during the trimming and piercing processes.

Springback. The boundary conditions for the springback analysis of the underbody cross-member panel are shown in Fig. 50. In addition to the x - z plane of symmetry, boundary conditions were applied at two points (“A” and “B”) in

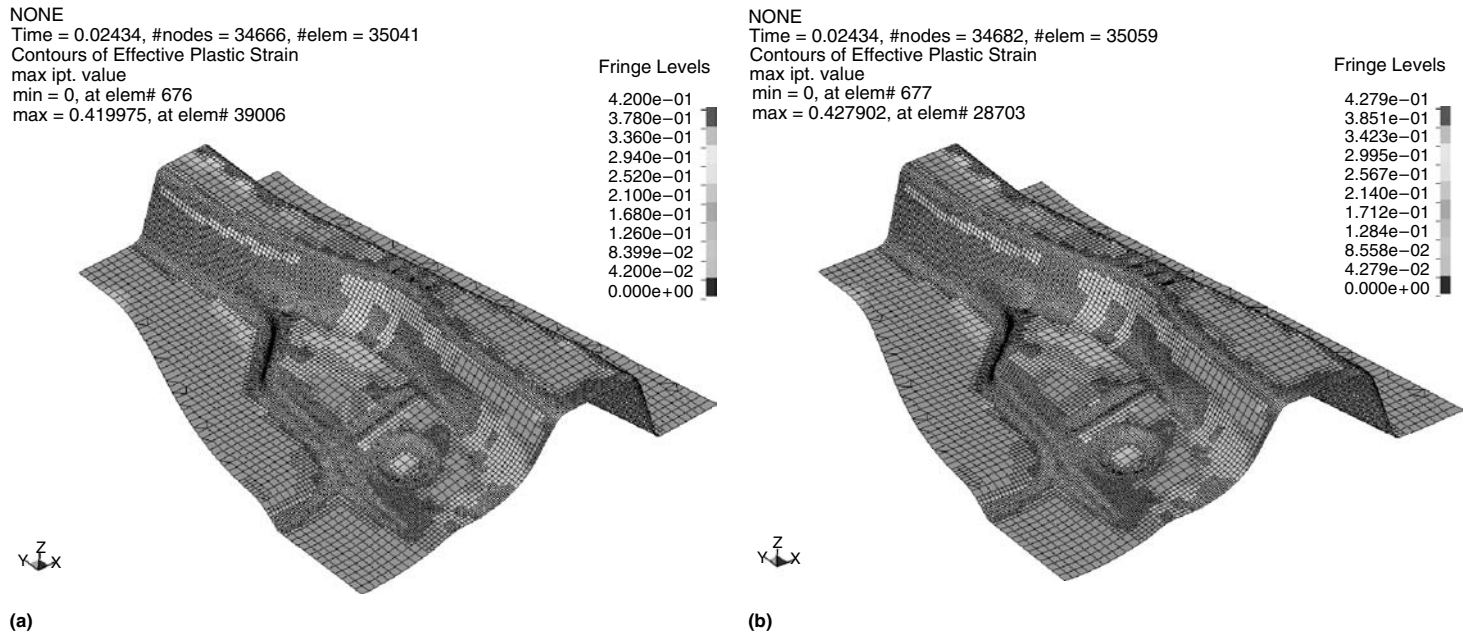


Fig. 47 Effective strain contours predicted using (a) Yld2000-2d and (b) Yld2004-18p. The maximum effective strain for each was 0.42

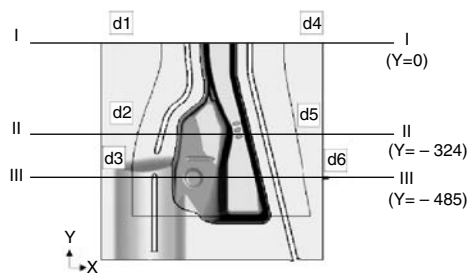


Fig. 48 Measurements of draw-in at sections I, II, and III of the automotive underbody cross-member panel

order to eliminate any rigid body motion. Figures 51 and 52 show the predicted displacement magnitude and the effective stress contour before and after springback, respectively. It can be observed that the effective stress level is higher before than that after springback. This means that springback occurs in a direction that minimizes the residual stresses. The predicted amounts of draw-in and the profiles of specific sections of the panel (Fig. 53: section I, $y = 0$, and section IV, $y = -370$) after springback were compared with experimental results. Figure 54(a) shows that the prescribed profile obtained from the present simulation for section I was in excellent agreement with the experiment. In particular, the curled shape of the right wall was well predicted. Figure 54(b) shows the comparison between experiment and simulation results of section IV. The lifting of the left part and curling of the right wall were very well captured by the simulation and the predicted profile was in excellent quantitative agreement with the experiment.

Table 10 Blank draw-in amount at various locations after forming (Fig. 48)

Measured in mm (in.)

Method	Draw-in location					
	d1	d2	d3	d4	d5	d6
Experiment	62.17 (2.45)	52.8 (2.08)	56.67 (2.23)	73.7 (2.90)	57.2 (2.25)	47.8 (1.88)
Simulation	60.0 (2.36)	50.7 (2.00)	56.9 (2.24)	73.5 (2.90)	57.7 (2.27)	50.5 (1.99)

Example 7: Finite Element Modeling of Tube Hydroforming Processes. Hydroforming has been an important sheet metal forming processes since it was developed before World War II for application to the German aircraft industry (Ref 199). Approximately 30 years ago, hydroformed parts were fabricated by expanding straight or prebent tubes to manufacture manifold elements and components for sanitary use. Hydroforming offers several advantages compared to conventional manufacturing via stamping and welding (Ref 200), in particular, part consolidation and tooling cost. Moreover, while saving on material and manufacturing costs, hydroforming allows the production of parts with improved performances, such as weight, strength, and stiffness, compared to conventionally processed parts in a variety of applications (Ref 201). Today (2006), many hydroformed products, including exhaust manifolds, engine cradles, exhaust pipes, space frames, and so on, are mass-produced in the automotive industry (Ref 202, 203).

Tube hydroforming is a complex process, and it is essential to understand the basic technology to take advantage of the inherent formability of the material. In this process, while the tube is pressurized, axial forces are applied to its ends in order to overcome frictional effects, which cause

premature failure by strain localization. However, if the axial forces are too large, buckling or wrinkling can occur. Consequently, a proper combination of internal pressure and axial compressive force is important to prevent necking (therefore, tearing) as well as buckling. In addition to these process parameters, it is necessary to understand the influence of the tooling geometry, lubrication, and material behavior. Designing die and preform shapes, especially in the early stage, is one of the most difficult tasks. Optimal design is essential to produce final products without defects and to effectively reduce production time.

Recently, FE analyses were applied to the design of the tube hydroforming forming process. Guan (Ref 204), Kridili et al. (Ref 205), and Koc and Altan (Ref 206) simulated axisymmetric tube bulging, while Hwang and Altan (Ref 207) simulated the crushing performance of circular tubes into folds with an overall triangular cross section. Koc et al. (Ref 208) predicted the protrusion height of T-shaped parts using a three-dimensional FE analysis. Because a prebending process often precedes hydroforming, it is important to take into account the deformation during prebending in the simulations. Using FE analyses, some researchers have investigated the cross-sectional

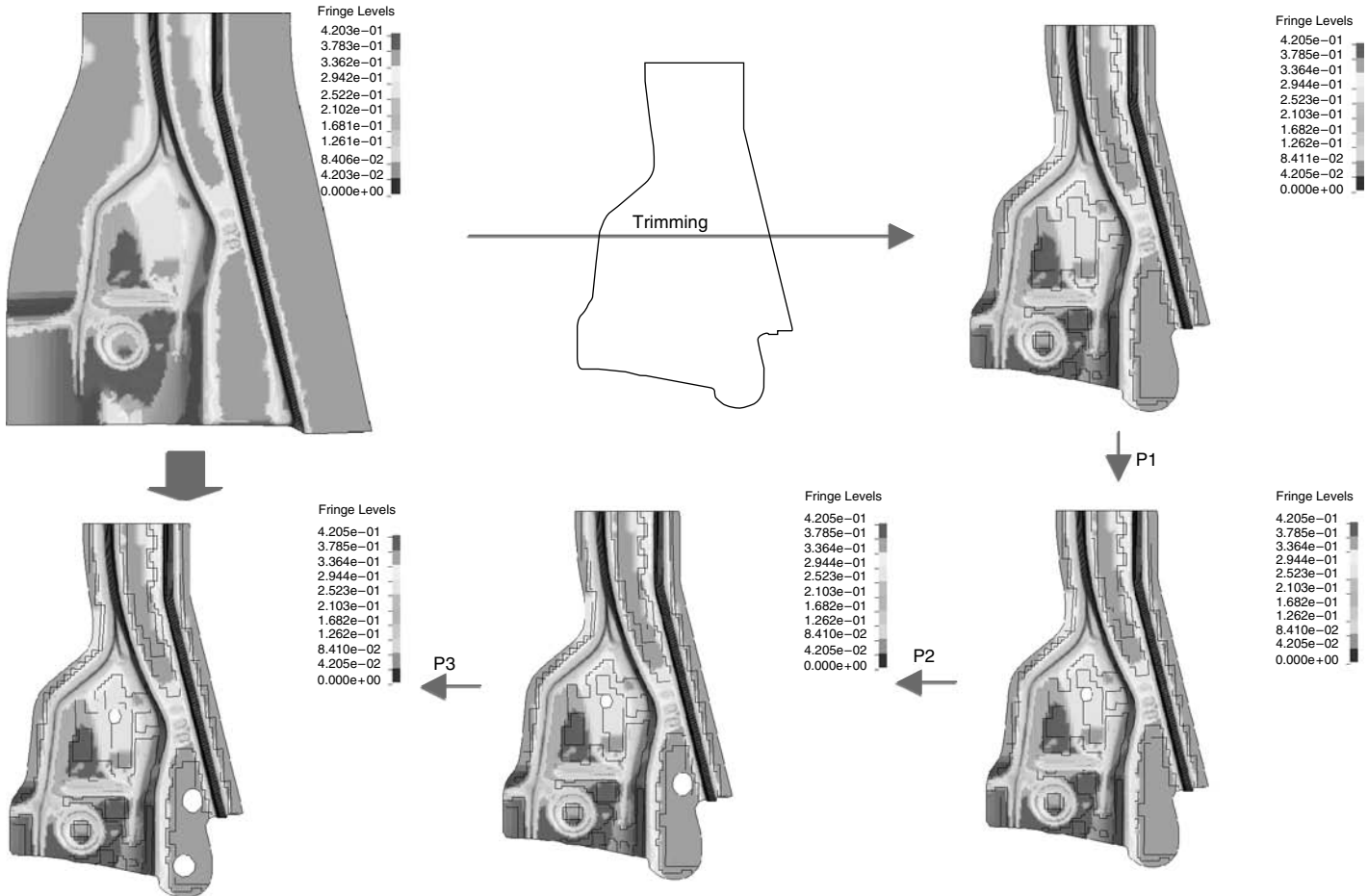


Fig. 49 Trimming and piercing procedure for the automotive underbody cross-member panel

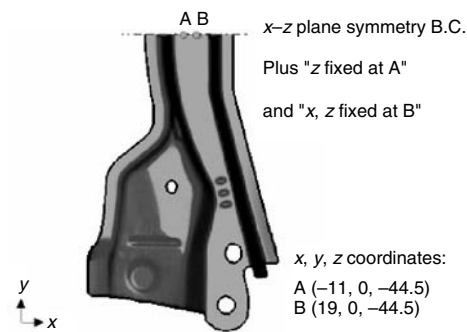


Fig. 50 Boundary conditions for the springback analysis of the automotive underbody cross-member panel

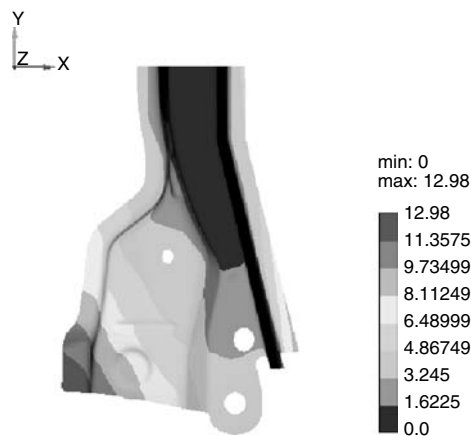


Fig. 51 Predicted displacement magnitude after springback of the automotive underbody cross-member panel

shape change and wall thinning during prebending and integrated the results in subsequent hydroforming simulations (Ref 209–211). Yang et al. (Ref 212) further included springback after the prebending operation. Berg et al. (Ref 213) developed a numerical scheme to overcome problems due to concave cross-sections introduced by local buckling during prebending and preforming processes. For the optimization

of the tube hydroforming in the design stage, several schemes based on FE analyses have been introduced (Ref 214–216). Chung and Yoon (Ref 217) applied a direct FE method (FE design) based on the ideal forming theory (see

the section “Ideal Forming Design Theory” in this article) to design the preform for tube hydroforming.

Preform Design. The use of the ideal forming theory for the optimal design of preforms is illustrated on two industrial hydroformed parts. The examples illustrate how the cross-sectional shape and the tube length can be optimized. Assuming that the final geometry is specified and, as a constraint, the initial thickness of the tube is imposed, an optimal straight, hollow preform (before bending) is determined from this design theory.

In the two examples, the isotropic strain-rate potential $Srp93$ (Ref 51, 52, as well as the section “Strain-Rate Potentials” in this article) was used to describe the material plasticity, with the exponent set to the recommended value of $b = 4/3$ for aluminum alloys. The stress-strain curve was approximated by the Swift law with the following parameters $\bar{\sigma} = 359.8(0.001 + \bar{\epsilon})^{0.223}$ MPa.

For the first example, the uniform thickness of the tube preforms was assumed to be equal to 2 mm (0.08 in.). The final part shape after hydroforming is shown in Fig. 55. Only a half-section was considered in the simulation in

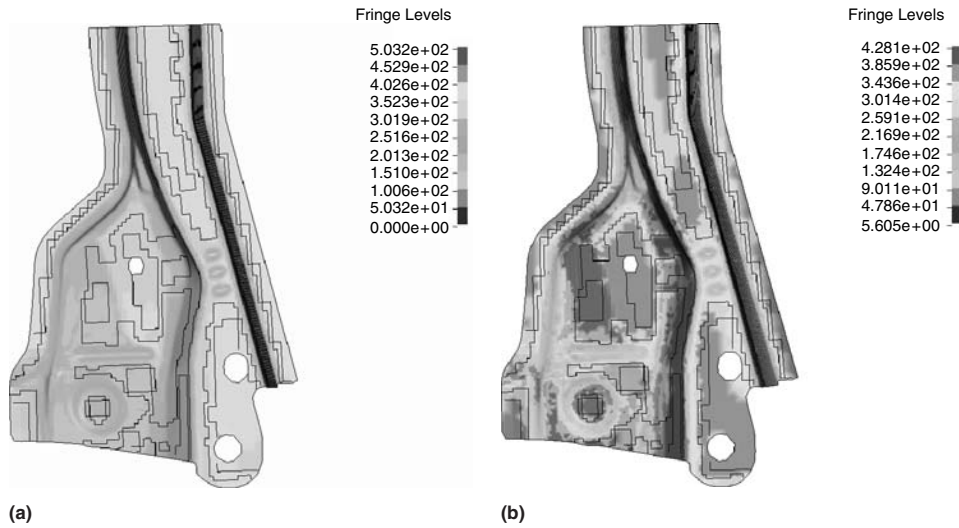


Fig. 52 Predicted effective stress contour (a) before and (b) after springback of the automotive underbody cross-member panel

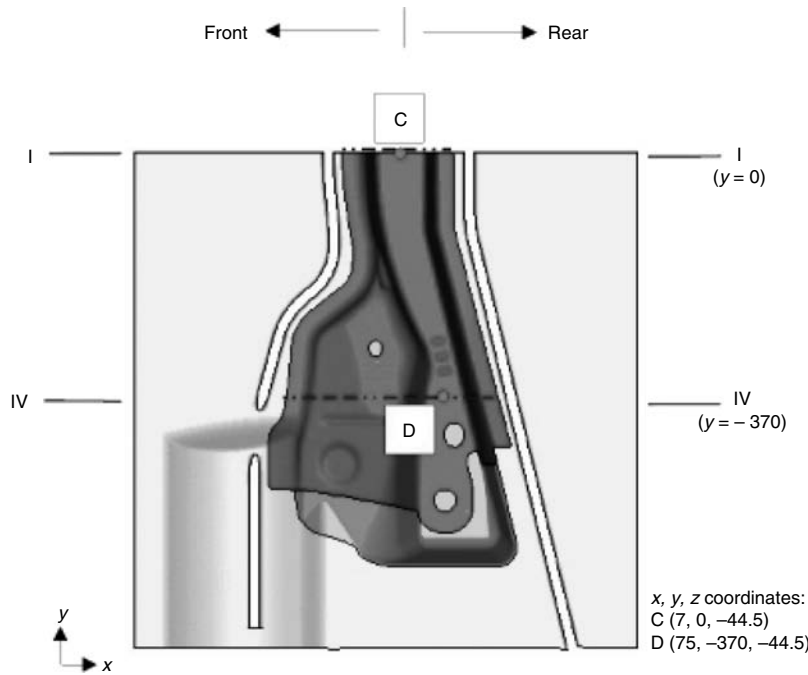


Fig. 53 Definition of sections I and IV of the automotive underbody cross-member panel

view of the part symmetry. Because the solution is the result of a one-step procedure, it took only 2 min to complete the calculation of the initial preform shape. The ideal forming design code showed that the amount of optimal end feeding was 3.3 mm (0.13 in.), with an average pressure of 60.8 MPa (8.8 ksi), while the experimental feeding and pressure were 3.7 mm (0.15 in.) and 75 MPa (10.9 ksi), respectively, to successfully manufacture the final part. Figure 56 compares the thickness strains predicted with friction coefficients of 0.15 and 0.0 (no friction). This figure shows that when the

frictional effect is incorporated, more thinning is observed.

In the second example, the part geometry shown in Fig. 57 was considered. Figure 58 represents the predicted optimal preform tube calculated with the ideal forming code, neglecting the influence of friction. The results showed that the optimal cross section was not circular but close to an ellipse. The predicted thickness strain contours, which are also an output of the model, are plotted on the final part geometry in Fig. 57.

These two examples illustrate that the ideal forming code can provide useful information in

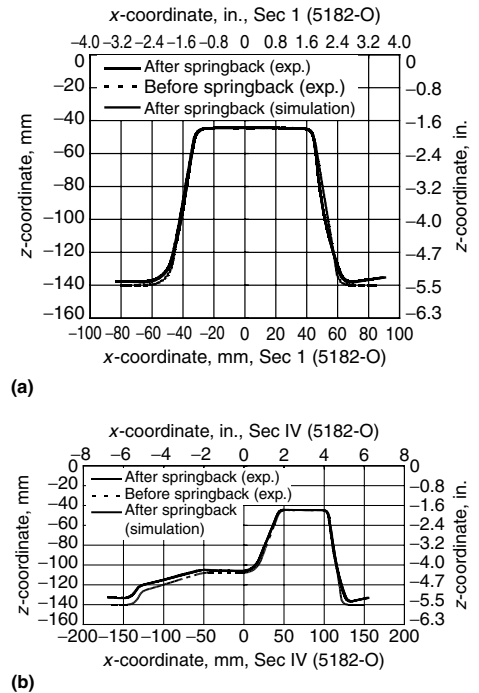


Fig. 54 Profiles of automotive underbody cross-member panels at (a) section I and (b) section IV for 5182-O sheet sample. Experimental and predicted profiles after springback are almost coincident.

the early stage of design, which ultimately reduces the number of FE iterations required to finalize the design of a forming process.

Example 8: Finite Element Simulations in the Design of a Beverage Can End. In the rigid-packaging industry, products with smaller cut-edges and reduced design characteristics have been proposed to decrease overall product costs. However, for beverage can applications, clam-shell failures, as shown in Fig. 59(a), are often observed for many of the newly proposed end designs. Thus, a new geometric design that further increases the buckle pressure without clam-shell failure is an important and critical issue. In this example, finite element (FE) simulations were conducted to predict the resistance to clam-shell buckling and failure in the context of a Taguchi design approach (Ref 1). A plane stress yield function (Yld2000-2d; Ref 41), which accurately describes the behavior of aluminum alloy sheet was employed to model plastic anisotropy (see Fig. 7). The criterion for clam-shell failure was the forming limit curve (FLC) discussed in the section “Tensile Instability” in this article. Once the failure shape was properly predicted, the Taguchi method was used to extract the most important factors from the many possible design variables and to evaluate their influence on the initial buckle pressure. Finally, a new optimum design was proposed to improve the buckle pressure without clam-shell failure.

Buckle Pressure Calculation. In order to predict the buckle pressure, the center displacement

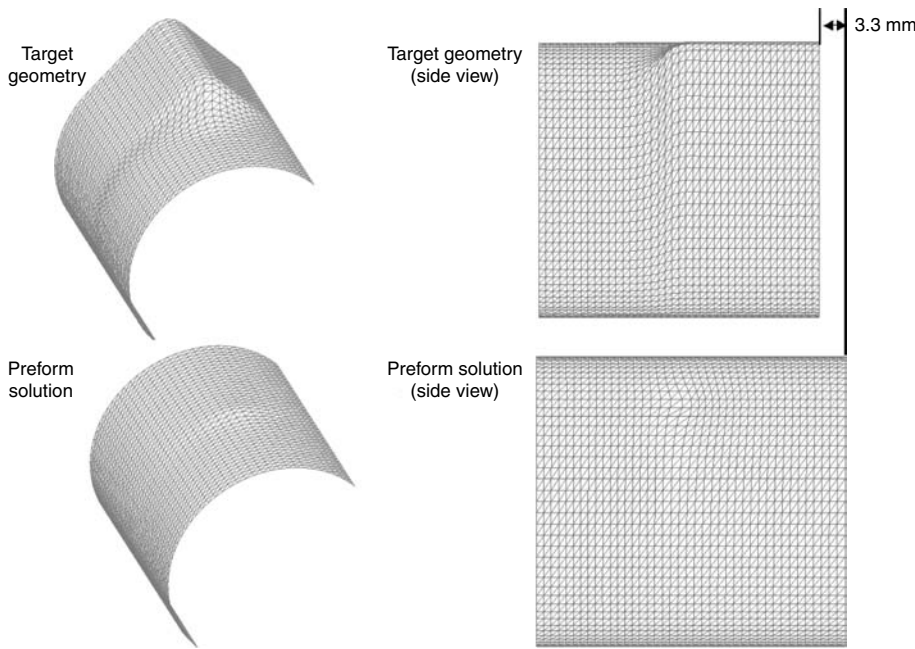


Fig. 55 Final part shape and FE predicted optimal preform shape for hydroforming of aluminum alloy 6061-T4 tube. Source: Ref 217

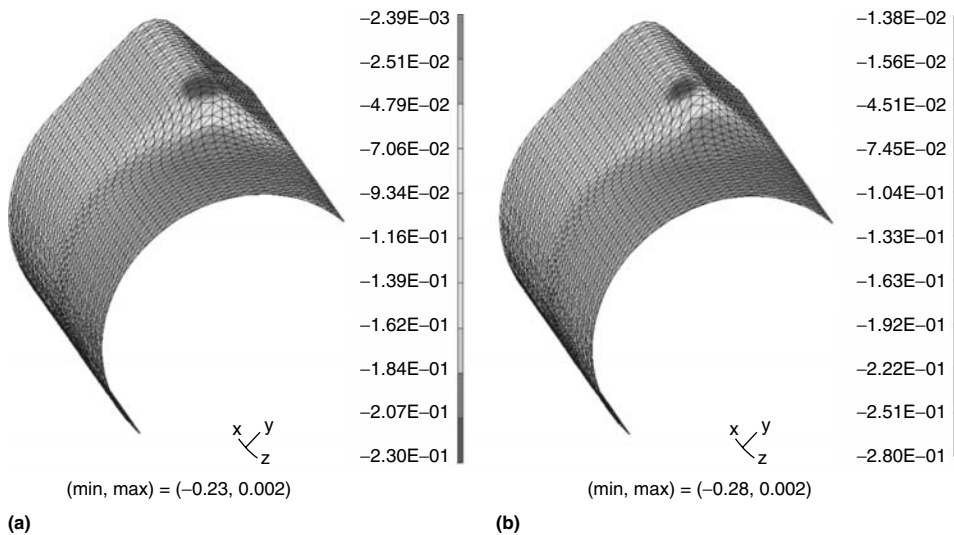


Fig. 56 FE predicted thickness strain assuming (a) no friction and (b) friction coefficient $\mu = 0.15$. Source: Ref 217

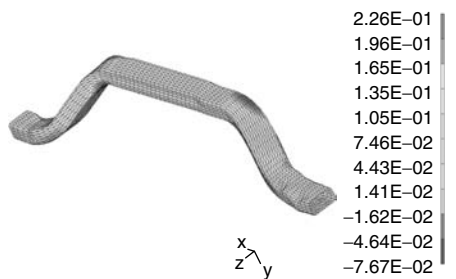


Fig. 57 Final part shape (input for FE design code) and predicted thickness strain contours for hydroforming of aluminum alloy 6061-T4 tubes. Source: Ref 217

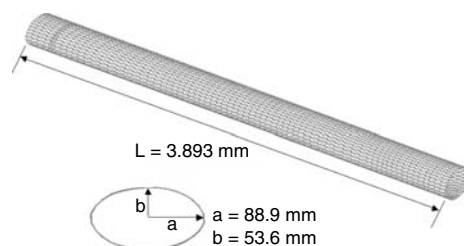


Fig. 58 Predicted optimal preform tube with near-elliptical cross section. Source: Ref 217

of the shell was obtained from FE simulations. Figure 60 shows a schematic illustration of the shell center displacement as a function of pressure at several stages. The displacement at the center increases gradually at the early stage of pressurization. After this transient period (at the end of which the clam-shell initiates), the displacement increases abruptly. The pressure associated to this rapid change is defined as the critical buckle pressure and corresponds to the intersection of the two tangent lines in Fig. 60. Figure 59 compares the observed and simulated deformed shapes of the can end, which are in excellent agreement.

Design Optimization. After confirming the applicability of the FE simulation approach, a number of numerical simulations were conducted instead of experiments to optimize the design parameters in an efficient way. Eight among the twelve geometrical parameters shown in Fig. 61 were selected as variables (denoted A to H in Table 11) to design the best geometry allowing an increase of the buckle pressure. An L_{18} orthogonal array (Ref 1, 218) was constructed to define a set of 18 simulations (Table 11), which were used to evaluate the influence of each of the eight selected design parameters on the buckle pressure (Fig. 62). By this means, Parameter G was found to be most critical factor influencing the buckle pressure.

Further work was conducted in investigate in more detail the influence of this parameter and other conditions. Using the FE simulations, it was found that a buckle pressure of $p_{final} = 0.64$ MPa could be obtained by judicious choice of the design geometry. This pressure was 0.07 MPa (11%) higher than the maximum pressure obtained with the original can end design. Moreover, the new design led to reduction of the maximum effective strain from 0.56 to 0.19, preventing the occurrence of clam-shell failure. Figure 63 shows the simulated and experimental deformed shapes based on the new design, which did not lead to clam-shell failure.

Conclusions

The FE method applied to sheet metal forming process analysis and design, particularly for aluminum alloys, was briefly summarized in this article. Special emphasis was paid to the constitutive modeling and its implementation in FE codes. Tensile and compressive instabilities, which limit the formability of materials, as well as springback, which compromises the overall shape stability of a part, were analyzed. A few issues in the FE method, such as kinematics, element and matrix formulation, as well as stress-integration algorithms, were discussed. The ideal forming theory was briefly introduced as a direct method for the design of sheet-forming or hydroforming processes.

In this article, specific constitutive models suitable for aluminum alloy sheets (or thin tube) were presented. These models were always able

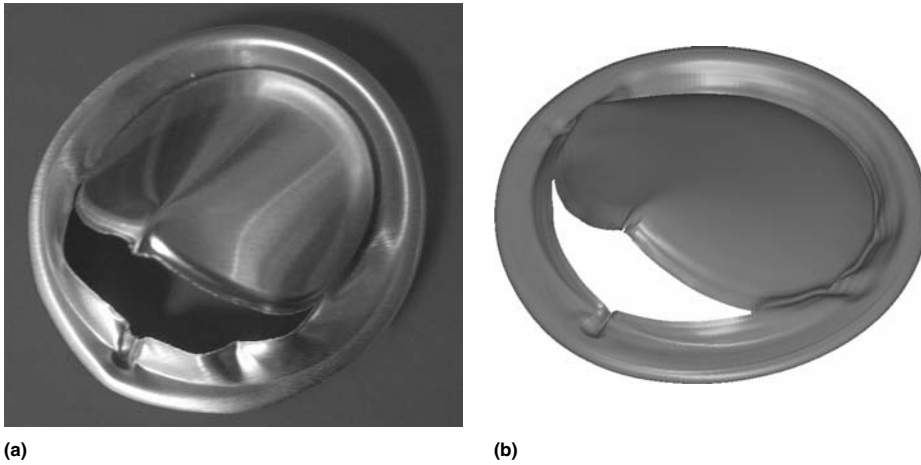


Fig. 59 Comparison of (a) observed and (b) predicted clam-shell failure for the original beverage-can end design

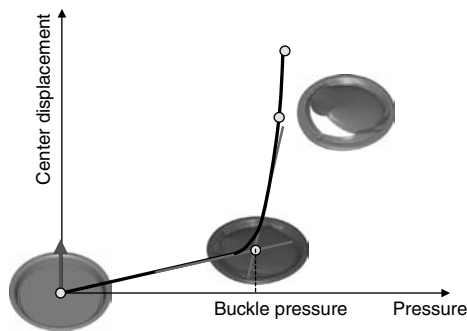


Fig. 60 Shell center displacement versus pressure curve, and the determination of the buckle pressure

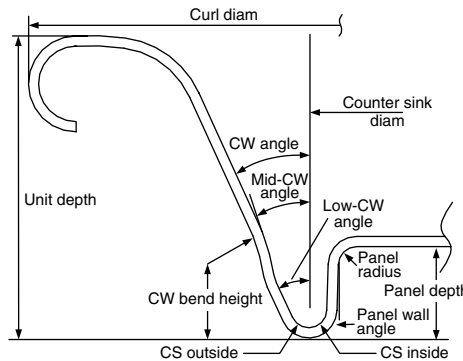


Fig. 61 Schematic illustration of design parameters for beverage-can ends. CW, chuck wall; CS, countersink

Table 11 Orthogonal array for L_{18} in Taguchi method

Run #	A	B	C	D	E	F	G	H
C1	1	1	1	1	1	1	1	1
C2	1	1	2	2	2	2	2	2
C3	1	1	3	3	3	3	3	3
C4	1	2	1	1	2	2	3	3
C5	1	2	2	2	3	3	1	1
C6	1	2	3	3	1	1	2	2
C7	1	3	1	2	3	1	2	3
C8	1	3	2	3	1	2	3	1
C9	1	3	3	1	2	3	1	2
C10	2	1	1	3	2	3	2	1
C11	2	1	2	1	3	1	3	2
C12	2	1	3	2	1	2	1	3
C13	2	2	1	2	1	3	3	2
C14	2	2	2	3	2	1	1	3
C15	2	2	3	1	3	2	2	1
C16	2	3	1	3	3	2	1	2
C17	2	3	2	1	1	3	2	3
C18	2	3	3	2	2	1	3	1

Note: Numbers refer to the levels of design parameters within design range. 1, lower bound, 2, middle level, 3, upper bound

to capture experimental strain-hardening and plastic anisotropy features favorably. A variety of examples of sheet metal forming process simulations, such as cup-drawing, hemming, stamping, springback, hydroforming, and so on,

were given as illustrative examples. The simulation results were generally in excellent agreement with experimental measurements.

This overall theoretical approach illustrates the importance of material and process interac-

tions. In principle, modeling of sheet forming and microstructure evolution should be a concurrent process. However, in view of the size of the forming simulations and the complexity of the physical phenomena occurring during plastic deformation, it seems more efficient to use macroscopic constitutive models with one or more internal variables to account for the microstructure. Constitutive models at a finer scale are, of course, very important for the understanding of the microstructure evolution, for material design, and for providing a basis for the development of more advanced macroscopic models.

ACKNOWLEDGMENT

The authors are indebted to many of their colleagues, in particular from Alcoa Technical Center, Pittsburgh, Pennsylvania, whose contributions made this work possible. The authors also gratefully acknowledge Dr. Lee Semiatin from the US Air Force Research Laboratory, Wright-Patterson Air Force Base, Ohio, for his excellent review of the manuscript and his pertinent suggestions. Finally, the authors are obliged to ASM International personnel, in particular Mr. Steve Lampan, for the difficult task of preparing this article for publication.

REFERENCES

1. G. Taguchi, *Taguchi on Robust Technology Development*, ASME Press, 1993
2. O. Richmond and W.A. Spitzig, Pressure Dependence and Dilatancy of Plastic Flow, *IUTAM Conference, Theoretical and Applied Mechanics, Proc. 15th International Congress of Theoretical and Applied Mechanics*, North-Holland Publishers, Amsterdam, 1980, p 377–386
3. W.A. Spitzig and O. Richmond, The Effect of Pressure on the Flow Stress of Metals, *Acta Metall.*, Vol 32, 1984, p 457–463
4. U.F. Kocks, C.N. Tomé, and H.-R. Wenk, *Texture and Anisotropy*, University Press, Cambridge, 1998
5. F. Perocheau and J.H. Driver, Slip System Rheology of Al-1% Mn Crystals Deformed by Hot Plane Strain Compression, *Int. J. Plast.*, Vol 18, 2002, p 185–202
6. C.C. Bampton, J. Wadsworth, and A.K. Ghosh, Superplastic Aluminum Alloys, *Aluminum Alloys—Contemporary Research and Applications*, A.K. Vasudévan and R.D. Doherty, Ed., Academic Press, 1989
7. J.E. Hatch, Ed., *Aluminum Properties and Physical Metallurgy*, American Society for Metals, 1984
8. D.G. Altenpohl, *Aluminum: Technology, Applications, and Environment*, TMS, 1998
9. P. Perzyna, Ed., *Localization and Fracture Phenomena in Inelastic Solids*, Springer-Verlag, Wien, 1998

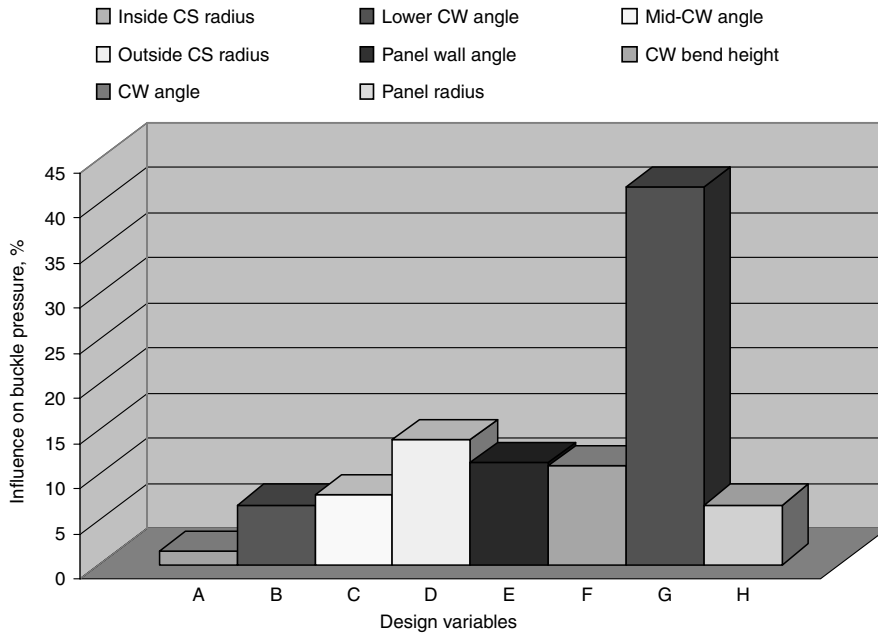


Fig. 62 Influence of design variables on buckle pressure

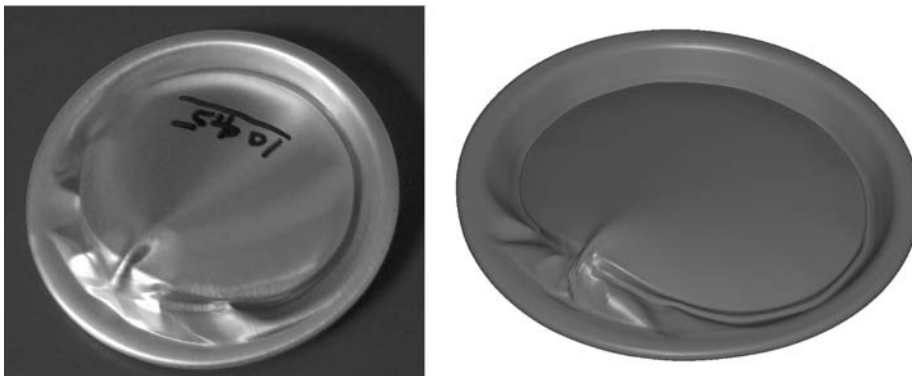


Fig. 63 Comparison of observed and predicted deformed shapes for the new beverage-can end design

10. P.F. Thomason, *Ductile Fracture in Metals*, Pergamon Press, 1990
11. A.S. Krausz and K. Krausz, Ed., *Unified Constitutive Laws of Plastic Deformation*, Academic Press, 1996
12. Y. Estrin, Dislocation Density-Related Constitutive Modeling, *Unified Constitutive Law of Plastic Deformation*, A.S. Krausz and K. Krausz, Ed., Academic Press, 2002, p 69–106
13. W. Gambin, *Plasticity and Texture*, Kluwer Academic Publishers, Amsterdam, 2001
14. P. Dawson, Crystal Plasticity, *Continuum Scale Simulation of Engineering Materials—Fundamentals—Microstructures—Process Applications*, D. Raabe, F. Roters, F. Barlat, and L.-Q. Chen, Ed., Wiley-VCH Verlag GmbH, Berlin, 2004, p 115–143
15. M. Życzkowski, *Combined Loadings in the Theory of Plasticity*, Polish Scientific Publisher, Warsaw, 1981

16. J.F.W. Bishop and R. Hill, A Theory of the Plastic Distortion of a Polycrystalline Aggregate under Combined Stresses, *Philos. Mag.*, Vol 42, 1951, p 414–427
17. F. Barlat, O. Cazacu, M. Zyczkowski, D. Banabic and J.W. Yoon, Yield Surface Plasticity and Anisotropy, *Continuum Scale Simulation of Engineering Materials—Fundamentals—Microstructures—Process Applications*, D. Raabe, F. Roters, F. Barlat, and L.-Q. Chen, Ed., Wiley-VCH, Verlag GmbH, Berlin, 2004, p 145–183
18. H. Sang and D.J. Lloyd, The Influence of Biaxial Prestrain on the Tensile Properties of Three Aluminum Alloys, *Metall. Trans. A*, Vol 10, 1979, p 1773–1776
19. V.N. Rao and V.V. Laukonis, Microstructural Mechanisms for the Anomalous Behavior of Aluminum Killed Steel Prestrain in Plane Strain Tension, *Mater. Sci. Eng.*, Vol 60, 1983, p 125–135

20. C. Teodosiu, and Z. Hu, Microstructure in the Continuum Modeling of Plastic Anisotropy, *Proceedings of the Risø International Symposium on Material Science: Modelling of Structure and Mechanics of Materials from Microscale to Products*, J.V. Cartensen, T. Leffers, T. Lorentzen, O.B. Pedersen, B.F. Sørensen, and G. Winther, Ed., Risø National Laboratory, Roskilde, Denmark, 1998, p 149–168
21. J.J. Gracio, A.B. Lopes, and E.F. Rauch, Analysis of Plastic Instability in Commercially Pure Aluminium, *J. Mater. Proc. Technol.*, Vol 103, 2000, p 160–164
22. F. Mollica, K.R. Rajagopal, and A.R. Srinivasa, The Inelastic Behavior of Metals Subjected to Loading Reversal, *Int. J. Plast.*, Vol 17, 2001, p 1119–1146
23. F. Barlat, J. Ferreira Duarte, J.J. Gracio, A.B. Lopes, and E.F. Rauch, Plastic Flow for Non-Monotonic Loading Conditions of an Aluminum Alloy Sheet Sample, *Int. J. Plast.*, Vol 19, 2003, p 1215–1244
24. B. Peeters, B. Bacroix, C. Teodosiu, P. Van Houtte, and E. Aernould, Work Hardening/Softening Behaviour of b.c.c. Polycrystals during Changing Strain Path, Part II: TEM Observations of Dislocation Sheets in an IF Steel during Two-Stage Strain Paths and Their Representations in Terms of Dislocation Densities, *Acta Mater.*, Vol 49, 2001, p 1621–1632
25. B. Peeters, M. Seefeldt, C. Teodosiu, S.R. Kalindindi, P. Van Houtte, and E. Aernould, Work Hardening/Softening Behaviour of b.c.c. Polycrystals during Changing Strain Path, Part II: An Integrated Model Based on Substructure and Texture Evolution, and Its Predictions of the Stress-Strain Behaviour of an IF Steel during Two-Stage Strain Paths, *Acta Mater.*, Vol 49, 2001, p 1607–1619
26. P.D. Wu, S.R. MacEwen, D.J. Lloyd, M. Jain, P. Tugcu, and K.W. Neale, On Pre-Straining and the Evolution of Material Anisotropy in Sheet Metal, *Int. J. Plast.*, Vol 21, 2005, p 723–739
27. H.W. Swift, Plastic Instability under Plane Stress, *J. Mech. Phys. Solids.*, Vol 1, 1952, p 1–18
28. J.H. Hollomon, Tensile Deformation, *Trans. ASME*, 1945, p 1–22
29. E. Voce, A Practical Strain-Hardening Function, *Metallurgica*, Vol 51, 1955, p 219–226
30. R.C. Picu, G. Vincze, F. Ozturk, J.J. Gracio, F. Barlat, and A. Maniatty, Strain Rate Sensitivity of the Commercial Aluminum Alloy AA5182-O, *Mater. Sci. Eng.*, Vol 390, 2005, p 334–343
31. A.V. Hershey, The Plasticity of an Isotropic Aggregate of Anisotropic Face Centered Cubic Crystals, *J. Appl. Mech.*, Vol 21, 1954, p 241–249
32. W.F. Hosford, A Generalized Isotropic Yield Criterion, *J. Appl. Mech. (Trans. ASME)*, Vol 39, 1972, p 607–609

33. W.F. Hosford, On Yield Loci of Anisotropic Cubic Metals, *Proc. Seventh North American Metalworking Conf.*, SME, 1979, p 191–197
34. R.W. Logan and W.F. Hosford, Upper-Bound Anisotropic Yield Locus Calculations Assuming Pencil Glide, *Int. J. Mech. Sci.*, Vol 22, 1980, p 419–430
35. R. Hill, A Theory of the Yielding and Plastic Flow of Anisotropic Metals, *Proc. R. Soc. (London) A*, Vol 193, 1948, p 281–297
36. F. Barlat and J. Lian, Plastic Behavior and Stretchability of Sheet Metals, Part I: Yield Function for Orthotropic Sheets under Plane Stress Conditions, *Int. J. Plast.*, Vol 5, 1989, p 51–66
37. F. Barlat, D.J. Lege, and J.C. Brem, A Six-Component Yield Function for Anisotropic Metals, *Int. J. Plast.*, Vol 7, 1991, p 693–712
38. A.P. Karafillis and M.C. Boyce, A General Anisotropic Yield Criterion Using Bounds and a Transformation Weighting Tensor, *J. Mech. Phys. Solids*, Vol 41, 1993, p 1859–1886
39. O. Cazacu and F. Barlat, Generalization of Drucker's Yield Criterion to Orthotropy, *Mat. Mech. of Solids*, Vol 6, 2001, p 613–630
40. O. Cazacu, B. Plunkett, and F. Barlat, Orthotropic Yield Criterion for Hexagonal Close Packed Metals, *Int. J. Plast.*, Vol 22, 2006, p 1171–1194
41. F. Barlat, J.C. Brem, J.W. Yoon, K. Chung, R.E. Dick, D.J. Lege, F. Pourboghrat, S.H. Choi, and E. Chu, Plane Stress Yield Function for Aluminum Alloy Sheets, *Int. J. Plast.*, Vol 19, 2003, p 1297–1319
42. F. Barlat, H. Aretz, J.W. Yoon, M.E. Karabin, J.C. Brem, and R.E. Dick, Linear Transformation-Based Anisotropic Yield Functions, *Int. J. Plast.*, Vol 21, 2005, p 1009–1039
43. F. Bron and J. Besson, A Yield Function for Anisotropic Materials—Application to Aluminum Alloys, *Int. J. Plast.*, Vol 21, 2004, p 937–963
44. J.W. Yoon, F. Barlat, R.E. Dick, K. Chung, and T.J. Kang, Plane Stress Yield Function for Aluminum Alloy Sheet, Part II: FE Formulation and Its Implementation, *Int. J. Plast.*, Vol 20, 2004, p 495–522
45. H. Ziegler, *An Introduction to Thermodynamics*, North Holland Publishing Company, Amsterdam, 1977
46. R. Hill, Constitutive Dual Potentials in Classical Plasticity, *J. Mech. Phys. Solids*, Vol 35, 1987, p 22–33
47. R. Fortunier, Dual Potentials and Extremum Work Principles in Single Crystal Plasticity, *J. Mech. Phys. Solids*, Vol 37, 1989, p 779–790
48. M. Arminjon and B. Bacroix, On Plastic Potentials for Anisotropic Metals and Their Derivation from the Texture Function, *Acta Mech.*, Vol 88, 1991, p 219–243
49. P. Van Houtte, Application of Plastic Potentials to Strain-Rate Sensitive and Insensitive Materials, *Int. J. Plast.*, Vol 10, 1994, p 719–748
50. A. Van Bael and P. Van Houtte, Convex Fourth and Sixth-Order Plastic Potentials Derived from Crystallographic Texture, *Non Linear Mechanics of Anisotropic Materials, Proceedings of the Sixth European Mechanics of Materials Conference (EMMC6)*, S. Cescotto, Ed., Sept 2002 (Liege, Belgium), University of Liege, 2002, p 51–58
51. F. Barlat and K. Chung, Anisotropic Potentials for Plastically Deforming Metals, *Model. Simul. Mater. Sci. Eng.*, Vol 1, 1993, p 403–416
52. F. Barlat, K. Chung, J.W. Yoon, and F. Pourboghrat, Plastic Anisotropy Modeling for Sheet Forming Design Applications, *Constitutive and Damage Modeling of Inelastic Deformation and Phase Transformation*, A.S. Khan, Ed., 1998, Neat Press, Fulton (MD), p 301–304
53. F. Barlat and K. Chung, Anisotropic Strain Rate Potential for Aluminum Alloy Plasticity, *Proc. Eight ESAFORM Conference on Material Forming*, D. Banabic, Ed., April 2005 (Cluj-Napoca, Romania), The Publishing House of the Romanian Academy, Bucharest, 2005, p 415–418
54. B. Paul, Macroscopic Criteria for Plastic Flow and Brittle Fracture, *Fracture*, Vol 1, H. Liebowitz, Ed., Academic Press, 1968, p 313–495
55. S.S. Hecker, Experimental Studies of Yield Phenomena in Biaxially Loaded Metals, *Constitutive Modeling in Viscoplasticity*, A. Stricklin and K.C. Sazalski, Ed., ASME, 1976, p 1–33
56. D. Banabic, O. Cazacu, F. Barlat, D.S. Comsa, S. Wagner, and K. Siegert, Description of Anisotropic Behaviour of AA3103-O Aluminum Alloy Using Two Recent Yield Criteria, *Non Linear Mechanics of Anisotropic Materials, Proceedings of the Sixth European Mechanics of Materials Conference (EMMC6)*, S. Cescotto, Ed., Sept 2002 (Liege, Belgium), University of Liege, 2002, p 265–272
57. S.H. Choi, J.C. Brem, F. Barlat, and K.H. Oh, Macroscopic Anisotropy in AA5019A Sheets, *Acta Mater.*, Vol 48, 2000, p 1853–1863
58. R.F. Young, J.E. Bird, and J.L. Duncan, An Automated Hydraulic Bulge Tester, *J. Appl. Metalwork.*, Vol 2, 1981, p 11–18
59. K. Pöhlant, D. Banabic, and K. Lange, Equi-Biaxial Anisotropy Coefficient Used to Describe the Plastic Behavior of Sheet Metals, *Proceedings of the Fifth ESAFORM Conference on Metal Forming*, M. Pietrzyk, Ed., April 2002 (Krakow, Poland), 2002, p 723–727
60. R.H. Wagoner and N.-M. Wang, An Experimental and Analytical Investigation of In-Plane Deformation of 2036-T4 Aluminum Sheet, *Int. J. Mech. Sci.*, Vol 21, 1979, p 255–264
61. F. Taha, A. Graf, and W.F. Hosford, Plane-Strain Tension Tests on Aluminum Alloy Sheet, *J. Eng. Mater. Technol. (Trans. ASME)*, Vol 117, 1995, p 168–171
62. E.F. Rauch and J.-H. Schmitt, Dislocation Substructures in Mild Steel Deformed in Simple Shear, *Mater. Sci. Eng. A*, Vol 113, 1989, p 441–448
63. T. Kuwabara, Y. Morita, Y. Miyashita, and S. Takahashi, Elastic-Plastic Behavior of Sheet Metals Subjected to In-Plane Reverse Loading, *Dynamic Plasticity and Structural Behaviors*, S. Tanimura and A.S. Khan, Ed., Gordon and Breach Publishers, Luxembourg, 1995, p 841–844
64. R.K. Boger, R.H. Wagoner, F. Barlat, M.G. Lee, and K. Chung, Continuous, Large Strain, Tension/Compression Testing of Sheet Material, *Int. J. Plast.*, Vol 21, 2005 p 2319–2343
65. R. Hill, On Discontinuous Plastic States with Special Reference to Localized Necking in Thin Sheets, *J. Mech. Phys. Solids*, Vol 1, 1952, p 19–30
66. Z. Marciniak and K. Kuczynski, Limit Strain in the Process of Stretch Forming Sheet Metal, *Int. J. Mech. Sci.*, Vol 9, 1967, p 609–620
67. J.W. Hutchinson and K.W. Neale, Sheet Necking II: Time Independent Behavior, *Mechanics of Sheet Metal Forming*, D.P. Koistinen and N.M. Wang, Ed., Plenum Press, 1978, p 127–150
68. A. Barata da Rocha and J.M. Jalinier, Plastic Instability of Sheet Metals under Simple and Complex Strain Path, *Trans. Iron Steel Inst. Jpn.*, Vol 24, 1984, p 133–140
69. S. Stören and J.R. Rice, Localized Necking in Thin Sheet, *J. Mech. Phys. Solids.*, Vol 23, 1975, p 421–441
70. R. Sowerby and J.L. Duncan, Failure in Sheet Metal in Biaxial Tension, *Int. J. Mech. Sci.*, Vol 13, 1971, p 217–229
71. J. Lian, F. Barlat, and B. Baudalet, Plastic Behavior and Stretchability of Sheet Metals, Part II: Effect of Yield Surface Shape on Sheet Forming Limit, *Int. J. Plast.*, Vol 5, 1989, p 131–148
72. F. Barlat, Crystallographic Texture, Anisotropic Yield Surfaces and Forming Limits of Sheet Metals, *Mater. Sci. Eng.*, Vol 91, 1987, p 55–72
73. V. Tvergaard, Effect of Kinematic Hardening on Localized Necking in Biaxially Stretched Sheets, *Int. J. Mech. Sci.*, Vol 20, 1978, p 651–658
74. A. Needleman and N. Triantafyllidis, Void Growth and Local Necking in Biaxially Stretched Sheets, *J. Eng. Mech. Technol.*, Vol 100, 1978, p 164–169
75. F. Barlat, A. Barata da Rocha, and J.M. Jalinier, Influence of Damage on the Plastic Instability of Sheet Metal under Complex

- Strain Path, *J. Mater. Sci.*, Vol 19, 1984, p 4133–4137
76. F. Barlat and J.M. Jalinier, Formability of Sheet Metals with Heterogeneous Damage, *J. Mater. Sci.*, Vol 20, 1985, p 3385–3399
 77. F. Barlat and O. Richmond, Modeling Macroscopic Imperfections for the Prediction of Flow Localization and Fracture, *Fatigue Fract. Eng. Mater. Struct.*, Vol 26, 2003, p 311–321
 78. D.J. Lege, F. Barlat, and J.C. Brem, Characterization and Modeling of the Mechanical Behavior and Formability of 2008 Autobody Sheet, *Int. J. Mech. Sci.*, Vol 31, 1989, p 549–563
 79. R.J. Asaro and A. Needleman, Texture Development and Strain Hardening in Rate Dependent Polycrystals, *Acta Metall.*, Vol 33, 1985, p 923–953
 80. F. Barlat, Forming Limit Diagram – Prediction Based on Some Microstructural Aspects of Materials, *Forming Limit Diagram—Concepts, Methods and Applications*, R.H. Wagoner, K.S. Chan and S.P. Keeler, Ed., TMS, 1989, p 275–301
 81. Y. Zhou and K.W. Neale, Predictions of Forming Limit Diagrams Using a Rate-Sensitive Crystal Plasticity Model, *Int. J. Mech. Sci.*, Vol 37, 1995, p 1–20
 82. L.S. Toth, J. Hirsch, and P. Van Houtte, On the Role of Texture Development in the Forming Limits of Sheet Metals, *Int. J. Mech. Sci.*, Vol 38, 1996, p 1117–1126
 83. P.D. Wu, K.W. Neale, and E. Van der Giessen, Simulation of the Behaviour of fcc Polycrystals during Reversed Torsion, *Int. J. Plast.*, Vol 12, 1996, p 1199–1219
 84. P.D. Wu, K.W. Neale, and E. Van der Giessen, On Crystal Plasticity FLD Analysis, *Proc. R. Soc. (London)*, Vol 453, 1997, p 1831–1848
 85. P.D. Wu, S.R. MacEwen, D.J. Lloyd, and K.W. Neale, A Mesoscopic Approach for Predicting Sheet Metal Formability, *Model. Simul. Mater. Sci. Eng.*, Vol 12, 2004, p 511–527
 86. S. Hiwatashi, A. Van Bael, P. Van Houtte, and C. Teodosiu, Prediction of Forming Limit Strains under Strain-Path Changes: Applications of an Anisotropic Model Based on Texture and Dislocation Structure, *Int. J. Plast.*, Vol 14, 1998, p 647–669
 87. K. Inal, N.W. Neale, and A. Aboutajeddine, Forming Limit Comparisons for fcc and bcc Sheets, *Int. J. Plast.*, Vol 21, 2005, p 1255–1266
 88. T. Kikuma and K. Nakazima, Effects of Deforming Conditions and Mechanical Properties on the Stretch Forming Limits of Steel Sheets, *Trans. Iron Steel Inst. Jpn.*, Vol 11, 1971, p 827–831
 89. T. Kobayashi, T. Ishigaki, and T. Abe, *Proc. Seventh Congress International Deep Drawing Research Group*, Vol 8.2 (Amsterdam), 1972
 90. A. Graf and W.F. Hosford, Calculations of Forming Limit Diagrams for Changing Strain Paths, *Metall. Trans. A*, Vol 24, 1993, p 2497–2501
 91. A. Graf and W.F. Hosford, Effect of Changing Strain Paths on Forming Limit Diagrams of Aluminum 2008-T4, *Metall. Trans. A*, Vol 24, 1993, p 2503–2512
 92. H.J. Kleemola and M.T. Pelkkikangas, Effect of Predeformation and Strain Path on the Forming Limits of Steel, Copper, and Brass, *Sheet Met. Ind.*, Vol 63, 1977, p 591–599
 93. R. Arrieux, C. Bedrin, and M. Boivin, Determination of an Intrinsic Forming Limit Stress Diagram for Isotropic Sheet Metals, *Proc. Congress International Deep Drawing Research Group*, May 1982 (S. Margherita Ligure, Italy), Working Group Volume, p 61–72
 94. T.B. Stoughton, General Forming Limit Criterion for Sheet Metal Forming, *Int. J. Mech. Sci.*, Vol 42, 2000, p 1–27
 95. T.B. Stoughton and J.W. Yoon, Sheet Metal Formability Analysis for Anisotropic Materials under Non-Proportional Loading, *Int. J. Mech. Sci.*, Vol 47, 2005, p 1972–2002
 96. T. Kuwabara, K. Yoshida, K. Narihara, and S. Takahashi, Forming Limits of Aluminum Alloy Tubes under Axial Load and Internal Pressure, *Proceedings of Plasticity '03*, NEAT Press, 2003, p 388–390
 97. T.X. Yu and W. Johnson, The Buckling of Annular Plates in Relation to the Deep Drawing Process, *Int. J. Mech. Sci.*, Vol 24, 1982, p 175–188
 98. T.X. Yu, W. Johnson, and W.J. Stronge, Stamping Rectangular Plates into Doubly-Curved Dies, *Proc. Inst. Mech. Eng.*, Vol 198, 1984, p 109–125
 99. W.J. Stronge, M.P.F. Sutcliffe, and T.X. Yu, Wrinkling of Elastoplastic Circular Plates during Stamping, *Exp. Mech.*, Vol 26, 1986, p 345–353
 100. E. Riks, An Incremental Approach to the Solution of Snapping and Buckling Problems, *Int. J. Solids Struct.*, Vol 15, 1979, p 529–551
 101. X. Wang and L.H.N. Lee, Postbifurcation Behavior of Wrinkles in Square Metal Sheet under Yoshida Test, *Int. J. Plast.*, Vol 9, 1993, p 1–19
 102. J.B. Kim, J.W. Yoon, and D.Y. Yang, Wrinkling Initiation and Growth in Modified Yoshida Buckling Test, *Int. J. Mech. Sci.*, Vol 42, 2000, p 1693–1714
 103. J.B. Kim, J.W. Yoon, and D.Y. Yang, Investigation into the Wrinkling Behavior of Thin Sheet on the Cylindrical Cup Deep Drawing Process Using Bifurcation Theory, *Int. J. Num. Methods Eng.*, Vol 56, 2003, p 1673–1705
 104. G. Powell and J. Simons, Improved Iteration Strategy for Nonlinear Structures, *Int. J. Numer. Method. Eng.*, Vol 17, 1981, p 1455–1467
 105. Y. Tomita and A. Shindo, Onset and Growth of Wrinkling in Thin Square Plate Subjected to Diagonal Tension, *Int. J. Mech. Sci.*, Vol 30, 1988, p 921–931
 106. S.L. Chan, A Non-Linear Numerical Method for Accurate Determination of Limit and Bifurcation Points, *Int. J. Num. Method Eng.*, Vol 36, 1993, p 2779–2790
 107. A.S. Gendy and A.F. Saleeb, Generalized Mixed Finite Element Model for Pre- and Post-Quasistatic Buckling Response of Thin-Walled Frame Structures, *Int. J. Num. Method. Eng.*, Vol 37, 1994, p 297–322
 108. J. Cao and M.C. Boyce, Optimization of Sheet Metal Forming Processes by Instability Analysis, *Proceedings of NUMIFORM '95*, A.A. Balkema, Rotterdam, 1995, p 675–679
 109. F.R. Shanley, Inelastic Column Theory, *J. Aeronaut. Sci.*, Vol 14, 1947, p 261–268
 110. R. Hill, A General Theory of Uniqueness and Stability in Elastic-Plastic Solids, *J. Mech. Phys. Solids*, Vol 6, 1958, p 236–249
 111. J.W. Hutchinson, Post-Bifurcation Behavior in the Plastic Range, *J. Mech. Phys. Solids*, Vol 21, 1973, p 163–190
 112. E. Riks, The Application of Newton's Method to the Problem of Elastic Stability, *J. Appl. Mech.*, Vol 39, 1972, p 1060–1066
 113. H.S. Lee, D.W. Jung, J.H. Jeong, and S. Im, Finite Element Analysis of Lateral Buckling for Beam Structures, *Comput. Struct.*, Vol 53, 1994, p 1357–1371
 114. F. Pourboghrat and E. Chu, Springback in Plane Strain Stretch/Draw Sheet Forming, *Int. J. Mech. Sci.*, Vol 36, 1995, p 327–341
 115. F. Pourboghrat, K. Chung, and O. Richmond, A Hybrid Membrane/Shell Method for Rapid Estimation of Springback in Anisotropic Sheet Metals, *J. Appl. Mech. (Trans. ASME)*, Vol 65, 1998, p 671–684
 116. J.W. Yoon, F. Pourboghrat, K. Chung, and D.Y. Yang, Springback Prediction for Sheet Metal Forming Process Using a 3-D Hybrid Membrane/Shell Method, *Int. J. Mech. Sci.*, Vol 44, 2002, p 2133–2153
 117. K.P. Li, W.P. Carden, and R.H. Wagoner, Simulation of Springback, *Int. J. Mech. Sci.*, Vol 44, 2002, p 103–122
 118. M.C. Oliveira, J.L. Alves, B.M. Chaparro, and L.F. Menezes, Study on the Influence of the Work Hardening Models Constitutive Parameters Identification in the Springback Prediction, *Proceeding of the Sixth International Conference and Workshop on Numerical Simulation of 3-D Sheet Metal Forming Processes*, L.M. Smith, F. Pourboghrat, J.W. Yoon, and T.B. Stoughton, Ed. (Detroit, MI), 2005, p 253–258
 119. D. Zeng and Z.C. Xia, An Anisotropic Hardening Model for Springback Prediction, *Proceedings of the Sixth International Conference and Workshop on Numerical Simulation of 3-D Sheet Metal Forming Processes*, L.M. Smith, F. Pourboghrat,

- J.W. Yoon, and T.B. Stoughton, Ed. (Detroit, MI), 2005, p 226–241
120. S.W. Lee and D.Y. Yang, An Assessment of Numerical Parameters Influencing Springback in Explicit Finite Element Analysis of Sheet Forming Processes, *J. Mater. Process. Technol.*, Vol 80–81, 1998, p 60–67
 121. K. Li and R.H. Wagoner, Simulation of Springback, *Simulation of Materials Processing*, J. Huetink and F.P.T. Baaijens, Ed., A.A. Balkema, Rotterdam, 1998, p 21–32
 122. R.H. Wagoner, Sheet Springback, *Continuum Scale Simulation of Engineering Materials—Fundamentals—Microstructures—Process Applications*, D. Raabe, F. Roters, F. Barlat, L.-Q. Chen, Ed., Wiley-VCH Verlag GmbH, Berlin, 2004, p 777–794
 123. L. Geng and R.H. Wagoner, Role of Plastic Anisotropy and Its Evolution on Springback, *Int. J. Mech. Sci.*, Vol 44, 2002, p 123–148
 124. R.H. Wagoner, W.D. Carden, W.P. Carden, and D.K. Matlock, Springback after Drawing and Bending of Metal Sheets, *Proc. IPMM '97—Intelligent Processing and Manufacturing of Materials*, T. Chandra, S.R. Leclair, J.A. Meech, B. Verma, and M. Smith, Ed., Balachandram, University of Wollongong (Intelligent Systems Applications), 1997, p 1–10
 125. J.F. Wang, R.H. Wagoner, W.P. Carden, D.K. Matlock, and F. Barlat, Creep and Anelasticity in the Springback of Aluminum Alloys, *Int. J. Plast.*, Vol 20, 2004, p 2209–2232
 126. W. Prager, A New Method of Analyzing Stresses and Strains in Work-Hardening Plastic Solids, *J. Appl. Mech. (Trans. ASME)*, Vol 23, 1956, p 493–496
 127. H. Ziegler, A Modification of Prager's Hardening Rule, *Q. Appl. Math.*, Vol 17, 1959, p 55–65
 128. J.L. Chaboche, Time Independent Constitutive Theories for Cyclic Plasticity, *Int. J. Plast.*, Vol 2, 1986, p 149–188
 129. Z. Mróz, Non-Associated Flow Laws in Plasticity, *J. Mécan.*, Vol 2, 1963, p 21–42
 130. R.D. Krieg, A Practical Two Surface Plasticity Theory, *J. Appl. Mech.*, Vol 42 1975, p 641–646
 131. Y.F. Dafalias and E.P. Popov, Plastic Internal Variables Formalism of Cyclic Plasticity, *J. Appl. Mech.*, Vol 98, 1976, p 645–651
 132. K. Chung, M.G. Lee, D. Kim, C. Kim, M.L. Wenner, and F. Barlat, Spring-Back Evaluation of Automotive Sheets Based on Isotropic-Kinematic Hardening Laws and Non-Quadratic Anisotropic Yield Functions, Part I: Theory and Formulation, *Int. J. Plast.*, Vol 21, 2005, p 861–882
 133. M.G. Lee, D. Kim, C. Kim, M.L. Wenner, R.H. Wagoner, and K. Chung, Spring-Back Evaluation of Automotive Sheets Based on Isotropic-Kinematic Hardening Laws and Non-Quadratic Anisotropic Yield Function, Part II: Characterization of Material Properties, *Int. J. Plasticity*, Vol 21, 2005, p 883–914
 134. M.G. Lee, D. Kim, C. Kim, M.L. Wenner, and K. Chung, Spring-Back Evaluation of Automotive Sheets Based on Isotropic-Kinematic Hardening Laws and Non-Quadratic Anisotropic Yield Functions, Part III: Applications, *Int. J. Plast.*, Vol 21, 2005, p 915–953
 135. N.M. Wang and B. Budianski, Analysis of Sheet Metal Stamping by a Finite Element Method, *J. Appl. Mech. (Trans. ASME)*, Vol 45, 1978, p 73–82
 136. D.Y. Yang and Y.J. Kim, A Rigid-Plastic Finite Element Calculation for the Analysis of General Deformation of Plastic Anisotropic Sheet Metals and Its Application, *Int. J. Mech. Sci.*, Vol 28, 1986, p 825
 137. P. Hora, T.C. Vu, P.M. Wollrab, and J. Reissner, Simulation of the Forming Process for Irregularly Shaped Autobody Panels, *Advanced Technology of Plasticity (Proc. Second ICTP)*, K. Lange, Ed., Springer, Stuttgart, Germany, 1987, p 663
 138. D.J. Yoo, I.S. Song, D.Y. Yang, and J.H. Lee, Rigid-Plastic Finite Element Analysis of Sheet Metal Forming Processes Using Continuous Contact Treatment and Membrane Elements Incorporating Bending Effect, *Int. J. Mech. Sci.*, Vol 36, 1994, p 513–546
 139. W. Kubli and J. Reissner, Optimization of Sheet Metal Forming Processes Using the Special-Purpose Program AUTOFORM, *Proc. Second International Conference NUMISHEET '93*, A. Machinouch et al., Ed (Isehara, Japan), 1993, p 271–280
 140. S. Ahmad, B.M. Irons, and O.C. Zienkiewicz, Analysis of Thick and Thin Shell Structure by Curved Finite Elements, *Int. J. Numer. Methods Eng.*, Vol 2, 1970, p 419–451
 141. E. Ramm, A Plate/Shell Element for Large Deflection and Rotations, *Formulation and Computational Algorithms in Finite Element Analysis*, K.J. Bathe, J.T. Oden, and W. Wunderlich, Ed., MIT Press, 1977
 142. H. Parish, Nonlinear Analysis of Shells Using Isoparametric Elements, in *ASME Conference*, T.J.R. Hughes et al., Ed., New York, 1981, p 48
 143. T.J.R. Hughes and W.K. Liu, Nonlinear Finite Element Analysis of Shells. Part I: Three-Dimensional Shells, *Comput. Methods Appl. Mech. Eng.*, Vol 26, 1981, p 331–362
 144. T.J.R. Hughes and W.K. Liu, Nonlinear Finite Element Analysis of Shells, Part II: Two-Dimensional Shells, *Comput. Method. Appl. Mech. Eng.*, Vol 27, 1981, p 167–181
 145. E.N. Dvorkin and K.J. Bathe, A Continuum Mechanics Based on Four-Node Shell Element for General Non-Linear Analysis, *Eng. Comp. (Int. J. Comput.-Aided Eng. Software)*, Vol 1, 1984, p 77–88
 146. W.K. Liu, E.S. Law, D. Lam, and T. Belytschko, Resultant-Stress Degenerated Shell Element, *Comput. Methods Appl. Mech. Eng.*, Vol 55, 1986, p 259–300
 147. K.J. Bathe, *Finite Element Procedures in Engineering Analysis*, Prentice-Hall, 1982
 148. T.J.R. Hughes, *The Finite Element Method*, Prentice-Hall, 1987
 149. G. Stanley, "Continuum-Based Shell Elements," Ph.D. dissertation, Applied Mechanics Division, Stanford University, 1985
 150. T. Belytschko, J.I. Lin, and C. Tsay, Explicit Algorithms for the Nonlinear Dynamics of Shells, *Comput. Methods Appl. Mech. Eng.*, Vol 42, 1989, p 225–251
 151. J.O. Hallquist, D.J. Benson, and G.L. Goudreau, Implementation of a Modified Hughes-Liu Shell into a Fully Vectorized Explicit Finite Element Code, *Finite Element Methods for Nonlinear Problems*, P. Bergan et al., Ed., Springer, Berlin, 1986, p 283
 152. T. Belytschko and I. Leviatan, Physical Stabilization of the 4-Node Shell Element with One Point Quadrature, *Comput. Methods Appl. Mech. Eng.*, Vol 113, 1994, p 321–350
 153. R.P.R. Cardoso and J.W. Yoon, One Point Quadrature Shell Elements for Sheet Metal Forming Analysis, *Arch. Comput. Method Eng.*, Vol 12, 2005, p 3–66
 154. R.P.R. Cardoso and J.W. Yoon, A One Point Quadrature Shell Element for Through Thickness Deformation, *Comp. Methods Appl. Mech. Eng.*, Vol 194, 2005, p 1161–1199
 155. J.L. Batoz, J.M. Roeland, P. Pol, and P. Duroux, A Membrane Bending Finite Element Model for Sheet Forming, *Proc. NUMIFORM '89 Conference*, A.A. Balkema, Rotterdam, 1989, p 389
 156. R.J. Alves de Sousa, R.P.R. Cardoso, R.A.F. Valente, J.W. Yoon, J.J. Gracio, and R.M.N. Jorge, A New One-Point Quadrature Enhanced Assumed Strain Solid-Shell Element with Multiple Integration Points along Thickness, Part I: Geometrically Linear Applications, *Int. J. Numer. Methods Eng.*, Vol 62, 2005, p 952–977
 157. M.E. Honnor and R.D. Wood, Finite Element Analysis of Axisymmetric Deep Drawing Using a Simple Two-Noded Mindlin Shell Element, *Numerical Methods for Nonlinear Problems*, C. Taylor et al., Ed., Pineridge Press, 1987, p 440
 158. A. Honecker and K. Mattiason, Finite Element Procedures for 3-D Sheet Forming Simulation, *Proc. of the NUMIFORM '89 Conference*, A.A. Balkema, Rotterdam, 1989, p 457–463
 159. E. Massoni and J.L. Chenot, 3-D Finite Element Simulation of Deep-Drawing Process, *Proc. NUMIFORM '92 Conference*,

- A.A. Balkema, Rotterdam, 1992, p 503–507
160. M. Kawka and A. Makinouchi, Finite Element Simulation of Sheet Metal Forming Processes by Simultaneous Use of Membrane, Shell and Solid Elements, *Proc. NUMIFORM '92 Conference*, A.A. Balkema, Rotterdam, 1992, p 491–495
 161. J.W. Yoon, D.Y. Yang, and K. Chung, Elasto-Plastic Finite Element Method Based on Incremental Deformation Theory and Continuum Based Shell Elements for Planar Anisotropic Sheet Materials, *Comput. Methods Appl. Mech. Eng.*, Vol 174, 1999, p 23–56
 162. R. Hill, Stability of Rigid-Plastic Solids, *J. Mech. Phys. Solids*, Vol 6, 1957, p 1–8
 163. R. Hill, External Paths of Plastic Work and Deformation, *J. Mech. Phys. Solids*, Vol 34, 1986, p 511–523
 164. A. Nadai, *Theory of Flow and Fracture of Solids*, Vol 2, McGraw-Hill, 1963, p 96
 165. K. Chung and O. Richmond, A Deformation Theory of Plasticity Based on Minimum Work Paths, *Int. J. Plast.*, Vol 9, 1993, p 907–920
 166. Y. Germain, K. Chung, and R.H. Wagoner, A Rigid-Viscoplastic Finite Element Program for Sheet Metal Forming Analysis, *Int. J. Mech. Sci.*, Vol 31, 1989, p 1–24
 167. K. Chung and O. Richmond, Ideal Forming, Part I: Homogeneous Deformation with Minimum Plastic Work, *Int. J. Mech. Sci.*, Vol 34, 1992, p 575–591
 168. K. Chung and O. Richmond, Ideal Forming, Part II: Sheet Forming with Optimum Deformation, *Int. J. Mech. Sci.*, Vol 34, 1992, p 617–633
 169. J.W. Yoon, I.S. Song, D.Y. Yang, K. Chung, and F. Barlat, Finite Element Method for Sheet Forming Based on an Anisotropic Strain-Rate Potential and the Convected Coordinate System, *Int. J. Mech. Sci.*, Vol 37, 1995, p 733–752
 170. H.J. Braudel, M. Abouaf, and J.L. Chenot, An Implicit and Incremental Formulation for the Solution of Elasto-Plastic Problems by the Finite Element Method, *Comput. Struct.*, Vol 22, 1986, p 801–814
 171. J.W. Yoon, D.Y. Yang, K. Chung, and F. Barlat, A General Elasto-Plastic Finite Element Formulation Based on Incremental Deformation Theory for Planar Anisotropy and Its Application to Sheet Metal Forming, *Int. J. Plast.*, Vol 15, 1996, p 35–67
 172. M.L. Wilkins, Calculation of Elasto-Plastic Flow, *Methods of Computational Physics*, B. Alder et al., Ed., Academic Press, 1964, p 3
 173. M. Ortiz and P.M. Pinsky, “Global Analysis Methods for the Solution of Elastoplastic and Viscoplastic Dynamic Problems,” Report UCB/SESM 81/08, Dept. Civil Eng., Univ. of California, Berkeley, 1981
 174. M. Ortiz, P.M. Pinsky, and R.L. Taylor, Operator Split Methods for the Numerical Solution of the Elastoplastic Dynamic Problem, *Comput. Methods Appl. Mech. Eng.*, Vol 39, 1983, p 137–157
 175. M. Ortiz and J.C. Simo, An Analysis of a New Class of Integration Algorithm for Elastoplastic Relations, *Int. J. Numer. Methods Eng.*, Vol 23, 1986, p 353–366
 176. M. Dao and R.J. Asaro, Localized Deformation Modes and Non-Schmid Effects in Crystalline Solids, Part I. Critical Conditions of Localization, *Mech. Mater.*, Vol 23, 1996, p 71–102
 177. J.W. Yoon, F. Barlat, J.J. Gracio, and E. Rauch, Anisotropic Strain Hardening Behavior in Simple Shear for Cube Textured Aluminum Alloy Sheets, *Int. J. Plast.*, Vol 21, 2005, p 2426–2447
 178. K. Chung, J.W. Yoon, and O. Richmond, Ideal Sheet Forming with Frictional Constraints, *Int. J. Plast.*, Vol 16, 2000, p 595–610
 179. F. Barlat, K. Chung, and O. Richmond, Anisotropic Plastic Potentials for Polycrystals and Application to the Design of Optimum Blank Shapes in Sheet Forming, *Metall. Mater. Trans. A*, Vol 25, 1994, p 1209–1216
 180. K. Chung, S.Y. Lee, F. Barlat, Y.T. Keum, and J.M. Park, Finite Element Simulation of Sheet Forming Based on a Planar Anisotropic Strain-Rate Potential, *Int. J. Plast.*, Vol 12, 1996, p 93–115
 181. O. Richmond and K. Chung, Ideal Stretch Forming Processes for Minimum Weight Axisymmetric Shell Structures, *Int. J. Mech. Sci.*, Vol 42, 2000, p 2455–2468
 182. O. Richmond and M.L. Devenpeck, A Die Profile for Maximum Efficiency in Strip Drawing, *Proceedings Fourth U.S. National Cong. Appl. Mech.*, 1962, p 1053–1057
 183. O. Richmond and H.L. Morrison, Streamlined Wire Drawing Dies of Minimum Length, *J. Mech. Phys. Solids*, Vol 15, 1967, p 195–203
 184. R. Hill, Ideal Forming Operations for Perfectly Plastic Solids, *J. Mech. Phys. Solids*, Vol 15, 1967, p 223–227
 185. O. Richmond, Theory of Streamlined Dies for Drawing and Extrusion, *Mechanics of Solid State*, F.P.J. Rimrott and J. Schwaighofer, Ed., Univ. of Toronto Press, 1968, p 154
 186. O. Richmond and S. Alexandrov, Nonsteady Planar Ideal Plastic Flow: General and Special Analytic Solution, *J. Mech. Phys. Solids*, Vol 48, 2000, p 1735–1759
 187. K. Chung, W. Lee, T.J. Kang, and J.R. Yoon, Non-Steady Plane-Strain Ideal Forming without Elastic Dead-Zone, *Fibers Polym.*, Vol 3, 2002, p 120–127
 188. E.F. Rauch, J.J. Gracio, F. Barlat, A.B. Lopes, and J. Ferreira Duarte, Hardening Behaviour and Structural Evolutions upon Strain Reversal of Aluminum Alloys, *Scr. Mater.*, Vol 46, 2002, p 881–886
 189. A.B. Lopes, F. Barlat, J.J. Gracio, J. Ferreira Duarte, and E.F. Rauch, Effect of Texture and Microstructure on Strain Hardening Anisotropy for Aluminum Deformed in Uniaxial Tension and Simple Shear, *Int. J. Plast.*, Vol 19, 2003, p 1–22
 190. K. Chung and K. Shah, Finite Element Simulation of Sheet Metal Forming for Planar Anisotropic Metals, *Int. J. Plast.*, Vol 8, 1992, p 453–476
 191. A. Andersson, C.A. Ohlsson, K. Mattiason, and B. Persson, Implementation and Evaluation of the Karafillis-Boyce Material Model for Anisotropic Metal Sheets, *Proceedings of NUMISHEET '99*, Vol 1, J.C. Gelin and P. Picart, Ed. (Besancon, France), 1999, p 115–121
 192. J.W. Yoon, F. Barlat, K. Chung, F. Pourboghra, and D.Y. Yang, Earing Predictions Based on Asymmetric Nonquadratic Yield Function, *Int. J. Plast.*, Vol 16, 2000, p 1075–1104
 193. F. Barlat, Y. Maeda, K. Chung, M. Yanagawa, J.C. Brem, Y. Hayashida, D.J. Lege, K. Matsui, S.J. Murtha, S. Hattori, R.C. Becker, and S. Makosey, Yield Function Development for Aluminum Alloy Sheet, *J. Mech. Phys. Solids*, Vol 45, 1997, p 1727–1763
 194. J.W. Yoon, F. Barlat, R.E. Dick, and M.E. Karabin, Prediction of Six or Eight Ears in a Drawn Cup Based on a New Anisotropic Yield Function, *Int. J. Plast.*, Vol 22, 2006, p 174–193
 195. F. Barlat, H. Aretz, J.W. Yoon, M.E. Karabin, J.C. Brem, and R.E. Dick, Linear Transformation-Based Anisotropic Yield Functions, *Int. J. Plast.*, Vol 21, 2005, p 1009–1039
 196. J.C. Gelin and P. Picart, *Proceedings of NUMISHEET '99*, Vol 2, J.C. Gelin and P. Picart, Ed., Sept 13–17, 1999 (Besancon, France)
 197. R. Narayanasamy and R. Sowerby, Wrinkling of Sheet Metals When Drawing Through a Conical Die, *J. Mater. Process. Technol.*, Vol 41, 1994, p 275–290
 198. J. Cao, M.F. Shi, T.B. Stoughton, C.T. Wang, and L. Zhang, Ed., NUMISHEET 2005 Benchmark Study, *Proceedings of the Sixth International Conference and Workshop on Numerical Simulation of 3-D Sheet Metal Forming Processes: Part B*, Aug 15–19, 2005 (Detroit, MI), 2005, p 1179–1190
 199. S.H. Zhang, Developments in Hydroforming, *J. Mater. Process. Technol.*, Vol 91, 1999, p 236–244
 200. M. Ahmetoglu and T. Altan, Tube Hydroforming: State-of-the-Art and Future Trends, *J. Mater. Process. Technol.*, Vol 98, 2000, p 25–33
 201. Hydroforming Technology, *Adv. Mater. Process.*, Vol 151, 1997, p 50–53
 202. S. Nakamura, H. Sugiura, H. Onoe, and K. Ikemoto, Hydromechanical Drawing of

- Automotive Parts, *J. Mater. Process. Technol.*, Vol 46, 1994, p 491–503
203. F. Dohmann and C. Hartl, Hydroforming—A Method to Manufacture Light-Weight Parts, *J. Mater. Process. Technol.*, Vol 60, 1996, p 669–676
204. Y. Guan, “A Cross Section Analysis Finite Element Code for Tube Hydroforming,” Master of Science Thesis, Michigan State University, 2000
205. G.T. Kridili, L. Bao, and P.K. Mallick, Two-Dimensional Plane Strain Modeling of Tube Hydroforming, *Proceedings of the ASME, Manufacturing in Engineering Division*, MED-Vol 11, 2000, p 629–634
206. M. Koc and T. Altan, Application of Two-Dimensional (2-D) FEA for the Tube Hydroforming Process, *Int. J. Mach. Tools Manuf.*, Vol 42, 2002, p 1285–1295
207. Y.-M. Hwang and T. Altan, FE Simulations of the Crushing of Circular Tubes into Triangular Cross-Sections, *J. Mater. Process. Technol.*, Vol 125–126, 2002, p 833–838
208. M. Koc, T. Allen, S. Jiratheranat, and T. Altan, The Use of FEA and Design of Experiments to Establish Design Guidelines for Simple Hydroforming Parts, *Int. J. Mech. Sci.*, Vol 40, 2000, p 2249–2266
209. L. Wu and Y. Yu, Computer Simulations of Forming Automotive Structural Parts by Hydroforming Process, *Proceedings of NUMISHEET '96*, J.K. Lee, G.L. Kinzel, and R.H. Wagoner, Ed., 1996, p 324–329
210. N. Dwyer, M. Worswick, J. Gholipour, C. Xia, and G. Khodayari, Pre-Bending and Subsequent Hydroforming of Tube: Simulation and Experiment, *Proceedings of NUMISHEET 2002*, D.-Y. Yang, S.I. Oh, H. Huh, and Y.H. Kim, Ed., 2002, p 447–452
211. K. Trana, Finite Element Simulation of the Tube Hydroforming Process—Bending, Preforming and Hydroforming, *J. Mater. Process. Technol.*, Vol 127, 2002, p 410–408
212. J.-B. Yang, B.-H. Jeon, and S.-I. Oh, The Tube Bending Technology of a Hydroforming Process for an Automotive Part, *J. Mater. Process. Technol.*, Vol 111, 2001, p 175–181
213. H.J. Berg, P. Hora, and J. Reissner, Simulation of Complex Hydroforming Process Using an Explicit Code with a New Shell Formulation, *Proceedings of NUMISHEET '96*, J.K. Lee, G.L. Kinzel, and R.H. Wagoner, Ed., 1996, p 330–335
214. O. Ghouati, M. Baida, H. Lenoir, and J.C. Gelin, 3-D Numerical Simulation of Tube Hydroforming, *Proceedings of Sixth ICTP, Advanced Technology of Plasticity 1999*, M. Geiger, Ed., Springer, Berlin, 1999, p 1211–1216
215. J.-B. Yang, B.-H. Jeon, and S.-I. Oh, Design Sensitivity Analysis and Optimization of the Hydroforming Process, *J. Mater. Process. Technol.*, Vol 113, 2001, p 666–672
216. J. Kim, B.S. Kang, and S.M. Hwang, Preform Design in Hydroforming by the Three-Dimensional Backward Tracing Scheme of the FEM, *J. Mater. Process. Technol.*, Vol 130–131, 2002, p 100–106
217. K. Chung and J.W. Yoon, Direct Design Method Based on Ideal Forming Theory for Hydroforming and Flanging Processes, *Proc. NUMISHEET 2005*, L.M. Lorenzo, F. Pourboghraat, J.W. Yoon, and T.B. Stoughton, Ed., Aug 15–19, 2005 (Detroit, MI), p 40–45
218. M. Phadke, *Quality Engineering Using Robust Design*, Prentice Hall, 1989